SENSOR FAULT DETECTION AND DIAGNOSIS APPROACHES APPLIED TO AN AUTONOMOUS SOLAR-POWERED AIRCRAFT

Paulo Victor Padrão Lopes

Dissertação de Mestrado apresentada ao Programa de Pós-graduação em Engenharia Elétrica, COPPE, da Universidade Federal do Rio de Janeiro, como parte dos requisitos necessários à obtenção do título de Mestre em Engenharia Elétrica.

Orientador: Liu Hsu

Rio de Janeiro
Fevereiro de 2020

SENSOR FAULT DETECTION AND DIAGNOSIS APPROACHES APPLIED TO AN AUTONOMOUS SOLAR-POWERED AIRCRAFT

Paulo Victor Padrão Lopes

DISSERTAÇÃO SUBMETIDA AO CORPO DOCENTE DO INSTITUTO ALBERTO LUIZ COIMBRA DE PÓS-GRADUAÇÃO E PESQUISA DE ENGENHARIA (COPPE) DA UNIVERSIDADE FEDERAL DO RIO DE JANEIRO COMO PARTE DOS REQUISITOS NECESSÁRIOS PARA A OBTENÇÃO DO GRAU DE MESTRE EM CIÊNCIAS EM ENGENHARIA ELÉTRICA.

Orientador: Liu Hsu

Aprovada por: Prof. Liu Hsu
Profª. Lilian Kawakami Carvalho
Prof. Marco Henrique Terra

RIO DE JANEIRO, RJ – BRASIL
FEVEREIRO DE 2020

Lopes, Paulo Victor Padrão

Sensor Fault Detection and Diagnosis Approaches applied to an Autonomous Solar-powered Aircraft/Paulo Victor Padrão Lopes. – Rio de Janeiro: UFRJ/COPPE, 2020.

XXXVIII, 171 p.: il.; 29, 7cm.

Orientador: Liu Hsu

Dissertação (mestrado) – UFRJ/COPPE/Programa de Engenharia Elétrica, 2020.

Referências Bibliográficas: p. 120 – 125.

1. Sensor fault detection. 2. Sensor fault diagnosis. 3. Autonomous Aircraft systems. I. Hsu, Liu. II. Universidade Federal do Rio de Janeiro, COPPE, Programa de Engenharia Elétrica. III. Título.

Agradecimentos

Ao longo de quase três anos vivenciei tudo que a vida acadêmica pode oferecer. Por essa razão, gostaria de agradecer a todos aqueles que me proporcionaram essa experiência.

Agradeço a minha mãe Adriana e minha irmã Maria Paula por estarem sempre ao meu lado em todos os momentos. Juntos permanecemos.

Agradeço a minha querida Thais por todo o incentivo e amor que ofereceu durante esse período. Você foi essencial. Eu te amo.

Aos amigos que estiveram presentes durante as infindáveis viagens entre Santo Antônio de Pádua, Campos dos Goytacazes e Rio de Janeiro. Aos que me receberam e me acompanharam em Gilching. Aos amigos de sempre.

Aos pesquisadores Konstantin Kondak - chefe do grupo Flying Robots - e Michael Vilzmann pela oportunidade de estagiar no Departamento de Robótica e Mecatrônica do Centro Aeroespacial Alemão.

Ao prof. Alexandre Carvalho Leite pelas inúmeras discussões sobre cultura, sociedade, tecnologia, inovação e engenharia.

Ao meu orientador Prof. Liu Hsu pela sua paciência, conselhos e confiança. Tê-lo como referência me ajudou a seguir em frente.

Resumo da Dissertação apresentada à COPPE/UFRJ como parte dos requisitos necessários para a obtenção do grau de Mestre em Ciências (M.Sc.)

ABORDAGENS DE DETECÇÃO E DIAGNÓSTICO DE FALHAS EM SENSORES APLICADAS A UMA AERONAVE AUTÔNOMA MOVIDA A ENERGIA SOLAR

Paulo Victor Padrão Lopes

Fevereiro/2020

Orientador: Liu Hsu

Programa: Engenharia Elétrica

Elektra 2 é uma aeronave autônoma movida a energia solar projetada para suportar longas distâncias e altas altitudes. A principal motivação deste trabalho é desenvolver e comparar diferentes abordagens de detecção e diagnóstico de falhas (DDF) nos sensores IMU da aeronave Elektra 2. Atualmente, a aeronave fornece a verificação de medidas como taxas angulares e ângulos de atitude através da checagem de limiares pré-definidos. Esta abordagem simplista pode esconder comportamentos falhados do sistema, dificultando a pronta detecção de uma falha. Tal estratégia pode ainda ocasionar a completa perda de alarmes de falha ou até mesmo provocar consequências desastrosas para o sistema como um todo. A primeira abordagem de DDF proposta baseia-se em modelos lineares laterais e longitudinais da aeronave combinados com o projeto de filtros de Kalman para geração de resíduos e do uso de limiares adaptativos (técnica ATLMS) para detecção de falhas. A segunda abordagem de DDF proposta é baseada em um modelo cinemático da aeronave combinado com um filtro de Kalman estendido para geração de resíduos. O erro quadrático médio de tais resíduos é então avaliado por uma lógica de limiares para deteccção de falhas. Uma tabela de decisão baseada na sequência de ativação de alarmes de falhas é usada para o diagnóstico de falhas nas duas primeiras abordagens. A terceira abordagem de DDF é uma estratégia *model-free* baseada na análise de componentes principais. Contribuições para o erro de predição quadrático são usadas para diagnóstico de falhas. Por fim, uma quarta abordagem de DDF é apresentada combinando as principais vantagens das abordagens anteriores. A metodologia de simulação cobriu diferentes cenários de voo com diferentes falhas aditivas aplicadas às medidas das taxas de rolagem e arfagem bem como da aceleração longitudinal.

Abstract of Dissertation presented to COPPE/UFRJ as a partial fulfillment of the requirements for the degree of Master of Science (M.Sc.)

SENSOR FAULT DETECTION AND DIAGNOSIS APPROACHES APPLIED TO AN AUTONOMOUS SOLAR-POWERED AIRCRAFT

Paulo Victor Padrão Lopes

February/2020

Advisor: Liu Hsu

Department: Electrical Engineering

Developed by Elektra Solar, an official spin-off of the DLR Institute for Robotics and Mechatronics (DLR-RMC), Elektra 2 Solar is a solar-powered autonomous aircraft designed to endure long distances as well as high altitudes. Currently, Elektra 2 Solar provides a simple limit-checking of certain measurements such as aircraft angular velocities and attitude angles. This oversimplified detection approach can hide faulty system behavior, which could lead to missed fault alarms and even disastrous consequences for the overall system. Once an undesired deviation is detected in primary IMU sensor, the reconfiguration procedure is to switch to backup IMU sensor. The main motivation of this work is to compare different IMU sensor fault detection and diagnosis (FDD) approaches to be applied to the Elektra 2 aircraft. The first proposed FDD approach is based on decoupled lateral and longitudinal linear models of the aircraft in combination with the design of Kalman filters for residual generation. An adaptive threshold technique (ATLMS) is used for fault detection. The second proposed FDD approach is based on the kinematic model of the aircraft in combination with an extended Kalman filter for residual generation. A decision table based on the alarm flag activation sequence is used for fault diagnosis regarding the first two approaches. The third FDD approach is a model-free approach based on principal component analysis. Contributions to squared prediction error are used for fault diagnosis. Finally, a fourth FDD strategy is developed taken into account the major advantages of the previous approaches. Simulation methodology covered different flight scenarios with different additive faults applied to measurements of roll and pitch rates as well as aircraft longitudinal acceleration. Real flight data from nominal operation experiments was used for validation purposes.

Contents

List of Figures

List of Tables

List of Symbols and Acronyms

Acronyms

AFAS Alarm Flag Activation Sequence

AFIS Adaptive Fuzzy Inference System

AGL Altitude above Ground

AMSL Altitude above Mean-Sea-Level

AoA Angle of Attack

AoA-L Left Angle of Attack Sensor

AoA-R Right Angle of Attack Sensor

ATLMS Least Mean Square-based Adaptive Threshold

CoG Center of Gravity

CoM Center of Mass

DLR German Aerospace Center

ECEF Earth-Centered Earth-Fixed

EGM96 Earth Gravitational Model 1996

EKF Extended Kalman Filter

EoM Equations of Motion

FDD Fault Detection and Diagnosis

FFT Fast Fourier Transform

FT2019 Aerospace Technology Congress 2019

GLRT Generalized Likelihood Ratio Test

GPS Global Positioning System

H.O.T Higher Order Terms

ICAR International Conference on Advanced Robotics

ICAS Congress of the International Council of the Aeronautical Sciences

IFAC International Federation of Automatic Control

IMU Inertial Measurement Unit

MSE Mean Squared Error

NED North-East-Down Reference Frame

NN Neural Network

OKID Observer/Kalman Filter Identification

PC Principal Component

PCA Principal Component Analysis

PLS Partial Least Square

RLS Recursive Least Square

RMC Institute for Robotics and Mechatronics

SI International System of Units

SPE Squared Prediction Error

SPRT Sequential Probability Ratio Test

SVM Support Vector Machine

TDR True Detection Rate

UAV Unmanned Aerial Vehicle

UTC Universal Time Coordinate

WGS84 World Geodetic System 1984

WMM World Magnetic Model

WPD Wavelet Packet Decomposition

Symbols

α	Angle of Attack
β	Sideslip Angle
δ_a	Aileron Command
δ_e	Elevator Command
δ_f	Flap Command Control
δ_r	Rudder Command
δ_t	Thrust Command
$\frac{d\mathbf{h}}{dt_b}$	Time Derivative of Angular Momentum with respect to Body Frame $\mathcal{F}^b$
$\frac{d\mathbf{h}}{dt_i}$	Time Derivative of Angular Momentum with respect to Inertial Frame $\mathcal{F}^i$
$\frac{d\mathbf{v}}{dt_b}$	Time Derivative of the Aircraft Velocity in Body Frame $\mathcal{F}^b$
$\frac{d\mathbf{v}}{dt_i}$	Time Derivative of the Aircraft Velocity in Inertial Frame $\mathcal{F}^i$
$\hat{\mathbf{x}}_{k\|k-1}$	Discrete-Time Predicted State Estimate
$\hat{\mathbf{x}}_{k\|k}$	Discrete-Time Updated State Estimate
$\omega_{b/i}$	Aircraft Angular Velocity with respect to Inertial Frame $\mathcal{F}^i$
ϕ	Least Mean Square Algorithm Input Vector
$\tilde{\mathbf{y}}_k$	Discrete-Time Estimation Error
$\mathbf{A}_{lat}$	Aircraft Lateral State Matrix
$\mathbf{A}_{lon}$	Aircraft Longitudinal State Matrix
$\mathbf{B}_{lat}$	Aircraft Lateral Input Matrix
$\mathbf{B}_{lon}$	Aircraft Longitudinal Input Matrix
$\mathbf{C}_{lat}$	Aircraft Lateral Output Matrix
$\mathbf{C}_{lon}$	Aircraft Longitudinal Output Matrix
$\mathbf{f}$	Sum of External Forces acting on the Aircraft

$\mathbf{f}_a$ Aerodynamic Force

$\mathbf{f}_g$ Gravitational Force

$\mathbf{f}_p$ Force produced by the Propulsion System of the Aircraft

$\mathbf{F}_k$ Discrete-Time Jacobian of the State Transition Model

$\mathbf{h}$ Angular Momentum

$\mathbf{H}_k$ Discrete-Time Jacobian of the Observation Model

$\mathbf{I}$ Identity Matrix

$\mathbf{J}$ Inertia Matrix

$\mathbf{K}_k$ Discrete-Time Kalman Gain

$\mathbf{m}$ Sum of All Externally Applied Moments

$\mathbf{m}_a$ Aerodynamic Moment

$\mathbf{m}_p$ Moment produced by the Propulsion System of the Aircraft

$\mathbf{P}$ PCA Algorithm Transformation Data Matrix

$\mathbf{P}_0$ Initial Covariance Matrix

$\mathbf{P}_{k|k-1}$ Discrete-Time Predicted Covariance Estimate

$\mathbf{P}_{k|k}$ Discrete-Time Updated Covariance Estimate

$\mathbf{Q}_k$ Discrete-Time Covariance Matrix of Process Noise

$\mathbf{R}_k$ Discrete-Time Covariance Matrix of Measurement Noise

$\mathbf{r}_{lat}$ Residual Vector from Aircraft Lateral Dynamics

$\mathbf{r}_{lon}$ Residual Vector from Aircraft Longitudinal Dynamics

$\mathbf{T}$ PCA Algorithm Reduced Data Matrix

$\mathbf{u}^*$ Trimmed System Input Vector

$\mathbf{u}$ System Input Vector

$\mathbf{u}_k$ Discrete-Time Input Vector

$\mathbf{u}_{lat}$ Aircraft Lateral Input Vector

$\mathbf{u}_{lon}$ Aircraft Longitudinal Input Vector

$\mathbf{v}_k$ Output Gaussian Noise Sequence

$\mathbf{w}$ Least Mean Square Algorithm Weight Vector

$\mathbf{w}_k$ Input Gaussian Noise Sequence

$\mathbf{X}^*$ PCA Algorithm Back-transformed Data Matrix

$\mathbf{x}^*$ Trimmed System State Vector

$\mathbf{X}$ PCA Algorithm Data Matrix

$\mathbf{x}$ System State Vector

$\mathbf{x}_k$ Discrete-Time State Vector

$\mathbf{x}_{lat}$ Aircraft Lateral State Vector

$\mathbf{x}_{lon}$ Aircraft Longitudinal State Vector

$\mathbf{y_m}$ Measured Output Vector

$\mathbf{y}$ System Output Vector

$\mathbf{y}_f$ Faulty System Output Vector

$\mathbf{y}_k$ Discrete-Time Output Vector

$\mathbf{y}_{lat_m}$ Measured Lateral Output Vector

$\mathbf{y}_{lat}$ Aircraft Lateral Output Vector

$\mathbf{y}_{lon_m}$ Measured Longitudinal Output Vector

$\mathbf{y}_{lon}$ Aircraft Longitudinal Output Vector

$\mathcal{F}^a$ Aerodynamic Reference Frame

$\mathcal{F}^b$ Body Reference Frame

$\mathcal{F}^i$ Inertial Reference Frame

$\mathcal{H}_0$ Normal Mode Hypothesis

$\mathcal{H}_1$ Faulty Mode Hypothesis

μ ATLMS Convergence Rate

Ω_{prop} Propeller Speed

ϕ Roll Angle

ψ Yaw Angle

ρ Air Density

τ Angular Velocity of the Aircraft Motor

θ Pitch Angle

θ_{max} Maximum Pitch Angle

a ATLMS Sensitivity Factor

AF_i Alarm Flag of Measurement $i = V_a$, α, β, p, q, r, ϕ, θ, ψ, h

AF_{lat} Alarm Flag from Aircraft Lateral Dynamics

AF_{lon} Alarm Flag from Aircraft Longitudinal Dynamics

Alt Altitude

AR Wing Aspect Ratio

b Wing Span

c Mean Aerodynamic Chord of the Wing

C_D Drag Coefficient

C_i Contribution of measurement residual i to squared predicition error

C_L Lift Coefficient

C_l Roll Coefficient

C_m Pitch Coefficient

C_n Yaw Coefficient

c_x shorthand notation for $cos\, x$

C_Y Sideforce Coefficient

C_{D_0} Minimum Drag Coefficient

$C_{D_{\delta a}}$ Variation of C_D with respect to Aileron Command

$C_{D_{\delta e}}$ Variation of C_D with respect to Elevator Command

$C_{D_{\delta f}}$ Variation of C_D with respect to Flap Command

$C_{D_{\delta r}}$ Variation of C_D with respect to Rudder Command

$C_{D_{Mach}}$ Variation of C_D with respect to Mach Number

C_{L_0} Lift at minimum drag

C_{L_α} Variation of C_L with respect to the Angle of Attack

C_{l_β} Variation of C_l with respect to Sideslip Angle

$C_{l_{\delta a}}$ Variation of C_l with respect to Aileron Command

$C_{L_{\delta e}}$ Variation of C_L with respect to Elevator Command

$C_{L_{\delta f}}$ Variation of C_L with respect to Flap Command

$C_{l_{\delta r}}$ Variation of C_l with respect to Rudder Command

C_{l_p} Variation of C_l with respect to Roll Rate

C_{L_q} Variation of C_L with respect to the Pitch Rate

C_{l_r} Variation of C_l with respect to Yaw Rate

$C_{L_{\dot{\alpha}}}$ Variation of C_L with respect to the Time Derivative of the Angle of Attack

$C_{L_{Mach}}$ Variation of C_L with respect to Mach Number

C_{m_0} Pitch Moment at Zero Angle of Attack

C_{m_α} Variation of C_m with respect to Angle of Attack

$C_{m_{\delta e}}$ Variation of C_m with respect to Elevator Command

$C_{m_{\delta f}}$ Variation of C_m with respect to Flap Command

C_{m_q} Variation of C_m with respect to Pitch Rate

$C_{m_{\dot{\alpha}}}$ Variation of C_m with respect to the Time Derivative of the Angle of Attack

$C_{m_{Mach}}$ Variation of C_m with respect to Mach Number

C_{n_β} Variation of C_n with respect to Sideslip Angle

$C_{n_{\delta a}}$ Variation of C_n with respect to Aileron Command

$C_{n_{\delta r}}$ Variation of C_n with respect to Rudder Command

C_{n_p} Variation of C_n with respect to Roll Rate

C_{n_r} Variation of C_n with respect to Yaw Rate

C_{prop} Aerodynamic Coefficient of the Propeller

C_{Y_β} Variation of C_Y with respect to Sideslip Angle

$C_{Y_{\delta a}}$ Variation of C_Y with respect to Aileron Command

$C_{Y_{\delta r}}$ Variation of C_Y with respect to Rudder Command

C_{Y_p} Variation of C_Y with respect to Roll Rate

C_{Y_r} Variation of C_Y with respect to Yaw Rate

e_0 ATLMS Safety Offset

e_w Wing Efficiency Factor

f Fault

f_{abrupt} Abrupt fault

f_{drag} Drag Force

$f_{incipient}$ Incipient fault

f_{lift} Lift Force

g Gravitational Acceleration

g_i Sum of measurement residual i

h^* Desired Aircraft Altitude

J_x Moment of Inertia in with respect to x-axis

J_y Moment of Inertia in with respect to y-axis

J_z Moment of Inertia in with respect to z-axis

J_{xz} Product of Inertia in with respect to x and z axes

k_{motor} Motor Efficiency Constant

k_{T_p} Propeller Constant

Lat	Latitude
Lon	Longitude
m	Aircraft Mass
m_{f_x}	Magnetic Field in x direction
m_{f_y}	Magnetic Field in y direction
m_{f_z}	Magnetic Field in z direction
p	Roll rate measured along x in $\mathcal{F}^b$
p_d	Inertial down position of the aircraft along z in $\mathcal{F}^i$
p_e	Inertial east position of the aircraft along y in $\mathcal{F}^i$
p_n	Inertial north position of the aircraft along x in $\mathcal{F}^i$
Q	Q Statistics
q	Pitch rate measured along y in $\mathcal{F}^b$
r	Yaw rate measured along z in $\mathcal{F}^b$
r_0	Insensitive Residual
r_1	Sensitive Residual
r_i	Residual of Measurement $i = V_a$, α, β, p, q, r, ϕ, θ, ψ, h
S	Surface Area of the Wing
s_x	shorthand notation for $sin\, x$
S_{prop}	Area of the Propeller
t	Time
T_s	Sampling Period
t_x	shorthand notation for $tan\, x$
u	Body frame velocity measured along x in $\mathcal{F}^b$
v	Body frame velocity measured along y in $\mathcal{F}^b$
V_a	Aircraft Airspeed

V_a^* Desired Aircraft Airspeed

V_g Aircraft Ground Speed

V_w Wind Speed

w Body frame velocity measured along z in $\mathcal{F}^b$

x x-axis

y y-axis

z z-axis

ATLMS_i Adaptive Threshold for measurement $i = V_a$, α, β, p, q, r, ϕ, θ, ψ

MSE_{r_i} Mean Squared Error for measurement $i = V_a$, α, β, ϕ, θ, ψ

Chapter 1

Introduction

Fault detection and diagnosis (FDD) is a significant task in the automatic control of complex systems. By definition, a fault is an unpermitted deviation of a particular characteristic of the system from the standard condition [4]. In many cases, the automatic supervision was mainly performed by limit checking of relevant process variables [7]. If a predefined threshold was exceeded, then an alarm was activated and the operator could act towards avoiding larger damages to the whole system [4].

Due to the increasing complexity of most technological processes, sophisticated sensors and the existence of modern signal processing systems, advanced methods of fault detection and diagnosis have been developed over the last decades. A wide range of applications - in particular safety-critical systems - require fault detection frameworks in order to guarantee system reliability and availability. The list of applications vary from commercial aircrafts to spacecrafts and from nuclear power plants to vibration monitoring of mechanical systems [8]. Most of fault detection methods focus on the following objectives:

- Early detection of small incipient or abrupt faults in sensors, actuators and components;
- Low sensitivity to external perturbations such as unknown inputs and noise;
- Minimization of false alarm and missed alarm rates;

- Framework development for fault-tolerant systems;

1.1 Bibliographical Review on Fault Detection Methods applied to Unmanned Aerial Vehicles

Over the past few years, much effort has been done regarding the development of fault detection and diagnosis strategies to unmanned aerial vehicles (UAV). Classic approaches using state/parameter estimation or observer-based schemes are widely exploited. In [9], observer-based residual generation have been used to detect faults in the z-axis component of the angular velocity of a gyroscope. In [10], observer/Kalman filter identification technique (OKID) was used to identify sensor faults directly from flight data of a MARVIN helicopter and [11] designed an optimal two-stage extended Kalman filter for IMU fault detection from simulated data of the ADMIRE aircraft benchmark model. In combination with the generalized likelihood ratio test (GLRT), an EKF-based scheme has been used for change detection in aircraft systems as presented in [12] and for GPS fault detection in [13]. In [14], a sliding-mode observer algorithm is developed for detecting, isolating and estimating sensor bias faults in gyroscope and accelerometer measurements. [15] and [16] analyze parity space fault detection methods and its applicability to detect, diagnosis and isolate sensor faults in inertial measurement sensors. Different from classic model-based sensor fault detection algorithms, [17] proposed an algorithm based on adaptive fuzzy inference system (AFIS) that could be used for real-time applications. With regard to signal-based fault detection methods, Fast Fourier Transform (FFT) and Wavelet Packet Decomposition (WPD) were used to indicate faults in a propulsion system of an UAV [18] and principal component analysis (PCA) is used for fault detection of redundant IMU sensors in [19].

In [20], fault detection approaches based on neural networks (NN) are used to detect injected sensor faults in UAVs. In [21], the weighting parameters of the Neural Network are updated by using an Extended Kalman Filter. Online adaptation of

these weighting parameters aims to detect abrupt, intermittent, and incipient faults accurately. A comparison between NN and EKF-based fault detection approaches is provided in [22]. In [23], Support Vector Machine (SVM) is used to classify faulty and nominal flight conditions in gyroscope measurements.

1.2 Motivation

On 10 March, 2019, 05:38 UTC (Universal Time Coordinate), a Boeing 737-8 (MAX) aircraft took off as a scheduled passenger flight from Addis Ababa, Ethiopia to Nairobi International Airport, Kenya. According to the Preliminary Aircraft Accident Investigation Report [1], the Digital Flight Data Recorder (DFDR) recorded a difference of about 60° between left and right angle of attack (AoA) sensor measurements during most of the flight (Fig. 1.1). At 05:44 UTC, the DFDR stopped recording. 157 people died. The aircraft was completely destroyed. Although an investigation is still ongoing, the discrepancy on the angle of attack sensors may have contributed significantly to the overall failure of the aircraft system.

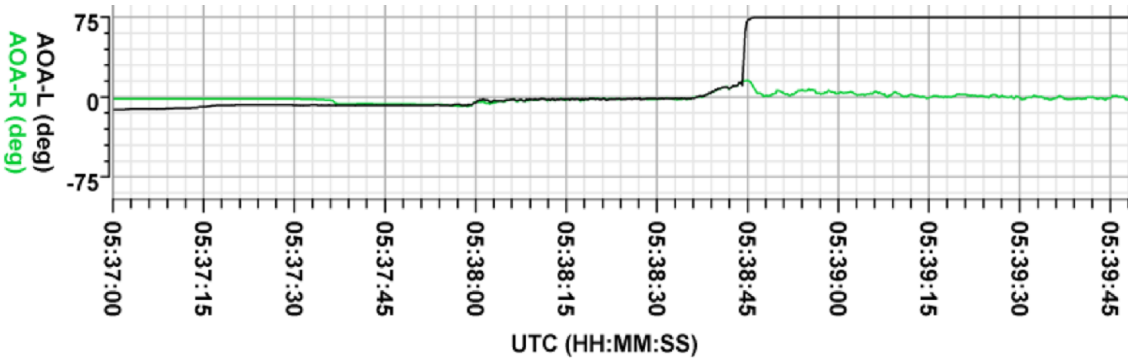

Figure 1.1: Angle of attack measurements of the Ethiopian Airlines Flight 302. AOA-L (black line) indicates the measurement of the left angle of attack sensor while AOA-R (green line) indicates the measurement of the right angle of attack sensor. Right after take off, an abrupt discrepancy is seen between these measurements. Both measurements were recorded in degrees [1].

Catastrophic events such the aforementioned one raise the attention to the

development of reliable fault management strategies in aircraft systems. Sensors are the most critical components for aircraft safety and it is well known that hardware redundancy plays a fundamental role in fault tolerant systems. However, differently from commercial aircrafts, redundant hardware sensor schemes may not always be available for unmanned aerial vehicles due to their size and cost limitations. Therefore, analytical redundancy approach arises as a suitable option for navigation sensor fault detection of such systems [13], [10], [24].

Developed by Elektra Solar, an official spin-off of the Institute for Robotics and Mechatronics at the German Aerospace Center (DLR-RMC), Elektra 2 is a solar-powered autonomous aircraft designed to endure long distances as well as surveillance purposes in high altitudes (fig. 1.2). The aircraft has two Xsens inertial measurement units (fig. 1.3), primary and backup, that provides aircraft accelerations, rates of turn and Earth-magnetic field data in three dimensions.

Currently, the Elektra 2 Solar aircraft provides limit-checking of raw measurements such as aircraft angular velocities and attitude angles. This oversimplified detection approach can hide faulty behaviors, making it difficult for early detection of small abrupt or incipient sensor faults. In the worst case scenario, it could lead to missed fault alarms and even disastrous consequences for the overall system. Once an undesired deviation is detected in primary IMU, the reconfiguration procedure is to switch to backup IMU.

The main motivation of this work is to develop a suitable IMU sensor fault detection and diagnosis module to be further applied to the Elektra 2 Aircraft in real flight experiments.

Figure 1.2: Elektra 2 Solar Aircraft. [2]

Figure 1.3: Xsens MTi-100 Series IMU. [3]

1.3 Scope of Work

The present work is the initial effort in order to define a suitable IMU sensor fault detection and diagnosis module to be further integrated to the Elektra 2 Aircraft. Choosing a suitable sensor fault detection and isolation strategy is the first step towards the development of a fault-tolerant control scheme (fig. 1.4).

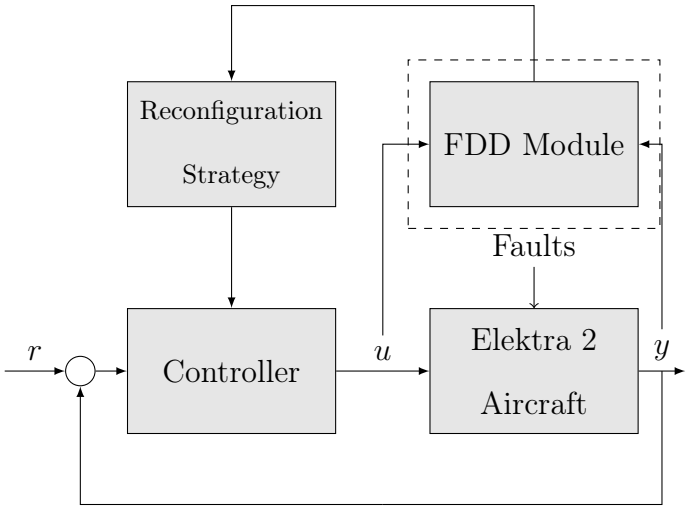

Figure 1.4: General Scheme of Fault Tolerant Control

The development of a fault detection and diagnosis module can be described by a general scheme presented in figure 1.5. Some of the tasks accomplished during the development phases are listed in table 1.1. This work covers the tasks from **FDD System Concept** to **FDD System Simulation Analysis**.

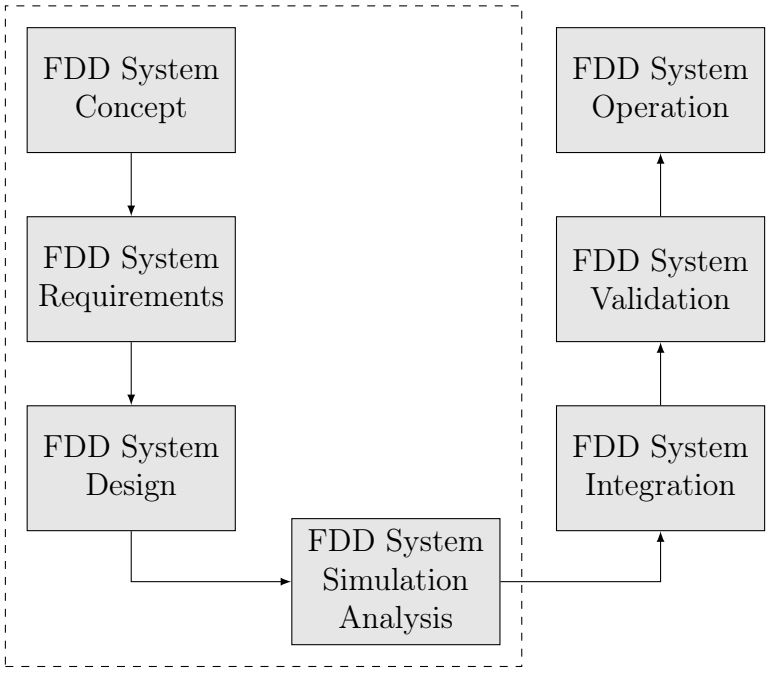

Figure 1.5: A general scheme for fault detection and diagnosis system development

1.4 Main Contribution

The main contribution of this work is the development and comparison of adequate IMU sensor fault detection and diagnosis approaches to be integrated to the Elektra 2 aircraft as presented in figure 1.6. Such approaches are further subdivided into model-based and data-driven.

Regarding the first IMU sensor fault detection approach, the so-called KF-ATLMS, residual generation for both longitudinal and lateral linear models of the aircraft is achieved based on the design of Kalman filters. The logarithmic likelihood ratio (LLR) is then used as a decision function to be evaluated with adaptive thresholds (ATLMS) for each of the aircraft measurements.

The second IMU sensor fault detection approach, the EKF-based approach, relies on a well-defined kinematic model of the aircraft. Due to its nonlinear nature, residual generation is based on the design of an extended Kalman filter (EKF). The mean squared error (MSE) of the residuals is then used as a decision function to be evaluated with fixed-value thresholds.

The third IMU sensor fault detection approach, the data-driven approach, is based on selected aircraft measurements such as angular rates, aircraft velocity and acceleration, and attitude angles. Principal component analysis (PCA) is used for residual generation. The squared prediction error (SPE) is used as a decision function to be evaluated with fixed-value thresholds.

A fourth IMU sensor fault detection strategy is presented taken into account the major advantages of the previous three approaches. It combines the aircraft kinematic equations with EKF-based residual generation as well as the ATLMS algorithm.

1.4.1 Publications

The efforts made in this work resulted in the following publications

- Aerospace Technology Congress 2019 - FT 2019 [25]

- 19^{th} International Conference on Advanced Robotics - ICAR 2019 [26]
- 32^{nd} Congress of the International Council of the Aeronautical Sciences - ICAS 2020 [27]

1.5 Thesis Organization

Chapter 1 presents the main motivation of this work, a bibliographical review of fault detection methods applied to unmanned aircrafts and the scope of the thesis. Chapter 2 presents an overview of the fault detection and diagnosis area. Chapter 3 is an overview of aircraft flight dynamics. It presents the six-degree-of-freedom, 12-state model for aircraft kinematics and dynamics and a brief discussion about aircraft control surfaces and reference frames. Chapter 4 introduces three different approaches to sensor fault detection and diagnosis. Besides that, a fourth fault detection strategy is developed based on the major advantages of the previous approaches. Chapter 5 presents the simulation results and comparison for different scenarios using the proposed fault detection approaches applied to the Elektra 2 Solar aircraft model. Finally, Chapter 6 presents the concluding remarks and future work.

Table 1.1: General Tasks for Fault Detection and Diagnosis (FDD) System Development

FDD System Concept:	
	- Data-driven vs. Model-based concepts; - Framework development for fault-tolerant and reconfigurable systems;
FDD System Requirements:	
	- Early detection of small incipient or abrupt IMU faults; - Decrease of false alarm and missed alarm rates; - Isolation and identification of IMU faults
FDD System Design:	
	- Development of fault models; - Development of residual generators; - Development of decision functions;
FDD System Simulation Analysis	
	- Simulation with different fault scenarios; - Comparison between FDD approaches;
FDD System Integration	
	- Code generation and upload to aircraft flight control computer;
FDD System Validation	
	- Real flight experiments with embedded FDD approach;

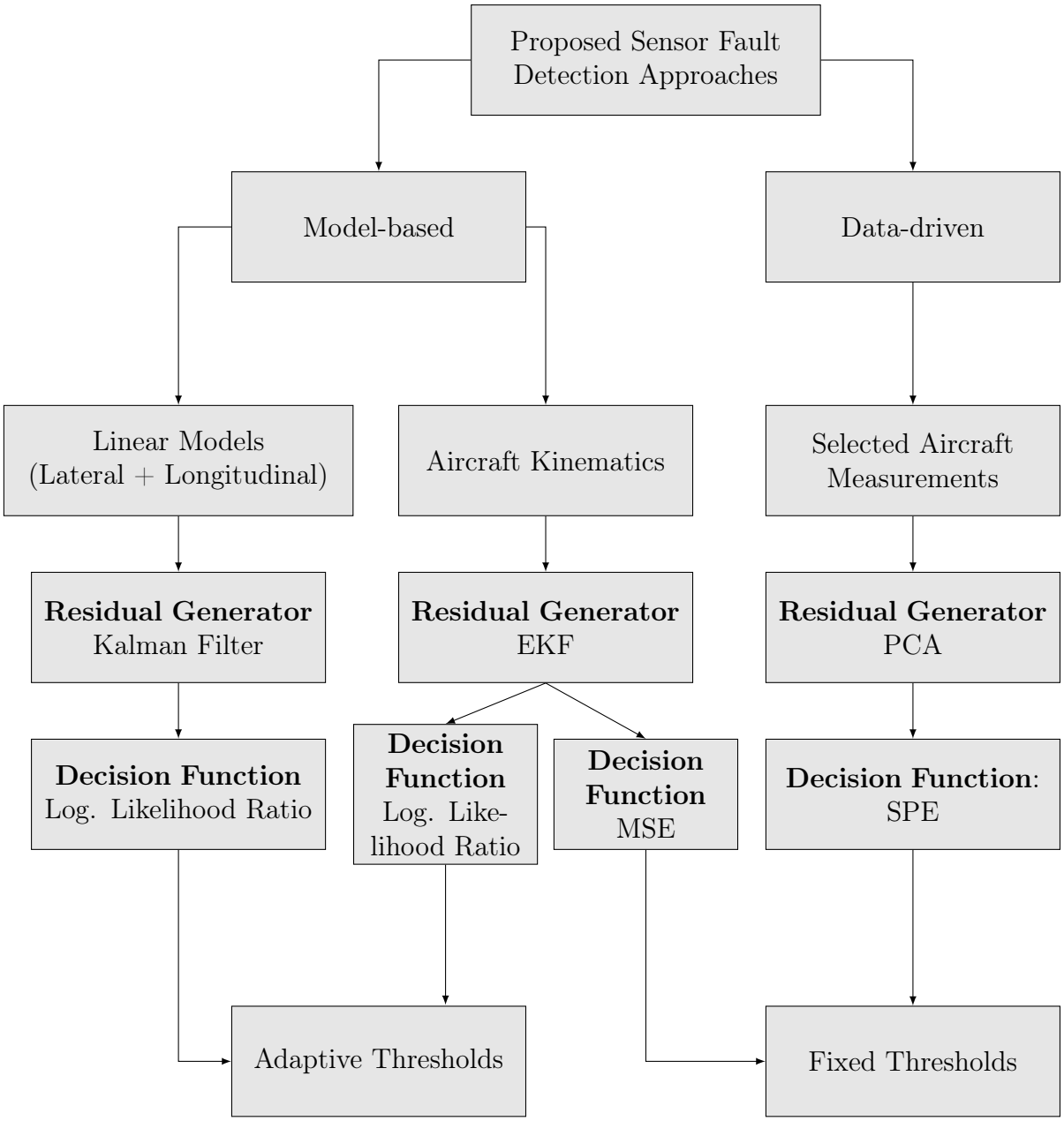

Figure 1.6: Proposed Fault Detection Approaches

Chapter 2

Overview of Fault Detection and Diagnosis

This chapter describes the terminology commonly used in the field of fault detection and diagnosis, different types of sensor faults, fault detection strategies, and fault diagnosis methods. It is mainly based on the work of [4].

2.1 Fault Detection Terminology

Although the literature is not always consistent with the terminology used in the field of fault detection and diagnosis, the International Federation of Automatic Control (IFAC) suggested some preliminary terms and definitions used in the present work [28].

- **States and Signals**
  - **Fault:** An unpermitted deviation of a characteristic or parameter of the system from the acceptable standard condition.
  - **Failure:** A permanent interruption of a system's ability to perform a required function under specified operating conditions.
  - **Residual:** A fault indicator, based on a deviation between measurements and model-equation-based computations.

  - **Symptom:** A change of an observable quantity from normal behavior.
  - **Alarm Flag:** A Boolean variable that assumes value 1 in case of fault detection. Otherwise, it is 0.

- **Functions**
  - **Fault detection:** Determination of faults present in a system and the time of detection.
  - **Fault isolation:** Determination of the location of a fault.
  - **Fault identification:** Determination of the size and time-variant behavior of a fault.
  - **Fault diagnosis** Determination of the kind, size, location and time of detection of a fault. Includes fault detection and identification.

- **Models**
  - **Quantitative model:** Use of static and dynamic relations among system variables and parameters in order to describe a system's behavior in quantitative mathematical terms.
  - **Qualitative model:** Use of static and dynamic relations among system variables in order to describe a system's behavior in qualitative terms such as causalities and IF–THEN rules.
  - **Analytical redundancy:** Use of more ways to determine a variable, where one way uses a mathematical process model in analytical form.

2.1.1 Basic Fault Types

According to [4], most faults can be classified into

- **Additive fault:** Influences a variable by the addition of the fault itself. They may represent, e.g., sensor offsets.

- **Multiplicative fault:** They can appear as parameter changes within a process.

The time dependency of such faults can be further classified into

- **Abrupt fault:** modelled as a step-wise function, it represents bias in the monitored signal.
- **Incipient fault:** modelled by ramp signals, it represents drift of the monitored signal.
- **Intermittent fault:** Combination of impulses or step functions with different amplitudes.

Figure 2.1 describes additive and multiplicative faults and figure 2.2 shows time-dependency characteristics of these faults.

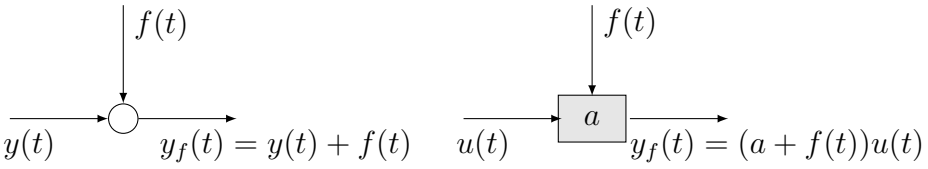

Figure 2.1: Basic Fault Models: (a) additive fault $f(t)$ for a measured signal $y(t)$; (b) multiplicative fault. Adapted from [4].

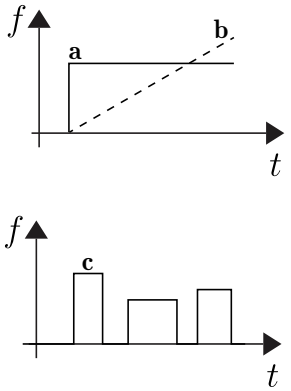

Figure 2.2: Time dependency of faults: (a) abrupt; (b) incipient; (c) intermittent. [4]

2.2 Classification of Fault Detection Methods

Most of the existing fault detection approaches can be organized into two different groups, as shown in figure 2.3: **(i)** the model-based approaches and **(ii)** data/signal-based ones [29], [30], [31]. Those groups are then subdivided into quantitative and qualitative methods. The most common model-based quantitative methods are based on state/parameter estimation and parity equations. On the other side, model-based qualitative methods take advantage of fault trees and structural graphs.

With respect to data-based quantitative methods, principal component analysis and neural networks are often used while fuzzy logic and pattern recognition are adopted in data-based qualitative methods. Comprehensive surveys about fault detection techniques and their applications are found in [32], [33], [34], [35], [7], [36], [37].

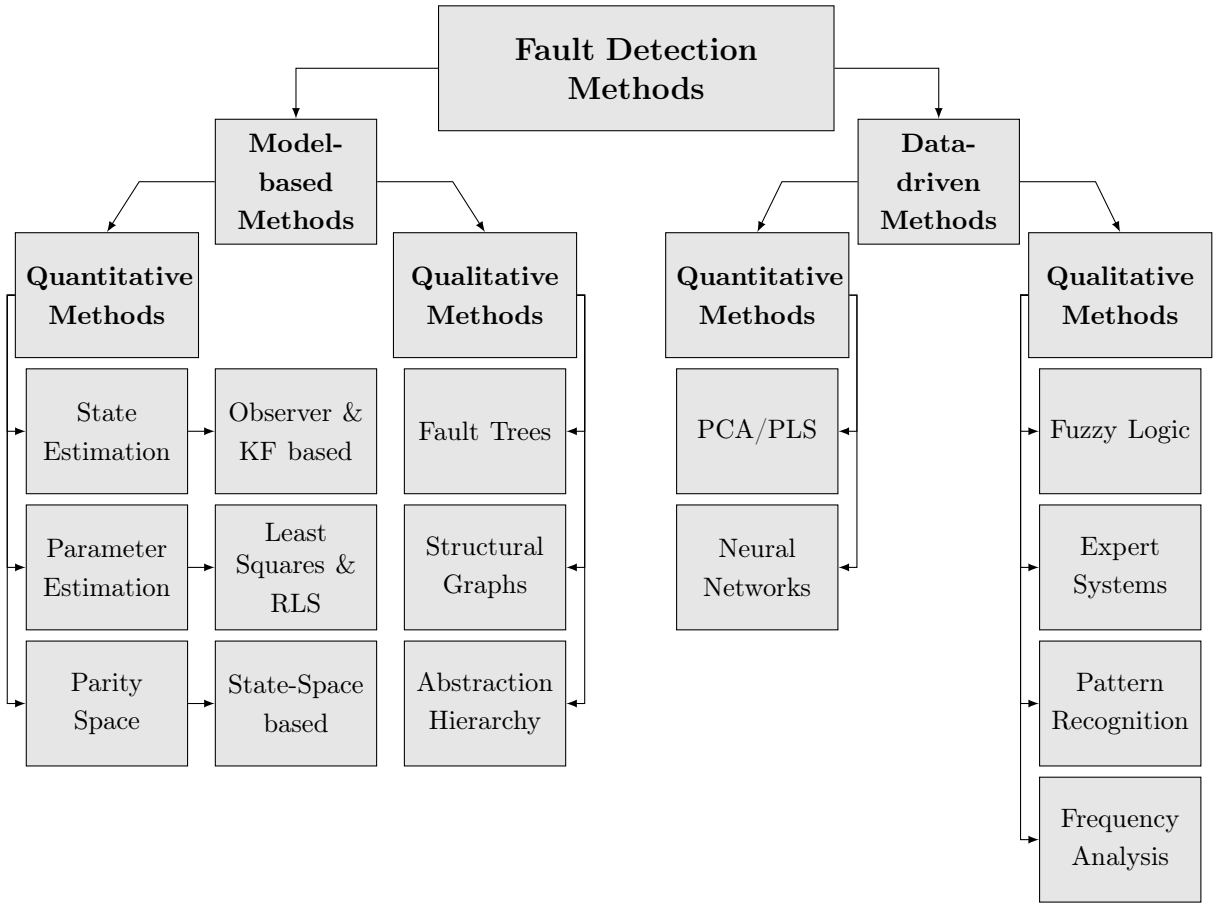

Figure 2.3: Classification of Fault Detection Methods. Adapted from [4]

2.3 Residual Generation and Decision Functions

An important part of fault detection algorithms is the generation of residuals [38], [39], and [40]. In general, the set of residuals is designed to be zero (ideal case) in the normal operating conditions and show significantly deviation from zero when a fault occurs. Relevant residual generation techniques such as fixed direction residuals, structured residuals [41] and structured hypothesis tests are often used. As described by [42], estimator-based methods for residual generation are also frequently applied to fault detection algorithms. One of the major difficulties in the development of residual generators is to achieve the decoupling of the inherent disturbances of the process. In this way, it is possible to avoid that an unknown event, which is not considered a fault, influences the detection of the faults themselves. Reviews on residual generation for fault diagnosis are presented in [43], [39], and [44]. Residual generation for linear systems is discussed in [40] and for non-linear systems in [45].

In general, the main task in fault detection schemes is to analyze the deflection of the residuals. For this purpose, the so-called decision functions are used. Such functions highlight the deflection of the residuals in case of fault occurrence. Some examples of widely used decision functions are residual absolute value, residual mean squared error, logarithmic likelihood ratio etc. In this way, a general structure for fault detection can be composed of a residual generator and a decision function as shown in figure 2.4. If the decision rules exceed a threshold-based application, a fault alarm is activated.

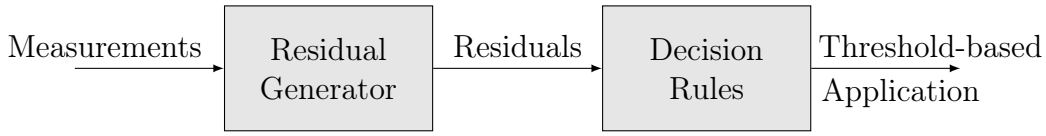

Figure 2.4: General Framework for Fault Detection.

2.4 Classification of Fault Diagnosis Methods

As presented in [4], fault propagation affects observable symptoms in a cause-effect fashion. In fault diagnosis methods, one has to proceed in the reverse way, i.e. determining which fault has occurred from observed symptoms. This characteristic is illustrated in figures 2.5 and 2.6.

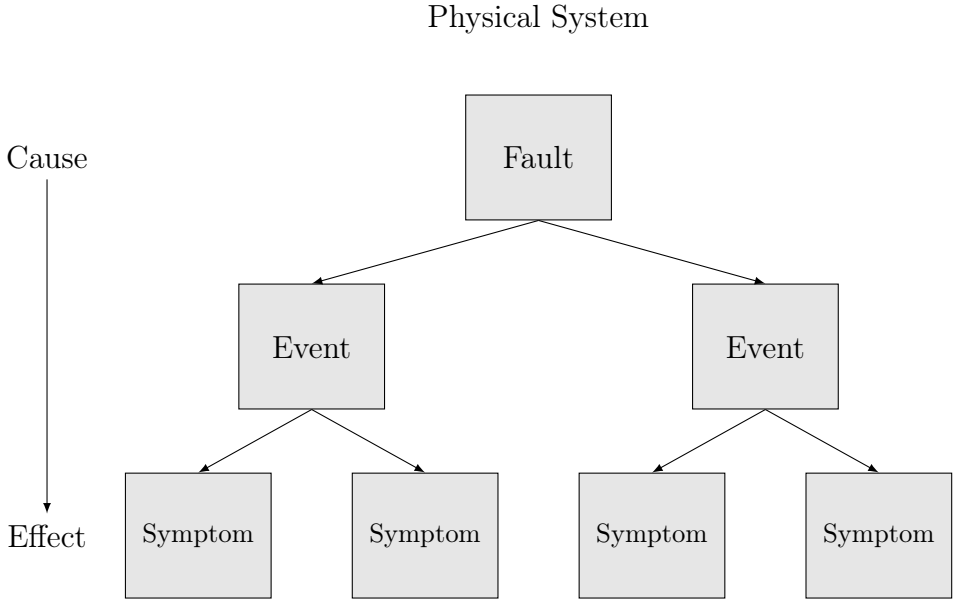

Figure 2.5: Fault-Symptom relationship in physical system: from faults to symptoms. Adapted from [4].

As presented in figure 2.7, typical fault diagnosis methods can be organized in two main groups: classification methods and inference methods. The former is then subdivided in pattern recognition methods, statistical classification, and density-based methods. The latter is subdivided in binary and approximate reasoning. Common tools for fault diagnosis are based on decision trees, fuzzy classifier, neural networks, Bayes classifiers, and so on.

According to [4], the main challenges in fault diagnosis are related to three different sources, such as (i) diagnosis knowledge representation, (ii) introduction of prior knowledge, and (iii) data size. In some cases, prior knowledge from experts is available, but the unification and representation of analytical and heuristic symptoms may not be trivial. Regarding experimental faulty data sets, they are rarely available or insufficient for fault diagnosis analysis. Besides that, a faulty

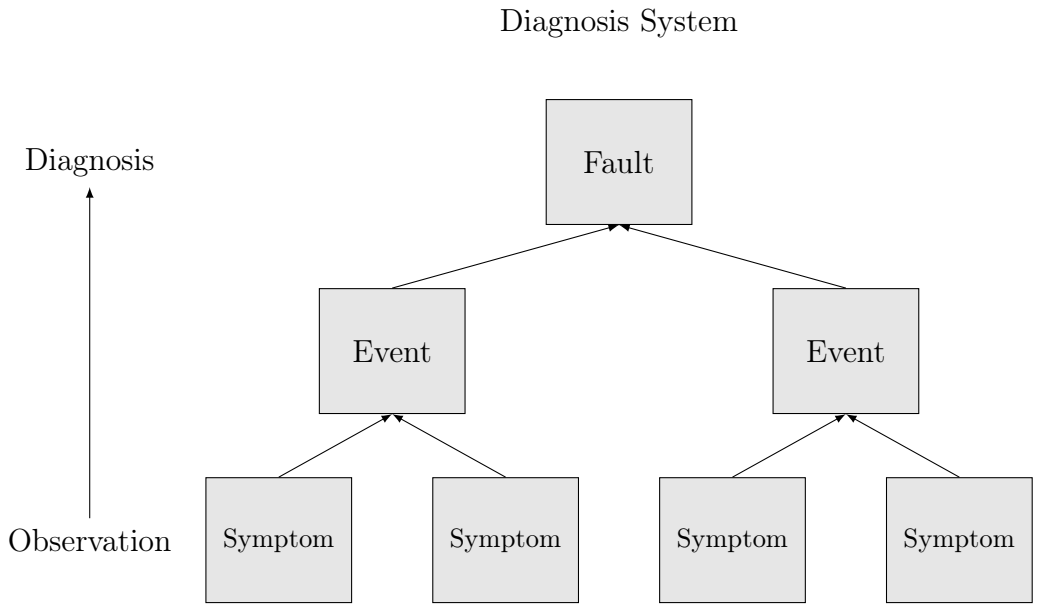

Figure 2.6: Fault-Symptom relationship in a fault diagnosis system: from symptoms to faults. Adapted from [4].

system could be dangerous and/or expensive to deal with. For these reasons, numerical simulations might be considered an adequate approach for fault detection an diagnosis analysis.

Extensive works about fault diagnosis methods and their applications are found in [32], [46], [47], [8], and [48].

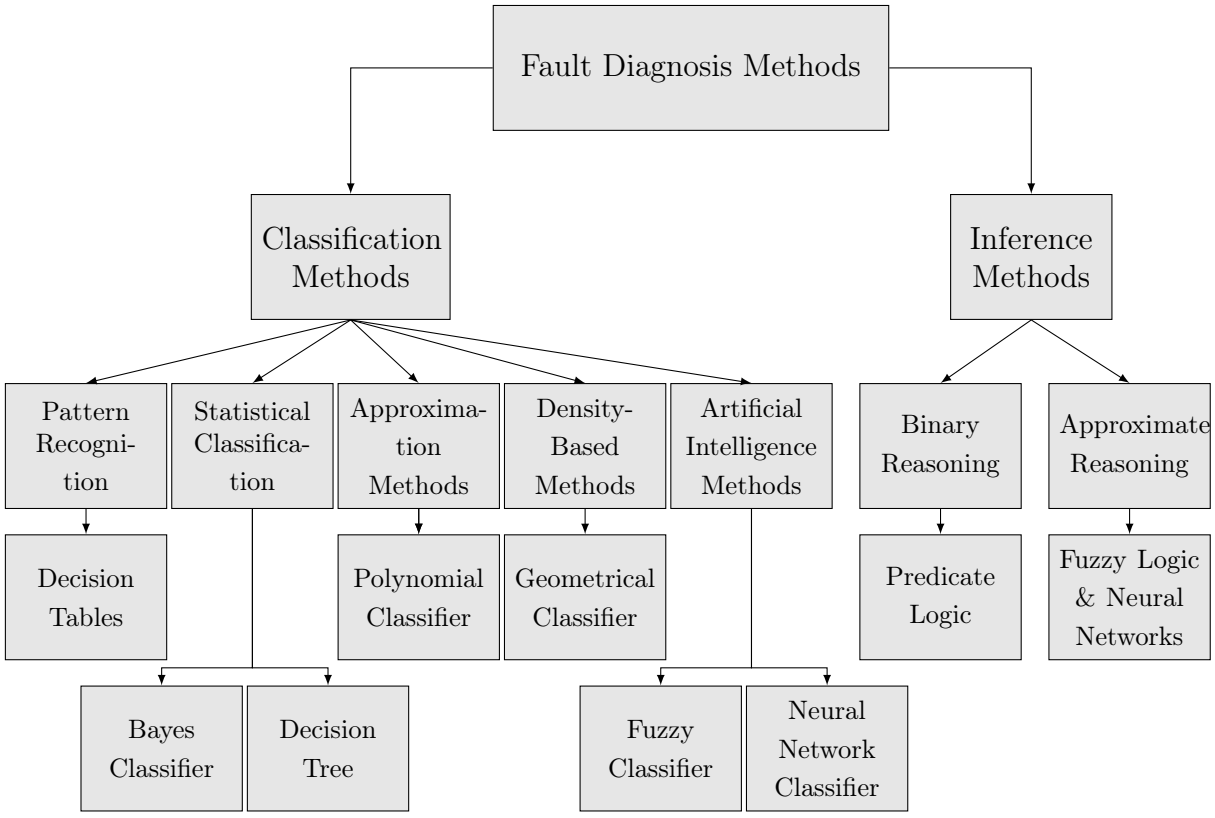

Figure 2.7: Typical Fault Diagnosis Methods. Adapted from [4].

Chapter 3

Overview of Aircraft Flight Theory

This chapter provides a summary of the introductory chapters of [49] regarding fixed-wing aircraft flight theory. It covers the different reference frames involved in describing aircraft position and orientation, presents the mathematical background of flight kinematic and dynamics, and introduces the main control surfaces of a fixed-wing aircraft.

3.1 Reference Frames

Reference frames are used to describe how different bodies are oriented relative to each other. Such descriptions vary from how the aircraft is oriented with respect to the Earth to how an on-board sensor is described relative to the aircraft. The following subsections present the most important coordinate systems for aircraft systems.

3.1.1 Inertial Reference Frame: $\mathcal{F}^i$

The inertial reference frame (or geodetic frame) $\mathcal{F}^i$ is a coordinate system used to relate the aircraft motion to the Earth. In the inertial frame, the x-direction points to the north, the y-direction to the east, and the z-direction points downward. The geodetic frame is denoted with subscript i and is sometimes referred to as north-east-down (NED) reference frame.

3.1.2 Body Reference Frame: $\mathcal{F}^b$

Aerodynamic forces and torques acting on the aircraft are commonly described in a body reference frame $\mathcal{F}^b$. The body-fixed reference frame has its origin in the center of gravity (CoG) of the aircraft. In this frame, the x-direction points forward to the aircraft vertical symmetry plane and the z-direction, perpendicular to x-axis, points downward with respect to the aircraft. The y-direction is perpendicular to the x-z plane and generally determined by the right-hand rule. The body reference frame is denoted with subscript b. Figures 3.1-3.3 describe aircraft yaw (ψ), roll (ϕ), and pitch (θ) angles provided by these axes rotations.

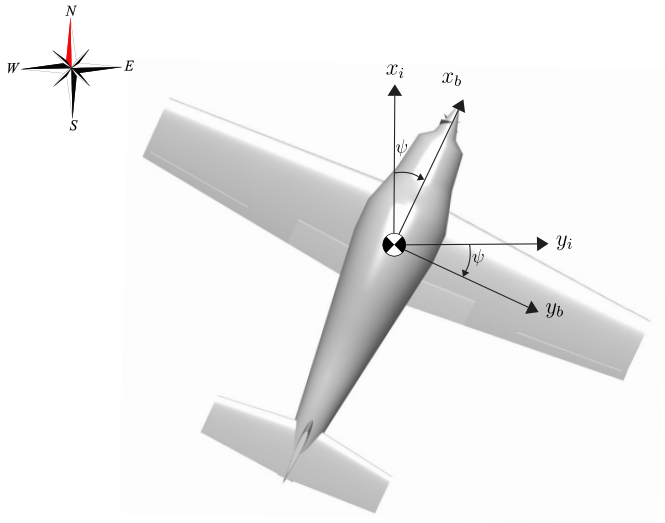

Figure 3.1: Aircraft yaw angle.

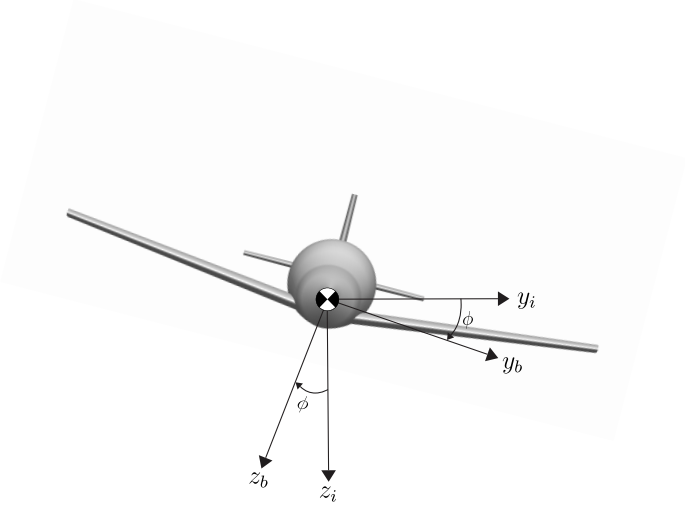

Figure 3.2: Aircraft roll angle.

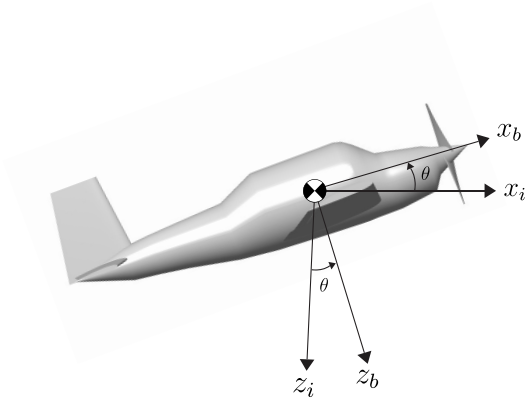

Figure 3.3: Aircraft pitch angle.

3.1.3 Aerodynamic Reference Frame: $\mathcal{F}^a$

In the aerodynamic reference frame $\mathcal{F}^a$, the x-axis points in the direction of the relative wind. In this coordinate system, two aerodynamic angles are defined: angle of attack α and sideslip angle β. The angle of attack α is the angle between the relative wind direction x_a and the longitudinal aircraft axis x_b and the sideslip angle β is related to the rotation of the aircraft longidutinal axis x_b from the relative wind direction x_a.

These angles are strongly associated with moments and forces acting on the aircraft. An increase of the angle of attack α results in an increase of the lift

coefficient of the aircraft. The sideslip angle β acts on the lateral dynamics of the aircraft. The aerodynamic reference frame is denoted with subscript a. Figures 3.4 and 3.5 describe the transformations from the body-fixed reference system $\mathcal{F}^b$ to the aerodynamic reference frame $\mathcal{F}^a$ and the definitions of the α and β angles.

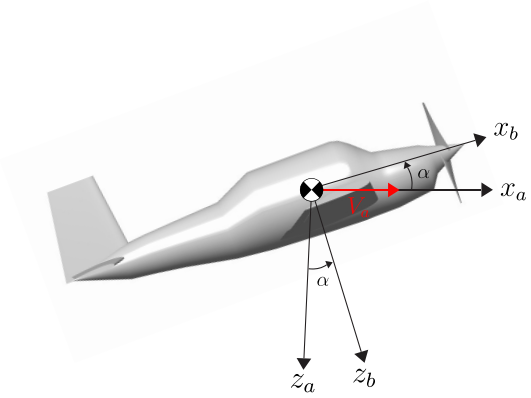

Figure 3.4: Aircraft Angle of Attack.

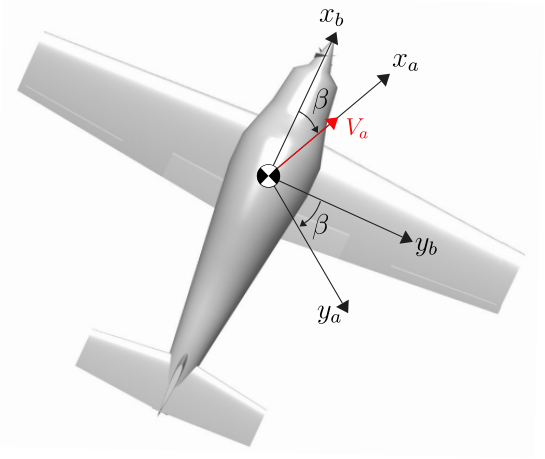

Figure 3.5: Aircraft Sideslip Angle.

3.2 Flight Kinematics and Dynamics

3.2.1 State Variables

Twelve state variables are here introduced in order to develop the aircraft kinematic and dynamic equations. The state variables are listed in Table 3.1.

Table 3.1: Aircraft State Variables

State Variable	Description
p_n	Inertial north position of the aircraft along x_i in $\mathcal{F}^i$
p_e	Inertial east position of the aircraft along y_i in $\mathcal{F}^i$
p_d	Inertial down position of the aircraft along z_i in $\mathcal{F}^i$
u	Body frame velocity measured along x_b in $\mathcal{F}^b$
v	Body frame velocity measured along y_b in $\mathcal{F}^b$
w	Body frame velocity measured along z_b in $\mathcal{F}^b$
ϕ	Roll angle defined with respect to $\mathcal{F}^i$ and $\mathcal{F}^b$
θ	Pitch angle defined with respect to $\mathcal{F}^i$ and $\mathcal{F}^b$
ψ	Yaw angle defined with respect to $\mathcal{F}^i$ and $\mathcal{F}^b$
p	Roll rate measured along x_b in $\mathcal{F}^b$
q	Pitch rate measured along y_b in $\mathcal{F}^b$
r	Yaw rate measured along z_b in $\mathcal{F}^b$

3.2.2 Aircraft Kinematics

The translational velocity of the aircraft is described with respect to the velocity components (u, v, w) in the body reference frame $\mathcal{F}^b$. However, the translational position is usually expressed with respect to the inertial frame $\mathcal{F}^i$. For this reason, the kinematic expression relating translational velocities and positions requires a rotational transformation. This relation is given by

$$\begin{pmatrix} \dot{p}_n \\ \dot{p}_e \\ \dot{p}_d \end{pmatrix} = \begin{pmatrix} c_\theta c_\psi & s_\phi s_\theta c_\psi - c_\phi s_\psi & c_\phi s_\theta c_\psi + s_\phi s_\psi \\ c_\theta s_\psi & s_\phi s_\theta s_\psi + c_\phi c_\psi & c_\phi s_\theta s_\psi + s_\phi s_\psi \\ -s_\theta & s_\phi c_\theta & c_\phi c_\theta \end{pmatrix} \begin{pmatrix} u \\ v \\ w \end{pmatrix} \tag{3.1}$$

where the shorthand notation $c_x \triangleq cos\, x$, $s_x \triangleq sin\, x$, and $t_x \triangleq tan\, x$ is used.

Regarding the angular rates (p, q, r) and angular positions (ϕ, θ, ψ), they are also expressed in terms of different coordinate frames. With the proper rotational transformations, the body-frame angular rates can be defined in terms of the derivatives of the Euler angles by

$$\begin{pmatrix} p \\ q \\ r \end{pmatrix} = \begin{pmatrix} 1 & 0 & -s_\theta \\ 0 & c_\phi & s_\phi c_\theta \\ 0 & -s_\phi & c_\phi c_\theta \end{pmatrix} \begin{pmatrix} \dot{\phi} \\ \dot{\theta} \\ \dot{\psi} \end{pmatrix} \tag{3.2}$$

Conversely,

$$\begin{pmatrix} \dot{\phi} \\ \dot{\theta} \\ \dot{\psi} \end{pmatrix} = \begin{pmatrix} 1 & s_\phi t_\theta & c_\phi t_\theta \\ 0 & c_\phi & -s_\phi \\ 0 & s_\phi / c_\theta & c_\phi / c_\theta \end{pmatrix} \begin{pmatrix} p \\ q \\ r \end{pmatrix} \tag{3.3}$$

3.2.3 Rigid-Body Dynamics

Translational Motion The translational motion of an aircraft can be derived through Newton's second law as

$$m \frac{d\mathbf{v}}{dt_i} = \mathbf{f} \tag{3.4}$$

where m is the mass of the aircraft, $\mathbf{f}$ is the sum of external forces acting on the aircraft and $\dfrac{d\mathbf{v}}{dt_i}$ is the time derivative of the aircraft velocity in the inertial frame $\mathcal{F}^i$.

The derivative of velocity in the inertial frame is related to the derivative in the body frame as

$$\frac{d\mathbf{v}}{dt_i} = \frac{d\mathbf{v}}{dt_b} + \omega_{b/i} \times \mathbf{v} \tag{3.5}$$

where $\omega_{b/i}$ is the angular velocity of the aircraft with respect to the inertial frame. Combining equations (3.4) and (3.5), it follows

$$m \left(\frac{d\mathbf{v}}{dt_b} + \omega_{b/i} \times \mathbf{v} \right) = \mathbf{f} \tag{3.6}$$

where $\mathbf{v} = (u,\, v,\, w)^T$, $\mathbf{w}_{b/i} = (p,\, q,\, r)^T$, and $\mathbf{f} \triangleq (f_x,\, f_y,\, f_z)^T$, all defined in body frame.

Rearranging (equation) 3.6,

$$\begin{pmatrix} \dot{u} \\ \dot{v} \\ \dot{w} \end{pmatrix} = \begin{pmatrix} rv - qw \\ pw - ru \\ qu - pv \end{pmatrix} + \frac{1}{m} \begin{pmatrix} f_x \\ f_y \\ f_z \end{pmatrix} \tag{3.7}$$

Rotational Motion The rotational motion of an aircraft is derived from Newton's second law as

$$\frac{d\mathbf{h}}{dt_i} = \mathbf{m} \tag{3.8}$$

where $\mathbf{h}$ is the angular momentum and $\mathbf{m} = (m_x\,, m_y\,, m_z)^T$ is the sum of all externally applied moments in x-y-z directions in inertial coordinate frame $\mathcal{F}^i$.

In body frame, equation (3.8) is expressed as

$$\frac{d\mathbf{h}}{dt_i} = \frac{d\mathbf{h}}{dt_b} + \omega_{b/i} \times \mathbf{h} = \mathbf{m} \tag{3.9}$$

For a rigid body, the angular momentum is defined as

$$\mathbf{h} \triangleq \mathbf{J}\omega_{b/i} \tag{3.10}$$

where $\mathbf{J}$ is the inertia matrix and is given by

$$\begin{aligned} \mathbf{J} &= \begin{pmatrix} \int (y^2 + z^2) dm & -\int xy\, dm & -\int xz\, dm \\ -\int xy\, dm & \int (x^2 + z^2) dm & -\int yz\, dm \\ -\int xz\, dm & -\int yz\, dm & \int (x^2 + y^2) dm \end{pmatrix} \\ &\triangleq \begin{pmatrix} J_x & -J_{xy} & -J_{xz} \\ -J_{xy} & J_y & -J_{yz} \\ -J_{xz} & -J_{yz} & J_z \end{pmatrix} \end{aligned} \tag{3.11}$$

The diagonal terms of $\mathbf{J}$ are called moments of inertia and the other terms are

called products of inertia. Generally speaking, the moments of inertia can be viewed as measures of the aircraft's tendency to oppose acceleration about a specific axis of rotation. The larger a moment of inertia is, the more the aircraft opposes the angular acceleration in that direction.

Combining equations (3.9) and (3.10),

$$\mathbf{J}\frac{d\omega_{b/i}}{dt_b} + \omega_{b/i} \times (\mathbf{J}\omega_{b/i}) = \mathbf{m} \tag{3.12}$$

.

The term $\frac{d\omega_{b/i}}{dt_b}$ can be rewritten as

$$\frac{d\omega_{b/i}}{dt_b} = \dot{\omega}_{b/i} = \begin{pmatrix} \dot{p} \\ \dot{q} \\ \dot{r} \end{pmatrix} \tag{3.13}$$

Rearranging equation (3.12), it follows that

$$\dot{\omega}_{b/i} = \mathbf{J}^{-1}[-\omega_{b/i} \times (\mathbf{J}\omega_{b/i}) + \mathbf{m}] \tag{3.14}$$

Under the assumption that the aircraft is symmetric about the plane x_b-z_b, the inertia matrix can be defined as

$$\mathbf{J} = \begin{pmatrix} J_x & 0 & -J_{xz} \\ 0 & J_y & 0 \\ -J_{xz} & 0 & J_z \end{pmatrix} \tag{3.15}$$

and its inverse is calculated as

$$\mathbf{J}^{-1} = \frac{\text{adj}(\mathbf{J})}{\det(\mathbf{J})}$$

$$= \frac{\begin{pmatrix} J_y J_z & 0 & J_y J_{xz} \\ 0 & J_x J_z - J_{xz}^2 & 0 \\ J_{xz} J_y & 0 & J_x J_y \end{pmatrix}}{J_x J_y J_z - J_{xz}^2 J_y} \tag{3.16}$$

$$= \begin{pmatrix} \frac{J_z}{\Gamma} & 0 & \frac{J_{xz}}{\Gamma} \\ 0 & \frac{1}{J_y} & 0 \\ \frac{J_{xz}}{\Gamma} & 0 & \frac{J_x}{\Gamma} \end{pmatrix}$$

where $\Gamma \triangleq J_x J_z - J_{xz}^2$. Defining the components of the externally applied moment about body frame axes (x_b, y_b, z_b) as $\mathbf{m}^b \triangleq (l, m, n)^T$, equation (3.12) can be rewritten as

$$\begin{pmatrix} \dot{p} \\ \dot{q} \\ \dot{r} \end{pmatrix} = \begin{pmatrix} \frac{J_z}{\Gamma} & 0 & \frac{J_{xz}}{\Gamma} \\ 0 & \frac{1}{J_y} & 0 \\ \frac{J_{xz}}{\Gamma} & 0 & \frac{J_x}{\Gamma} \end{pmatrix} \left[\begin{pmatrix} J_{xz} pq + (J_y - J_z) qr \\ J_{xz}(r^2 - p^2) + (J_z - J_x) pr \\ (J_x - J_y) pq - J_{xz} qr \end{pmatrix} + \begin{pmatrix} l \\ m \\ n \end{pmatrix} \right]$$

$$= \begin{pmatrix} \Gamma_1 pq - \Gamma_2 qr + \Gamma_3 l + \Gamma_4 n \\ \Gamma_5 pr - \Gamma_6 (p^2 - r^2) + \frac{1}{J_y} m \\ \Gamma_7 pq - \Gamma_1 qr + \Gamma_4 l + \Gamma_8 n \end{pmatrix} \tag{3.17}$$

where

$$
\begin{aligned}
\Gamma_1 &= \frac{J_{xz}(J_x - J_y + J_z)}{\Gamma} \\
\Gamma_2 &= \frac{J_z(J_z - J_y) + J_{xz}^2}{\Gamma} \\
\Gamma_3 &= \frac{J_z}{\Gamma} \\
\Gamma_4 &= \frac{J_{xz}}{\Gamma} \\
\Gamma_5 &= \frac{J_z - J_x}{J_y} \\
\Gamma_6 &= \frac{J_{xz}}{J_y} \\
\Gamma_7 &= \frac{(J_x - J_y)J_x + J_{xz}^2}{\Gamma} \\
\Gamma_8 &= \frac{J_x}{\Gamma}.
\end{aligned}
\tag{3.18}
$$

.

3.3 Airspeed, Wind Speed, and Ground Speed

While inertial forces acting on the aircraft are described with velocities and accelerations relative to the inertial frame, the aerodynamic forces are described with the velocity relative to the aerodynamic frame. The velocity described with respect to the inertial frame $\mathcal{F}^i$ is called ground speed (V_g) and the velocity described by the aerodynamic reference frame $\mathcal{F}^a$ is called airspeed (V_a). In the absence of wind, these velocities are the same.

$$V_a = V_g \tag{3.19}$$

Taking into account the wind velocity (V_w) relative to the inertial frame, the relationship between airspeed, ground speed and wind speed is defined as

$$V_a = V_g - V_w \tag{3.20}$$

With a suitable rotational transformation, the ground speed velocity vector can be expressed in terms of the airspeed, angle of attack and sideslip angle as

$$\begin{pmatrix} u \\ v \\ w \end{pmatrix} = V_a \begin{pmatrix} c_\alpha \, c_\beta \\ s_\beta \\ s_\alpha \, c_\beta \end{pmatrix} \tag{3.21}$$

Conversely,

$$\begin{aligned} V_a &= \sqrt{u^2 + v^2 + w^2} \\ \alpha &= tan^{-1}\left(\frac{w}{u}\right) \\ \beta &= sin^{-1}\left(\frac{v}{V_a}\right) \end{aligned} \tag{3.22}$$

The expressions in equation (3.22) are of great importance once aerodynamic forces and moments are described in terms of V_a, α, and β.

3.4 Flight Forces and Moments

Lift, drag, weight and thrust are the four fundamental forces acting on a flying aircraft. Given that a fluid flowing through the surface of a rigid body exerts a force on it, the **lift force** is the component of this force that is perpendicular to the incoming flow. It creates a pressure differential between upper and lower surfaces of the body. If enough lift is generated by these surfaces, it can overcome aircraft **weight** and flight is achieved. In contrast, the **drag force** opposes the forward movement generated by the **thrust**, acting as a type of fluid resistance. Lift and drag forces depend on the aircraft design and are affected by the shape of the airfoils and fuselage, air density, flight velocity, etc. Figure 3.6 shows a scheme of these forces acting on an aircraft.

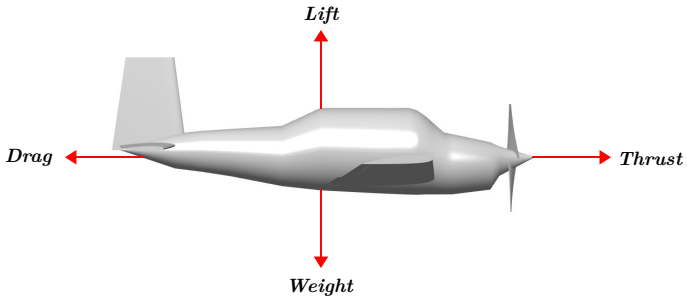

Figure 3.6: Fundamental Forces acting on an Aircraft.

The total force $\mathbf{f}$ and moment $\mathbf{m}$ acting on the aircraft come from three different sources: gravity ($\mathbf{f}_g$), aerodynamics ($\mathbf{f}_a$, $\mathbf{m}_a$), and propulsion ($\mathbf{f}_p$, $\mathbf{m}_p$). Equations (3.23) and (3.24) show the total force and moment.

$$\mathbf{f} = \mathbf{f}_g + \mathbf{f}_a + \mathbf{f}_p \tag{3.23}$$

$$\mathbf{m} = \mathbf{m}_a + \mathbf{m}_p \tag{3.24}$$

In body frame $\mathcal{F}^b$, the gravity force $\mathbf{f}_g^b$ acting on the center of mass (CoM) is given by

$$\mathbf{f}_g^b = \begin{pmatrix} -mg\, s_\theta \\ mg\, c_\theta\, s_\phi \\ mg\, c_\theta\, c_\phi \end{pmatrix} \tag{3.25}$$

The longitudinal motion of the aircraft is described in terms of lift and drag forces, as well as the pitching moment. Besides that, the lateral motion of the aircraft is described by the side force, rolling and yawing moments. Additionally, the structural design of the aircraft influences the flight dynamics by means of a set of aerodynamic coefficients, namely

$$\begin{cases} \text{Drag} & C_D = f_D(\alpha, q, \delta_e) \\ \text{Lift} & C_L = f_L(\alpha, q, \delta_e) \\ \text{Sideforce} & C_Y = f_Y(\beta, p, r, \delta_a, \delta_r) \\ \text{Roll} & C_l = f_l(\beta, p, r, \delta_a, \delta_r) \\ \text{Pitch} & C_m = f_m(\alpha, q, \delta_e) \\ \text{Yaw} & C_n = f_n(\beta, p, r, \delta_a, \delta_r) \end{cases}$$

where the coefficients depend on the angular velocities, control surfaces (δ_e,δ_a,δ_r) and aerodynamic angles (α, β).

The longitudinal forces and moment about y_b axis denoted by m are defined in body frame $\mathcal{F}^b$ as

$$f_{lift} = \frac{1}{2}\rho V_a^2 S C_L(\alpha, q, \delta_e) \tag{3.26}$$

$$f_{drag} = \frac{1}{2}\rho V_a^2 S C_D(\alpha, q, \delta_e) \tag{3.27}$$

$$m = \frac{1}{2}\rho V_a^2 S c C_m(\alpha, q, \delta_e) \tag{3.28}$$

Once lift and drag forces are expressed in the aerodynamic frame $\mathcal{F}^a$, a rotational transformation by the angle of attack α is needed to express these forces in body frame $\mathcal{F}^b$ as

$$\begin{pmatrix} f_x \\ f_z \end{pmatrix} = \begin{pmatrix} c_\alpha & -s_\alpha \\ s_\alpha & c_\alpha \end{pmatrix} \begin{pmatrix} -f_{drag} \\ -f_{lift} \end{pmatrix} \tag{3.29}$$

The lateral forces and moments about x_b and z_b axes in body frame $\mathcal{F}^b$ are defined as

$$f_y = \frac{1}{2}\rho V_a^2 S C_Y(\beta, p, r, \delta_a, \delta_r) \tag{3.30}$$

$$l = \frac{1}{2}\rho V_a^2 S b C_l(\beta, p, r, \delta_a, \delta_r) \tag{3.31}$$

$$n = \frac{1}{2}\rho V_a^2 S C_n(\beta, p, r, \delta_a, \delta_r) \tag{3.32}$$

where ρ is the air density, V_a denotes the aircraft airspeed, S is the surface area of the wing, c corresponds to the mean aerodynamic chord of the wing, and b is the wing span as presented in figure 3.7.

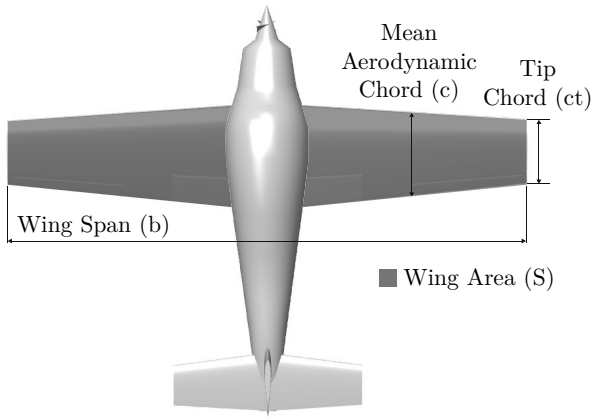

Figure 3.7: Aircraft Wing Parameters.

The force produced by the propulsion system of the aircraft is given by

$$\mathbf{f}_p = \frac{1}{2}\rho S_{prop} C_{prop} \begin{pmatrix} (k_{motor}\delta_t) - V_a^2 \\ 0 \\ 0 \end{pmatrix} \tag{3.33}$$

and the moments due to the propulsion system are

$$\mathbf{m}_p = \begin{pmatrix} -k_{T_p}\Omega_{prop}^2 \\ 0 \\ 0 \end{pmatrix} \tag{3.34}$$

where S_{prop} is the area of the propeller, C_{prop} corresponds to the aerodynamic coefficient of the propeller, δ_t is the control signal denoting the throttle deflection,

k_{motor} represents the motor efficiency constant, Ω_{prop} is the propeller speed, and k_{T_p} is a propeller constant determined by experimental procedure.

3.5 Flight Control Surfaces

The three main control surfaces of a standard fixed wing aircraft are ailerons, rudder, and elevator (figs. 3.8, 3.9, and 3.10). The ailerons are responsible for the directional control of the aircraft. It means that a positive aileron input results in a downward movement of the right aileron and upward movement of the left aileron. As a result, a negative rolling moment is created. The lift vector is then tilted and a side force that changes the path angle is created. The aileron deflection is denoted by δ_a.

The rudder surface is also related to the lateral motion of the aircraft. A yawing moment is created with rudder commands. It means that a positive rudder input results in a rudder turn to the left. As a result, a change in the heading and sideslip angle of the aircraft is achieved. For this reason, rudders and ailerons are usually commanded together in order to coordinate the aircraft turn, making the nose point in the direction of flight. The rudder deflection is denoted by δ_r.

The elevators are responsible to create a pitching moment. It means that a positive elevator input tilts the elevators downward, resulting in a negative pitching moment. It is important to notice that altitude changes are strongly coupled with velocity changes in aircraft. For this reason, an elevator input will not only affect the pitch angle, but also the velocity. The elevator deflection is denoted by δ_e.

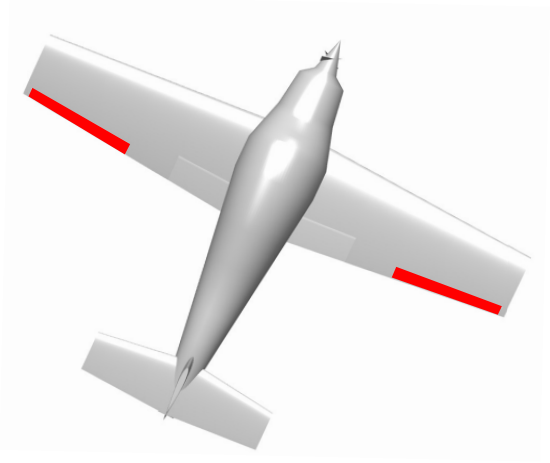

Figure 3.8: Aircraft control surfaces: Ailerons.

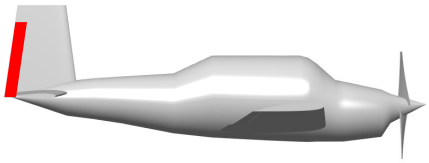

Figure 3.9: Aircraft control surfaces: Rudder.

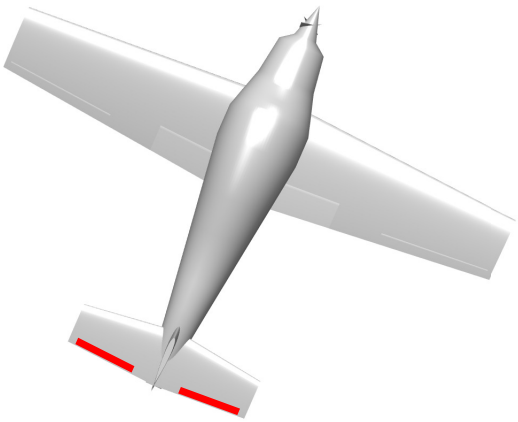

Figure 3.10: Aircraft control surfaces: Elevators.

3.5.1 Chapter Summary

In this chapter, 3 different coordinate frames were introduced, namely:

- Inertial Reference Frame $\mathcal{F}^i$;
- Body Reference Frame $\mathcal{F}^b$;

- Aerodynamic Reference Frame F^a.

Then, the six-degree-of-freedom, 12-state model for the aircraft kinematics and dynamics are summarized as follows

$$\begin{pmatrix} \dot{p}_n \\ \dot{p}_e \\ \dot{p}_d \end{pmatrix} = \begin{pmatrix} c_\theta c_\psi & s_\phi s_\theta c_\psi - c_\phi s_\psi & c_\phi s_\theta c_\psi + s_\phi s_\psi \\ c_\theta s_\psi & s_\phi s_\theta s_\psi + c_\phi c_\psi & c_\phi s_\theta s_\psi + s_\phi s_\psi \\ -s_\theta & s_\phi c_\theta & c_\phi c_\theta \end{pmatrix} \begin{pmatrix} u \\ v \\ w \end{pmatrix} \tag{3.35}$$

$$\begin{pmatrix} \dot{u} \\ \dot{v} \\ \dot{w} \end{pmatrix} = \begin{pmatrix} rv - qw \\ pw - ru \\ qu - pv \end{pmatrix} + \begin{pmatrix} a_x \\ a_y \\ a_z \end{pmatrix} \tag{3.36}$$

$$\begin{pmatrix} \dot{\phi} \\ \dot{\theta} \\ \dot{\psi} \end{pmatrix} = \begin{pmatrix} 1 & s_\phi t_\theta & c_\phi t_\theta \\ 0 & c_\phi & -s_\phi \\ 0 & s_\phi / c_\theta & c_\phi / c_\theta \end{pmatrix} \begin{pmatrix} p \\ q \\ r \end{pmatrix} \tag{3.37}$$

$$\begin{pmatrix} \dot{p} \\ \dot{q} \\ \dot{r} \end{pmatrix} = \begin{pmatrix} \Gamma_1 pq - \Gamma_2 qr + \Gamma_3 l + \Gamma_4 n \\ \Gamma_5 pr - \Gamma_6 (p^2 - r^2) + \dfrac{1}{J_y} m \\ \Gamma_7 pq - \Gamma_1 qr + \Gamma_4 l + \Gamma_8 n \end{pmatrix} \tag{3.38}$$

Finally, models for forces and moments due to gravity, aerodynamics, and propulsion were also derived and are summarized below and Elektra Solar aerodynamic coefficients and specifications are presented in appendices A and B.

$$\begin{pmatrix} f_x \\ f_y \\ f_z \end{pmatrix} = \begin{pmatrix} -mg\, s_\theta \\ mg\, c_\theta\, s_\phi \\ mg\, c_\theta\, c_\phi \end{pmatrix} + \frac{1}{2}\rho V_a^2 S \begin{pmatrix} C_D \\ C_Y \\ C_L \end{pmatrix} + \frac{1}{2}\rho S_{prop} C_{prop} \begin{pmatrix} (k_{motor}\delta_t) - V_a^2 \\ 0 \\ 0 \end{pmatrix} \tag{3.39}$$

$$\begin{pmatrix} l \\ m \\ n \end{pmatrix} = \frac{1}{2}\rho V_a^2 \begin{pmatrix} SbC_l \\ ScC_m \\ SbC_n \end{pmatrix} + \begin{pmatrix} -k_{T_p}\Omega_{prop}^2 \\ 0 \\ 0 \end{pmatrix} \tag{3.40}$$

Chapter 4

Proposed IMU Sensor Fault Detection and Diagnosis Approaches

This chapter presents the proposed IMU sensor fault detection and diagnosis approaches to be applied to the Elektra Solar aircraft as follows

1. **KF-ATLMS Fault Detection and Diagnosis Approach:** based on the decoupled lateral and longitudinal linear models of the aircraft in combination with the ATLMS technique. Due to its linear model structure and noisy IMU measurements, residual generation is based on the design of two Kalman filters covering both longitudinal and lateral aircraft measurements. The alarm flag activation sequence is used for fault diagnosis.

2. **EKF-based Fault Detection and Diagnosis Approach:** based on a well-defined nonlinear kinematic model of the aircraft in combination with an extended Kalman filter for residual generation of IMU measurements. The mean-squared error of these residuals are then evaluated by fixed-value threshold for fault detection. The alarm flag activation sequence is used for fault diagnosis.

3. **PCA-based Fault Detection and Diagnosis Approach:** a model-free approach based on principal component analysis. Contributions to squared prediction error (SPE) are used for fault diagnosis [39].

4.1 The Current Approach

Currently, the Elektra 2 Solar aircraft uses a simple limit checking approach for the detection of abnormal deviation regarding selected measurements (fig. 4.1). Once any of such measurements is above a predefined maximum value, an alarm flag is raised and the reconfiguration action takes place. Upper limits are defined by the experience of the aircraft team. As mentioned in chapter 1, this oversimplified detection approach can hide some faulty behaviors, making it difficult for early detection of small abrupt or incipient sensor faults. In case of fault occurrence, sensor reconfiguration action is defined as switching from primary IMU sensor to backup IMU sensor.

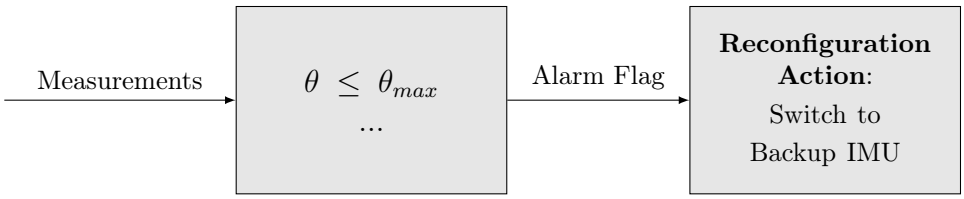

Figure 4.1: Current detection of abnormal deviation of IMU sensor measurements applied to Elektra 2 Solar aircraft.

4.2 The KF-ATLMS Fault Detection Approach

This approach considers the decoupled linear models of the aircraft in combination with the design of Kalman filters for residual generation. The logarithmic likelihood ratio (LLR) is then used as a decision function and an adaptive threshold based on the ATLMS algorithm is applied for fault detection as presented in figure 4.2. The details of the Kalman filter and ATLMS algorithms are presented in appendices D and E, respectively.

4.2.1 Linear Model Extraction of the Elektra 2 Solar Aircraft

In this section, system linearization is performed in order to provide linear, decoupled state-space models describing the longitudinal and lateral characteristics of the

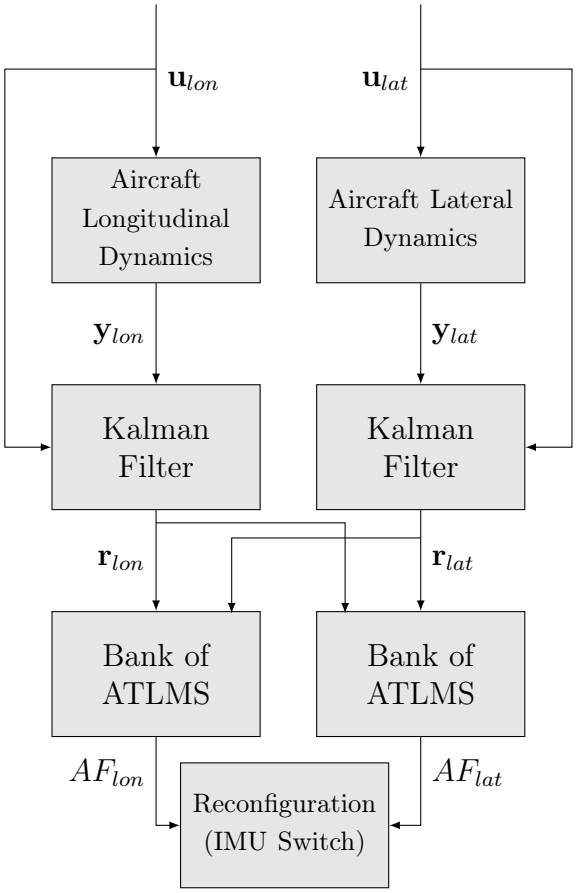

Figure 4.2: $\mathbf{u}_{lon}$ and $\mathbf{u}_{lat}$ are the control signals for the decoupled longitudinal and lateral aircraft dynamics, respectively. $\mathbf{y}_{lon}$ and $\mathbf{y}_{lat}$ are the aircraft measurements from longitudinal and lateral aircraft dynamics, respectively. $\mathbf{r}_{lon}$ and $\mathbf{r}_{lat}$ are the aircraft residuals from longitudinal and lateral aircraft dynamics, respectively. AF_{lon} and AF_{lat} refer to the longitudinal and lateral alarm flags, respectively.

Elektra 2 Solar aircraft that will be used for fault detection purposes.

Aircraft Trim Conditions and Linearization

Consider a nonlinear aircraft system described by

$$\dot{\mathbf{x}} = f(\mathbf{x}, \mathbf{u}) \tag{4.1}$$

where $\mathbf{x}$ is the state vector of the system, and $\mathbf{u}$ is the input vector. The aircraft is said to be in equilibrium (trimmed) at the state $\mathbf{x}^*$ and input $\mathbf{u}^*$ if

$$f(\mathbf{x}^*, \mathbf{u}^*) = 0 \tag{4.2}$$

Letting $\tilde{\mathbf{x}} \triangleq \mathbf{x} - \mathbf{x}^*$, it follows

$$\begin{aligned}
\dot{\tilde{\mathbf{x}}} &= \dot{\mathbf{x}} - \dot{\mathbf{x}}^* \\
&= f(\mathbf{x}, \mathbf{u}) - f(\mathbf{x}^*, \mathbf{u}^*) \\
&= f(\mathbf{x} + \mathbf{x}^* - \mathbf{x}^*, \mathbf{u} + \mathbf{u}^* - \mathbf{u}^*) - f(\mathbf{x}^*, \mathbf{u}^*) \\
&= f(\mathbf{x}^* + \tilde{\mathbf{x}}, \mathbf{u}^* + \tilde{\mathbf{u}}) - f(\mathbf{x}^*, \mathbf{u}^*)
\end{aligned} \tag{4.3}$$

Computing the Taylor series expansion of the first term about the trim state and neglecting the higher order terms (H.O.T) in equation (4.3), it follows

$$\begin{aligned}
\dot{\tilde{\mathbf{x}}} &= f(\mathbf{x}^*, \mathbf{u}^*) + \frac{\partial f(\mathbf{x}^*, \mathbf{u}^*)}{\partial \mathbf{x}} \tilde{\mathbf{x}} + \frac{\partial f(\mathbf{x}^*, \mathbf{u}^*)}{\partial \mathbf{u}} \tilde{\mathbf{u}} + H.O.T. - f(\mathbf{x}^*, \mathbf{u}^*) \\
&\approx \frac{\partial f(\mathbf{x}^*, \mathbf{u}^*)}{\partial \mathbf{x}} \tilde{\mathbf{x}} + \frac{\partial f(\mathbf{x}^*, \mathbf{u}^*)}{\partial \mathbf{u}} \tilde{\mathbf{u}}
\end{aligned} \tag{4.4}$$

Finally, the linearized dynamics are determined by computing the Jacobians $\left.\frac{\partial f}{\partial \mathbf{x}}\right|_{\mathbf{x}=\mathbf{x}^*}$ and $\left.\frac{\partial f}{\partial \mathbf{u}}\right|_{\mathbf{u}=\mathbf{u}^*}$, evaluated at the trim conditions. The resulting linear model is then approximately decoupled into longitudinal and lateral-directional systems as follows

$$\begin{bmatrix} \dot{\mathbf{x}}_{lon} \\ \dot{\mathbf{x}}_{lat} \end{bmatrix} = \begin{bmatrix} \mathbf{A}_{lon} & 0 \\ 0 & \mathbf{A}_{lat} \end{bmatrix} \begin{bmatrix} \mathbf{x}_{lon} \\ \mathbf{x}_{lat} \end{bmatrix} + \begin{bmatrix} \mathbf{B}_{lon} & 0 \\ 0 & \mathbf{B}_{lat} \end{bmatrix} \begin{bmatrix} \mathbf{u}_{lon} \\ \mathbf{u}_{lat} \end{bmatrix} \tag{4.5}$$

$$\begin{bmatrix} \mathbf{y}_{lon} \\ \mathbf{y}_{lat} \end{bmatrix} = \begin{bmatrix} \mathbf{C}_{lon} & 0 \\ 0 & \mathbf{C}_{lat} \end{bmatrix} \begin{bmatrix} \mathbf{x}_{lon} \\ \mathbf{x}_{lat} \end{bmatrix} \tag{4.6}$$

The longitudinal dynamics describes the aircraft motion in the $(x_b,\ z_b)$-plane in the body reference frame $\mathcal{F}^b$ and it has 3 degrees of freedom: aircraft pitch, longitudinal motion and vertical motion.

The state vector for longitudinal motion $\mathbf{x}_{lon}$ is given by

$$\mathbf{x}_{lon} \triangleq (u,\ w,\ q,\ \theta,\ h, \tau)^T \tag{4.7}$$

and the longitudinal input vector $\mathbf{u}_{lon}$ is defined as

$$\mathbf{u}_{lon} \triangleq (\delta_e,\, \delta_t)^T. \tag{4.8}$$

where u and w are the linear velocities along the x_b and z_b axes respectively, in body frame $\mathcal{F}^b$; q corresponds to the pitch rate; θ indicates the pitch angle; h indicates the altitude of the aircraft and τ denotes the angular velocity of the motor; δ_e and δ_t are the elevator and throttle commands, respectively.

The lateral dynamics describes the aircraft motion around the z_b-axis in body frame $\mathcal{F}^b$ and consists of roll, yaw and lateral motion. The state vector for lateral motion is given by

$$\mathbf{x}_{lat} \triangleq (v,\, p,\, r,\, \phi,\, \psi)^T \tag{4.9}$$

and the respective input vector is defined as

$$\mathbf{u}_{lat} \triangleq (\delta_a,\, \delta_r)^T. \tag{4.10}$$

where v is the linear velocity along the y_b axis, in body frame $\mathcal{F}^b$; p and r correspond to the roll and yaw rates, respectively; ϕ and ψ indicates the roll angle and yaw angle, respectively; δ_a and δ_r are the aileron and rudder commands, respectively.

The measured output vector for longitudinal dynamics $\mathbf{y}_{lon_m}$ and lateral dynamics $\mathbf{y}_{lat_m}$ are then rewritten in terms of the aircraft airspeed V_a, the angle of attack α, and the sideslip angle β as follows

$$\mathbf{y}_{lon_m} \triangleq (V_a,\, \alpha,\, q,\, \theta,\, h)^T \tag{4.11}$$

$$\mathbf{y}_{lat_m} \triangleq (\beta,\, p,\, r,\, \phi,\, \psi)^T. \tag{4.12}$$

All states and measurements are provided in the International System of Units

(SI) and are presented in table 4.1.

Table 4.1: Elektra Aircraft Measurements

Description	**Parameters**	**Unit**
Aircraft Airspeed	V_a	m/s
Body velocity	u, v, w	m/s
Aircraft Altitude	h	m
Angle of Attack and Sideslip angle	α, β	rad
Roll, pitch, and yaw angles	ϕ, θ, ψ	rad
Roll, pitch, and yaw rates	p, q, r	rad/s

The flowchart presented in figure 4.3 summarizes the procedures of aircraft trimming and linearization. For the Elektra 2 Solar aircraft model, a typical flight condition is defined in table 4.2

Table 4.2: Elektra 2 Solar Flight Condition

Description	**Parameters**	**Values**
Desired Aircraft Airspeed	V_a^*	18 m/s
Desired Aircraft Altitude	h^*	500 m

The resulting decoupled state-space model describing the longitudinal dynamics of the aircraft is presented in equations (4.13) and (4.14).

$$\begin{bmatrix} \dot{u} \\ \dot{w} \\ \dot{q} \\ \dot{\theta} \\ \dot{h} \\ \dot{\tau} \end{bmatrix} = \begin{bmatrix} -0.074 & 0.56 & -0.54 & -9.79 & 0 & 0.01 \\ -0.85 & -4.22 & 16.75 & -0.29 & 0.0009 & 0 \\ 0.02 & -0.55 & -3.83 & 0 & 0 & -0.0019 \\ 0 & 0 & 1 & 0 & 0 & 0 \\ 0.03 & -0.99 & 0 & 20 & 0 & 0 \\ 2.72 & 0.08 & 0 & 0 & 0.0026 & -0.99 \end{bmatrix} \begin{bmatrix} u \\ w \\ q \\ \theta \\ h \\ \tau \end{bmatrix} + \begin{bmatrix} 0.159 & 0 \\ -5.58 & 0 \\ -13.86 & 0 \\ 0 & 0 \\ 0 & 0 \\ 0 & 198.42 \end{bmatrix} \begin{bmatrix} \delta_e \\ \delta_t \end{bmatrix} \tag{4.13}$$

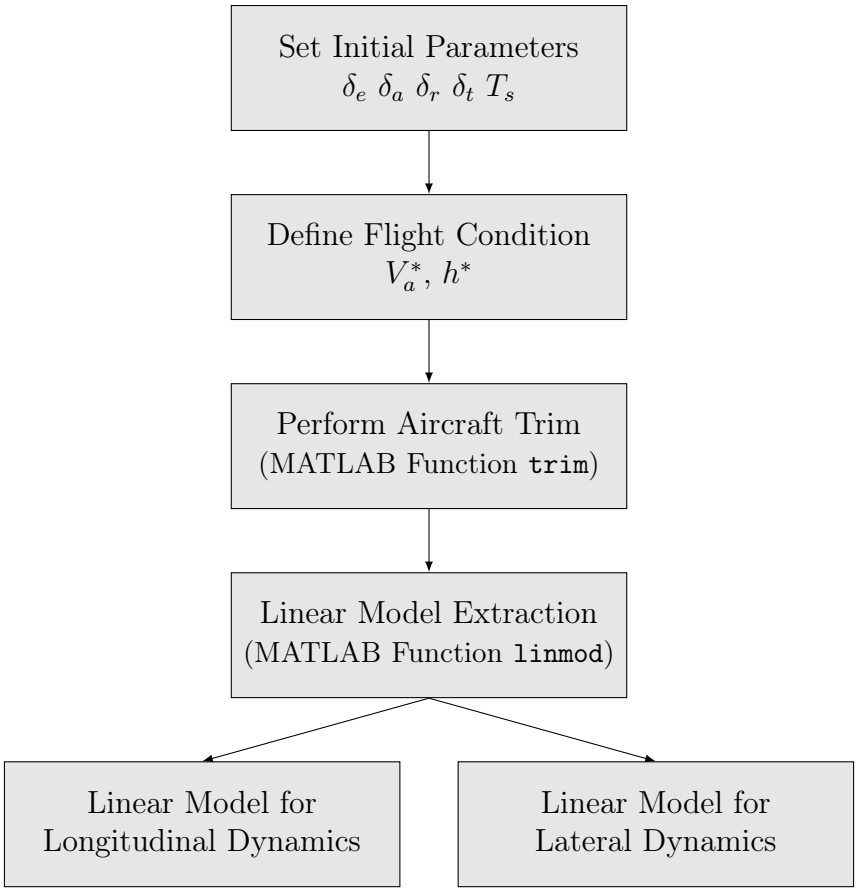

Figure 4.3: Aicraft Trim and Linearization Flowchart. δ_e, δ_t, δ_a and δ_r are the elevator, throttle, aileron and rudder commands, respectively. T_s is the sampling period; V_a^*, h^* corresponds to the airspeed and altitude in a typical flight configuration.

$$y_{m_{lon}} = \begin{bmatrix} 0.99 & 0.03 & 0 & 0 & 0 & 0 \\ -0.0015 & 0.05 & 0 & 0 & 0 & 0 \\ 0 & 0 & 1 & 0 & 0 & 0 \\ 0 & 0 & 0 & 1 & 0 & 0 \\ 0 & 0 & 0 & 0 & 1 & 0 \end{bmatrix} \begin{bmatrix} V_a \\ \alpha \\ q \\ \theta \\ h \end{bmatrix} \tag{4.14}$$

The resulting state-space model describing the lateral dynamics of the aircraft, is presented in equations (4.15) and (4.16).

$$\begin{bmatrix} \dot{v} \\ \dot{p} \\ \dot{r} \\ \dot{\phi} \\ \dot{\psi} \end{bmatrix} = \begin{bmatrix} -0.13 & 0.06 & -19.13 & 9.79 & 0 \\ -0.23 & -23.8 & 6.23 & 0 & 0 \\ 0.04 & -2.35 & -0.5 & 0 & 0 \\ 0 & 1 & 0.03 & 0 & 0 \\ 0 & 0 & 1 & 0 & 0 \end{bmatrix} \begin{bmatrix} v \\ p \\ r \\ \phi \\ \psi \end{bmatrix} + \begin{bmatrix} -0.53 & 1.40 \\ -15.68 & 0.18 \\ -0.41 & -0.95 \\ 0 & 0 \\ 0 & 0 \end{bmatrix} \begin{bmatrix} \delta_a \\ \delta_r \end{bmatrix} \quad (4.15)$$

$$y_{m_{lat}} = \begin{bmatrix} 0.05 & 0 & 0 & 0 & 0 \\ 0 & 1 & 0 & 0 & 0 \\ 0 & 0 & 1 & 0 & 0 \\ 0 & 0 & 0 & 1 & 0 \\ 0 & 0 & 0 & 0 & 1 \end{bmatrix} \begin{bmatrix} \beta \\ p \\ r \\ \phi \\ \psi \end{bmatrix} \quad (4.16)$$

4.2.2 Longitudinal and Lateral Kalman Filters for Residual Generation

As shown in figure 4.2, each linear model (longitudinal or lateral) has its own Kalman filter for residual generation.

Taking advantage of the decoupling nature of the aircraft linear system, residuals from longitudinal Kalman filter are sensitive to faults in longitudinal measurements but insensitive to faults in lateral dynamics (Definitions 4.1 and 4.2). Conversely, residuals from lateral dynamics Kalman filter are sensitive to faults in lateral measurements but insensitive to faults in longitudinal dynamics.

Once such decoupling feature is not always possible for other systems, sensitive and insensitive residuals can also be systematically designed by a decoupling matrix as in the structured residual technique presented in [4] or by a bank of observers/estimators as in [30], for example.

Definition 4.1 *The residual is said to be fault-sensitive if it is highly influenced by fault occurrence and consequently deviates significantly from zero.*

Definition 4.2 *The residual is said to be fault-insensitive if it is not influenced by fault occurrence or such influence is significantly lower in comparison with the sensitive residual.*

Table 4.10 summarizes the Kalman filter equations for the longitudinal linear model of the aircraft. A similar set of equations describes the Kalman filter equations for the lateral linear model of the aircraft.

The covariance matrices for longitudinal and lateral Kalman filters are defined in equation (4.17) according to table 4.3 and the details of the Kalman filter algorithm are presented in appendix D.

$$\begin{aligned}
\mathbf{R}_{lon} &= \text{diag}(\sigma_{V_a}^2\ \sigma_\alpha^2\ \sigma_q^2\ \sigma_\theta^2\ \sigma_h^2) \\
\mathbf{R}_{lat} &= \text{diag}(\sigma_\beta^2\ \sigma_p^2\ \sigma_r^2\ \sigma_\phi^2\ \sigma_\psi^2) \\
\mathbf{Q}_{lon} &= \text{diag}(\sigma_u^2\ \sigma_w^2\ \sigma_q^2\ \sigma_\theta^2\ \sigma_h^2) \\
\mathbf{Q}_{lat} &= \text{diag}(\sigma_v^2\ \sigma_p^2\ \sigma_r^2\ \sigma_\phi^2\ \sigma_\psi^2)
\end{aligned} \tag{4.17}$$

Table 4.3: Standard deviations of sensor noise

Standard Deviations	Magnitude	Units
σ_{a_x}, σ_{a_y}, σ_{a_z}	0.03	m/s^2
σ_p, σ_q, σ_r	$0.02\pi/180$	rad/s
σ_ϕ, σ_θ, σ_ψ	$0.02\pi/180$	rad
σ_α, σ_β	$0.1\pi/180$	rad
σ_u, σ_v, σ_w	0.02	m/s
σ_{V_a}	0.1	m/s
σ_h	0.1	m

Table 4.4: Longitudinal Kalman filter equations

Prediction	
	Predicted state estimate $\hat{\mathbf{x}}_{lon_{k\|k-1}} = \mathbf{A}_{lon_k}\hat{\mathbf{x}}_{lon_{k-1\|k-1}} + \mathbf{B}_{lon_k}\mathbf{u}_{lon_k}$
	Predicted covariance estimate $\mathbf{P}_{k\|k-1} = \mathbf{A}_{lon_k}\mathbf{P}_{k-1\|k-1}\mathbf{A}^T_{lon_k} + \mathbf{Q}_{lon_k}$
Update	
	Measurement residual $\mathbf{r}_{lonk} = \mathbf{y}_{mlon_k} - \mathbf{C}_{lon_k}\hat{\mathbf{x}}_{lon_{k\|k-1}}$
	Kalman gain $\mathbf{K}_k = \mathbf{P}_{k\|k-1}\mathbf{C}^T_{lon_k}(\mathbf{C}_{lon_k}\mathbf{P}_{k\|k-1}\mathbf{C}^T_{lon_k} + \mathbf{R}_{lon_k})^{-1}$
	Updated state estimate $\hat{\mathbf{x}}_{lon_{k\|k}} = \hat{\mathbf{x}}_{lon_{k\|k-1}} + \mathbf{K}_k(\underbrace{\mathbf{y}_{mlon_k} - \mathbf{C}_{lon_k}\hat{\mathbf{x}}_{lon_{k\|k-1}}}_{\text{residual generation}})$
	Updated covariance estimate $\mathbf{P}_{k\|k} = (\mathbf{I} - \mathbf{K}_k\mathbf{C}_{lon_k})\mathbf{P}_{k\|k-1}$

4.2.3 ATLMS: The Adaptive Threshold

The adaptive threshold (ATLMS) presented here is based on the technique exposed in [50] and its general scheme is shown in figure 4.4. The ATLMS technique allows the threshold to be tuned by changing well known parameters independently of the application and is based on SPRT algorithm [51] and the LMS (Least-Mean-Square) algorithm [52]. The requirements to the dynamic behavior of the adaptive threshold are

(i) low sensitivity to control signal variation;

(ii) low sensitivity to noise;

(iii) and high sensitivity to faulty residuals.

For each data sample k, the ATLMS algorithm computes the logarithmic likelihood ratio L_k in terms of the probability density function p_0 of the insensitive

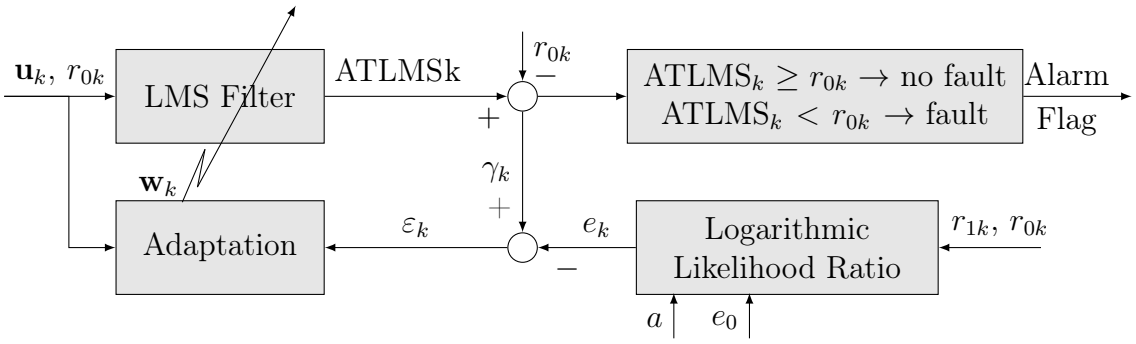

Figure 4.4: ATLMS Block diagram: $\mathbf{u}_k$ is the control signal vector, r_{0k} is the insensitive residual, r_{1k} is the sensitive residual, ε_k is the estimation error, $\mathbf{w}_k$ is the weight vector of the LMS algorithm. Both safety offset e_0 and sensitivity factor a are ATLMS tuning parameters. A fault alarm flag is raised if the adaptive threshold $\text{ATLMS}_k < r_{0k}$. The details of the ATLMS algorithm and its parameters are presented in Appendix E.

residual r_0 and the probability density function p_1 of the sensitive residual r_1 as follows

$$L_k = \ln \frac{p_1(r_{1k})}{p_0(r_{0k})} \tag{4.18}$$

Considering that r_0 and r_1 present normal distribution with zero mean and same variance σ_0^2, the ratio $\ln \dfrac{p_1}{p_0}$ can be simplified as follows

$$L_k = \frac{r_{0k}^2 - r_{1k}^2}{2\sigma_0^2} \tag{4.19}$$

An intrinsic characteristic of the sequential probability ratio test is that the expected value of the likelihood ratio ($E[L_k]$) presents trends in opposite directions under different hypotheses [50], (appendix E, eq. (E.22)). This particular feature provides the following ATLMS decisions for fault detection

(i) In favor of faulty mode (Hypothesis $\mathcal{H}_1$) if the adaptive threshold - which depends on L_k - crosses downwards the insensitive residual ($\text{ATLMS}_k < r_{0k}$) at instant k;

(ii) In favor of normal mode (Hypothesis $\mathcal{H}_0$), otherwise ($\text{ATLMS}_k \geq r_{0k}$);

Regarding implementation procedures, the SPRT algorithm (appendix E, section E.2) needs successive re-initializations for decision declaration. However, the basic

idea behind the proposed adaptive threshold is to use the adaptability of the LMS algorithm to reinitialize the ATLMS decision declaration automatically as presented in table 4.5 and figure 4.4. Appendix E presents the mathematical background of the ATLMS method and a brief discussion about its tuning parameters.

Table 4.5: ATLMS Algorithm for Fault Detection

	ATLMS Algorithm for Fault Detection
Step 1:	Ad-hoc definition of ATLMS tuning parameters: safety offset e_0, convergence rate μ, sensitivity factor a, and sampling time T_s
Step 2:	Define input vector $\phi^T = [\underbrace{\delta_a\ \delta_e\ \delta_r\ \delta_t}_{\mathbf{u}}\ r_0\ 1]$ composed of control signal vector $\mathbf{u}$ and insensitive residual r_0 (see definition 4.2)
Step 3:	Initial conditions for the weight vector arbitrarily set to $\mathbf{w}_0 = \mathbf{0}$
Step 4:	For $k = 0$, $\text{ATLMS}_k = \phi_k^T \mathbf{w}_k$
	For $k = 0$, $\gamma_k = ATLMS_k - r_{0k}$
	For $k = 0$, $e_k = e_0 - a\dfrac{r_{0k}^2 - r_{1k}^2}{2T_s\sigma_0^2}$,
	For $k = 0$, $\varepsilon_k = \gamma_k - e_k$
	Update weight vector $\mathbf{w}_{k+1} = \mathbf{w}_k - 2\mu\varepsilon_k\phi_k$
Step 5:	For $k = 1$:N $\text{ATLMS}_k = \phi_k^T \mathbf{w}_k$ (eq. (E.32)) If $\text{ATLMS}_k < r_{0k}$ then Alarm Flag = 1 Otherwise Alarm Flag = 0 (eq. (E.24)) $\varepsilon_k = \gamma_k - e_k$, where ε_k is the estimation error (eq. (E.27)) $\mathbf{w}_{k+1} = \mathbf{w}_k - 2\mu\varepsilon_k\phi_k$ (eq. (E.32)) end

4.2.4 Bank of ATLMS Filters

In order to provide useful information for fault isolation and fault identification, the bank of ATLMS filters regarding longitudinal dynamics is designed to be sensitive to faults in longitudinal measurements but insensitive to faults in lateral dynamics. Conversely, the bank of ATLMS filters regarding lateral dynamics is designed to be sensitive to faults in lateral measurements but insensitive to faults in longitudinal dynamics. Figures 4.5 and 4.6 illustrate the scheme of the bank of ATLMS filters for longitudinal and lateral dynamics according to table 4.6.

Table 4.6: Bank of ATLMS filters design: sensitive and insensitive residuals

	Longitudinal Residuals ($\mathbf{r}_{lon}$)	Lateral Residuals ($\mathbf{r}_{lat}$)
Sensitive Residuals	r_{V_a}, r_α, r_q, r_θ, r_h	r_β, r_p, r_r, r_ϕ, r_ψ
Insensitive Residual	r_ψ	r_θ

For the longitudinal measurements, the bank of ATLMS filters uses the yaw angle ψ residual as the insensitive residual. For the lateral measurements, the bank of ATLMS uses the pitch angle θ residual as the insensitive residual. Due to the critical aspect of IMU faults, the fault detection flag is activated - and kept active - if any of the adaptive thresholds indicates a fault. The same reconfiguration guidelines are applied to the other two fault detection approaches. The label AF_i refers to the alarm flag of measurement i. The combination of fault flags for longitudinal and lateral dynamics are denoted as AF_{Lon} and AF_{Lat}.

Tables 4.7 and 4.8 show the tuning of ATLMS parameters for longitudinal and lateral aircraft dynamics, respectively.

4.2.5 KF-ATLMS Fault Diagnosis Approach

A decision table based on the Alarm Flag Activation Sequence (AFAS) is then used as a tool for fault identification and isolation. The AFAS metrics proposed here indicates which alarm flags have been activated and the sequence of their activation. As a consequence, different faults produce different flag activation sequences. For the sake of terminology simplification, table 5.5 presents the alarm flag labels used

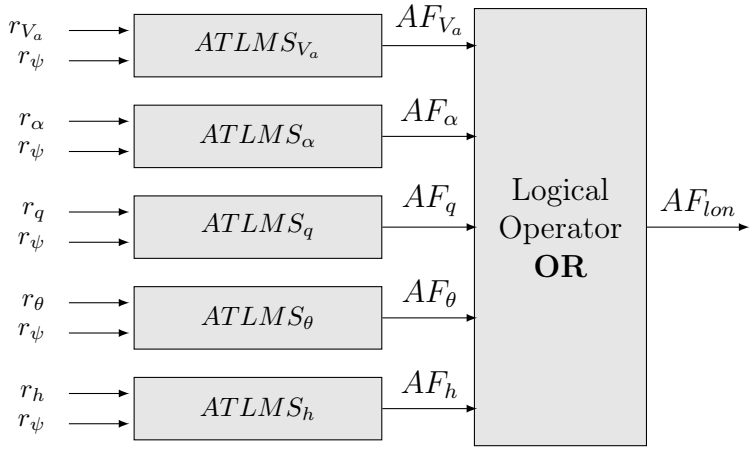

Figure 4.5: Bank of ATLMS filters for Longitudinal Dynamics. r_i is the residual of measurement i. V_a is the aircraft airspeed, α is the angle of attack, q is the pitch rate, θ is the pitch angle, and h is the aircraft altitude. The bank of ATLMS uses the yaw angle ψ residual as the insensitive residual. The label AF_i refers to the alarm flag of measurement i and AF_{lon} is the combined alarm flag for longitudinal dynamics used for sensor switching reconfiguration in case of fault occurrence.

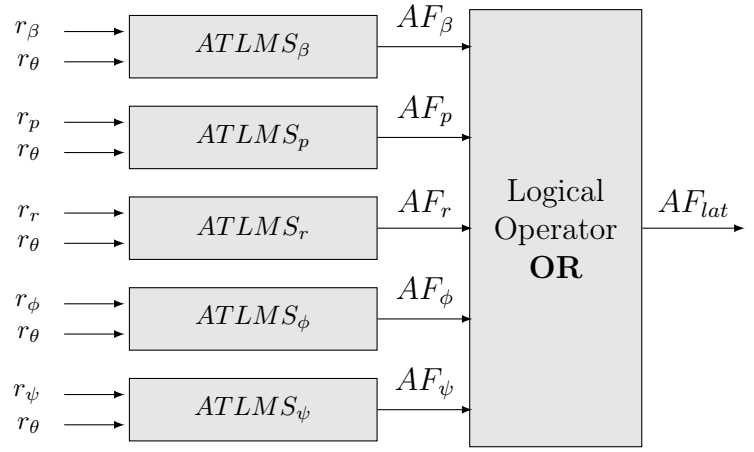

Figure 4.6: Bank of ATLMS Filters for Lateral Dynamics. R_i is the residual of measurement i. β is the sideslip angle, p is the roll rate, r is the yaw rate, ϕ is the roll angle and ψ is the yaw angle. The bank of ATLMS uses the pitch angle θ residual as the insensitive residual. The label AF_i refers to the alarm flag of measurement i and AF_{lat} is the combined alarm flag for lateral dynamics used for sensor switching reconfiguration in case of fault occurrence.

in this approach. Therefore, an alarm flag of AF_0 indicates no fault, AF_A indicates that the alarm flag associated with the angle of attack α was activated, and AF_{FT} indicates that the alarm flag associated with roll angle ϕ, AF_F, was first activated, followed by the activation of the alarm flag associated with pitch angle θ, AF_T. The

Table 4.7: ATLMS parameter tuning for longitudinal dynamics. r_1 = sensitive residual; r_0 = insensitive residual; e_0 = safety offset; a = sensitivity factor; μ = convergence rate. V_a = airspeed; α = angle of attack; q = pitch rate; θ = pitch angle; h = aircraft altitude

ATLMS	r_1	r_0	e_0	a	μ
ATLMS_{V_a}	V_a	ψ	12	-0.2	0.005
ATLMS_{α}	α	ψ	15	-0.2	0.005
ATLMS_{q}	q	ψ	1	-0.5	0.005
ATLMS_{θ}	θ	ψ	7	-0.2	0.005
ATLMS_{h}	h	ψ	35	-0.2	0.005

Table 4.8: ATLMS parameter tuning for lateral dynamics. r_1 = sensitive residual; r_0 = insensitive residual; e_0 = safety offset; a = sensitivity factor; μ = convergence rate; β = sideslip angle; p = roll rate; r = yaw rate; ϕ = roll angle; ψ yaw angle.

ATLMS	r_1	r_0	e_0	a	μ
ATLMS_{β}	β	θ	2.2	-0.3	0.005
ATLMS_{p}	p	θ	1	-0.2	0.005
ATLMS_{r}	r	θ	1	-0.5	0.005
ATLMS_{ϕ}	ϕ	θ	1	-0.2	0.005
ATLMS_{ψ}	ψ	θ	0.01	-1.5	0.005

patterns formed by the different sequences of fault alarms provide useful information regarding the identification and isolation of proposed faults.

Table 4.9: Alarm Flag (AF) Captions: AF_i indicates that the alarm flag associated with the measurement i was activated. V_a is the aircraft airspeed, α and β are the angle of attack and sideslip angle, respectively; p, q, and r are the aircraft angular rates; ϕ, θ, ψ are the aircraft attitude angles; and h is the aircraft altitude.

Measurement	V_a	α	β	p	q	r	ϕ	θ	ψ	h	No Fault
Alarm Flag	AF_V	AF_A	AF_B	AF_P	AF_Q	AF_R	AF_F	AF_T	AF_S	AF_H	AF_0

4.3 EKF-based Fault Detection Approach

The EKF-based approach as described in figure 4.9 considers a simplified model of the aircraft kinematics (fig.4.7) in combination of an extended Kalman filter for residual generation. Although the advantages of kinematic-based approaches are not fully exploited in aircraft fault detection strategies [53], kinematic relations are exactly known. Consequently, no model mismatches or unmodelled dynamics need to be taken into account, which provides a considerable advantage over classical linear model-based fault detection strategies.

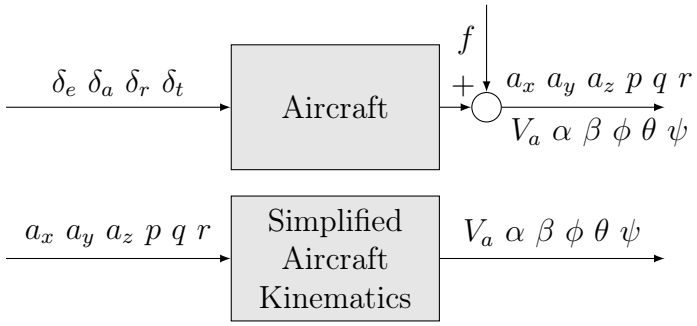

Figure 4.7: Scheme of the aircraft process (top) and its simplified aircraft kinematic model (bottom). f is an additive sensor fault. δ_e, δ_a, δ_r, and δ_t are the elevator, aileron, rudder and throttle commands, respectively. a_x, a_y, a_z are the aircraft accelerations; p, q, and r are the aircraft angular rates; ϕ, θ, and ψ are the aircraft attitude angles; and V_a, α, β are the aircraft airspeed, angle of attack and sideslip angle, respectively.

4.3.1 The Aircraft Simplified Kinematic Model

The discrete-time nonlinear representation of the aircraft simplified kinematic model can be described as

$$\begin{aligned} \mathbf{x}_{k+1} &= f(\mathbf{x}_k, \mathbf{u}_k) + \mathbf{w}_k \\ \mathbf{y}_k &= h(\mathbf{x}_k) + \mathbf{v}_k \end{aligned} \tag{4.20}$$

where $\mathbf{x}_k$ represents the kinematic states

$$\mathbf{x}_k = \begin{bmatrix} u & v & w & \phi & \theta & \psi \end{bmatrix}^T \tag{4.21}$$

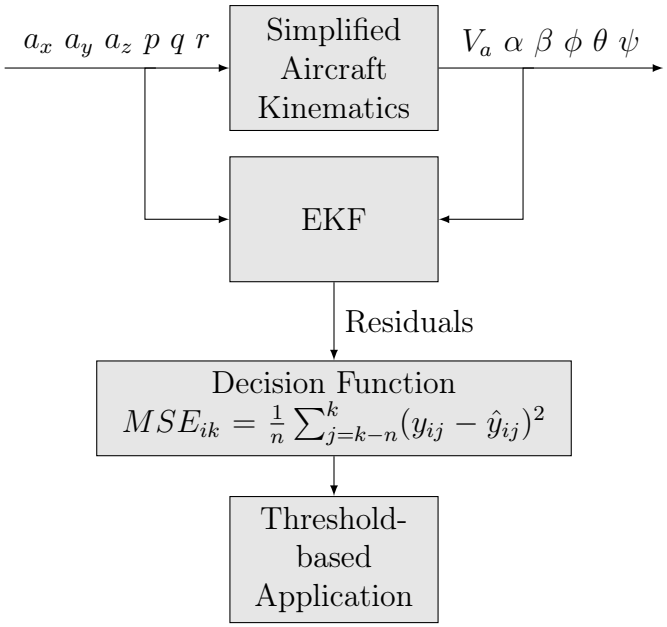

Figure 4.8: Scheme of the fault detection approach with a simplified aircraft kinematic model. It considers the design of an extended Kalman filter for residual generation. The decision function is based on the mean squared error (MSE) of the measurement residuals $(y_{ij} - \hat{y}_{ij})$ with $i = (V_a,\ \alpha,\ \beta,\ \phi,\ \theta,\ \psi)$ (table 4.10) at instant k and window size of n samples

and $\mathbf{u}_k$ is the kinematic input in terms of aircraft accelerations $(a_x,\ a_y,\ a_z)$ and aircraft angular rates $(p,\ q,\ r)$.

$$\mathbf{u}_k = \begin{bmatrix} a_x & a_y & a_z & p & q & r \end{bmatrix}^T \tag{4.22}$$

Once body speed components $(u,\ v,\ w)$ were not available from real flight data set, the kinematic output $\mathbf{y}_k$ was rewritten in terms of the airspeed V_a, angle of attack α, sideslip angle β, and attitude angles $(\phi,\ \theta,\ \psi)$ (eq. (3.22)) resulting in

$$\mathbf{y}_k = \begin{bmatrix} V_a & \alpha & \beta & \phi & \theta & \psi \end{bmatrix}^T \tag{4.23}$$

Variables in $\mathbf{u}_k$ and $\mathbf{y}_k$ are commonly available in any modern flight control system and are here represented as measured variables. Finally, $\mathbf{v}_k$ and $\mathbf{w}_k$ represent white Gaussian noise sequences.

If the kinematic state vector $\mathbf{x}_k$ is also rewritten in terms of the airspeed V_a, angle of attack α, sideslip angle β as in equation (3.22), the nonlinear state transition

function $f(\mathbf{x}_k, \mathbf{u}_k)$ is defined as follows

$$
\begin{aligned}
\dot{V}_a &= g(-s_\theta c_\alpha c_\beta + s_\phi c_\theta s_\beta + c_\phi c_\theta s_\alpha c_\beta) + a_x c_\alpha c_\beta + a_y s_\beta + a_z s_\alpha c_\beta \\
\dot{\alpha} &= \frac{g}{V_a c_\beta} + (c_\phi c_\theta c_\alpha + s_\theta s_\alpha) + \frac{1}{V_a c_\beta}(a_z c_\alpha - a_x s_\alpha) + q - t_\beta(p c_\alpha + r s_\alpha) \\
\dot{\beta} &= \frac{g}{V_a}(s_\theta c_\alpha s_\beta + s_\phi c_\theta c_\beta - c_\phi c_\theta s_\alpha s_\beta) + \frac{1}{V_a}(-a_x c_\alpha s_\beta + a_y c_\beta - a_z s_\alpha s_\beta) + p s_\alpha - r c_\alpha \\
\dot{\phi} &= p + s_\phi t_\theta q + c_\phi t_\theta r \\
\dot{\theta} &= c_\phi q - s_\phi r \\
\dot{\psi} &= \frac{s_\phi}{c_\theta} q + \frac{c_\phi}{c_\theta} r
\end{aligned}
\tag{4.24}
$$

where g is the gravity term, and $c_x \triangleq cos\, x$, $s_x \triangleq sin\, x$, and $t_x \triangleq tan\, x$.

4.3.2 The Extended Kalman Filter for Residual Generation

Due to the nonlinear nature of the kinematic model and noisy IMU measurements, an extended Kalman filter was designed for residual generation and the mean squared error (MSE) of the residuals is used as a decision function. The extended Kalman filter (EKF) algorithm is composed of two main phases, prediction and update. The general scheme of the discrete-time extended Kalman filter is presented in figure 4.9 and its equations are defined in table 4.10. The details of the extended Kalman filter algorithm is presented in appendix D.

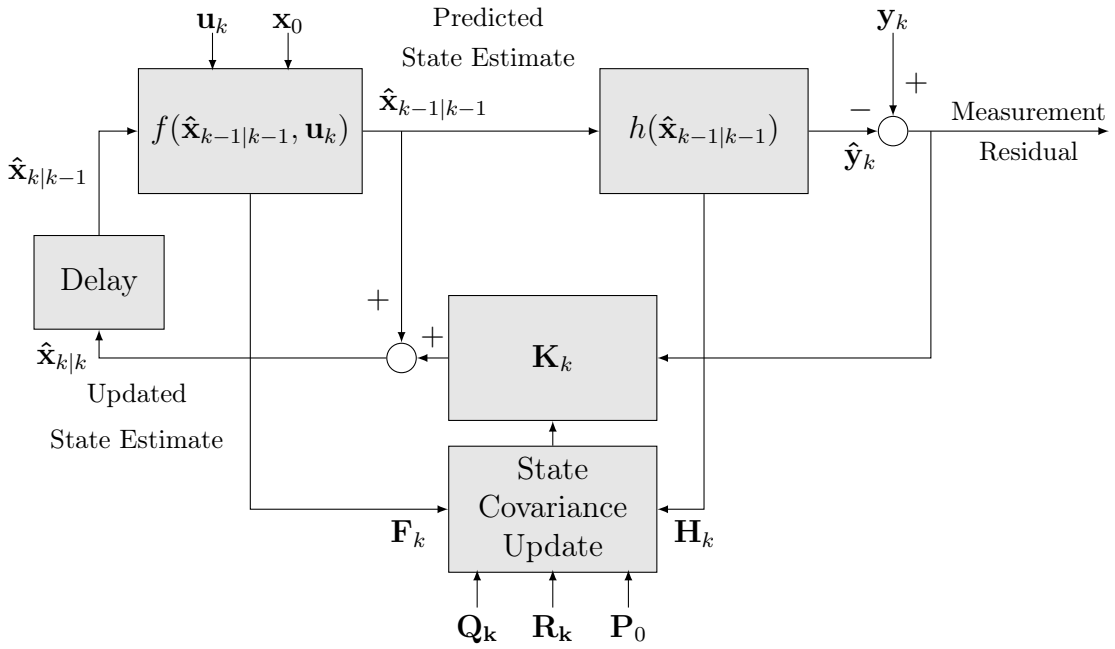

Figure 4.9: A general scheme of the extended Kalman filter applied to the aircraft kinematic model for residual generation.

Table 4.10: Extended Kalman filter equations

Prediction	
	Predicted state estimate
	$\hat{\mathbf{x}}_{k\|k-1} = f(\hat{\mathbf{x}}_{k-1\|k-1}, \mathbf{u}_k)$
	Predicted covariance estimate
	$\mathbf{P}_{k\|k-1} = \mathbf{F}_k \mathbf{P}_{k-1\|k-1} \mathbf{F}_k^T + \mathbf{Q}_k$
Update	
	Measurement residual
	$\tilde{\mathbf{y}}_k = \mathbf{y}_k - h(\hat{\mathbf{x}}_{k\|k-1})$
	Kalman gain
	$\mathrm{K}_k = \mathbf{P}_{k\|k-1} \mathbf{H}_k^T (\mathbf{H}_k \mathbf{P}_{k\|k-1} \mathbf{H}_k^T + \mathbf{R}_k)^{-1}$
	Updated state estimate
	$\hat{\mathbf{x}}_{k\|k} = \hat{\mathbf{x}}_{k-1\|k-1} + \mathbf{K}_k \tilde{\mathbf{y}}_k$
	Updated covariance estimate
	$\mathbf{P}_{k\|k} = (\mathbf{I} - \mathbf{K}_k \mathbf{H}_k) \mathbf{P}_{k\|k-1}$

The covariance matrix of the input measurement noise $\mathbf{R}_k = \text{diag}(\sigma_{a_x}^2\ \sigma_{a_y}^2\ \sigma_{a_z}^2\ \sigma_p^2\ \sigma_q^2\ \sigma_r^2)$ and the covariance matrix of the output measurement noise $\mathbf{Q}_k = \text{diag}(\sigma_{V_a}^2\ \sigma_\alpha^2\ \sigma_\beta^2\ \sigma_\phi^2\ \sigma_\theta^2\ \sigma_\psi^2)$ are defined according to table 4.3 and $\mathbf{F}_k = \left.\frac{\partial f}{\partial \mathbf{x}}\right|_{\hat{\mathbf{x}}_{k-1|k-1},\,\mathbf{u}_k}$ and $\mathbf{H}_k = \left.\frac{\partial h}{\partial \mathbf{x}}\right|_{\hat{\mathbf{x}}_{k-1|k-1}}$ are the Jacobians of the state transition model and observation model, respectively.

It is important to note that the transformation of the kinematic output vector $\mathbf{y}_k$ in terms of the airspeed V_a, angle of attack α, and sideslip angle β (eqs. (4.23) and (4.24)) provided a considerable simplification of the Jacobian of the observation model $\mathbf{H}_k$, resulting in $\mathbf{H}_k = \mathbf{I}_{6\times 6}$.

4.3.3 The Mean Squared Error as a Decision Function

The EKF-based fault detection approach uses the mean squared error (MSE) as a decision function [37]. The MSE metrics is defined in terms of the EKF residual $\tilde{y}_{ik}$ of measurement $i = (V_a,\ \alpha,\ \beta,\ \phi,\ \theta,\ \psi)$ (table 4.10) at instant k and window size of n samples as

$$\begin{aligned} MSE_{ik} &= \frac{1}{n}\sum_{j=k-n}^{k}(\tilde{y}_{ij})^2 \\ &= \frac{1}{n}\sum_{j=k-n}^{k}(y_{ij}-\hat{y}_{ij})^2 \end{aligned} \tag{4.25}$$

A fault alarm is activate if the MSE of any measurement residual exceeds the set of predefined threshold values presented in table 4.11. Each threshold value was chosen with an arbitrarily 10% safety offset from the respective maximum MSE value in fault-free scenario. For this approach, a 10-sample window size was selected.

4.3.4 EKF-based Fault Diagnosis Approach

Similarly to the previous fault diagnosis approach, the Alarm Flag Activation Sequence (AFAS) is also used as a tool for fault identification and isolation. The AFAS metrics indicates which alarm flags have been activated and the sequence of their activation. As a consequence, different faults produce different flag activation

Table 4.11: Threshold values with a 10% safety offset from the maximum residual MSE value of a fault-free simulation. MSE_{r_i} is the MSE of the residual of measurement i, where $i = V_a$ airspeed, α = angle of attack, β = sideslip angle, ϕ = roll angle, θ = pitch angle, ψ = yaw angle.

Residual MSE	**Maximum Residual MSE**	**Threshold Value**
$\text{MSE}r_{Va}$	0.01	0.011
$\text{MSE}r_{\alpha}$	0.0019	0.0021
$\text{MSE}r_{\beta}$	0.0019	0.0021
$\text{MSE}r_{\phi}$	1.2×10^{-5}	1.33×10^{-5}
$\text{MSE}r_{\theta}$	1.14×10^{-5}	1.25×10^{-5}
$\text{MSE}r_{\psi}$	1.2×10^{-5}	1.32×10^{-5}

sequences. Details of the AFAS metrics were previously presented in section 4.2.5.

4.4 PCA-based Fault Detection Approach

The third approach is based on principal component analysis (PCA). As presented in [4], the basic idea of PCA is to reduce the dimensionality of a data set of interrelated variables, while retaining as much as possible of the information present in the original data set. As a result, the original data set can be described by a transformed data set containing the so-called principal components. Appendix F presents more details about the PCA algorithm and its mathematical background.

4.4.1 The PCA Algorithm for Residual Generation

In this approach, residual generation can be achieved by comparing the original data set containing selected measurements of the aircraft with the back-transformed aircraft data set containing the principal components as illustrated in figure 4.10 and summarized in table 4.12.

After the generation of residuals as described in table 4.12, the decision function used in this approach is the squared prediction error (SPE), also known as Q statistics [54]. The SPE describes how well the reduced dimensional representation containing the principal components describes the original data. The SPE is defined

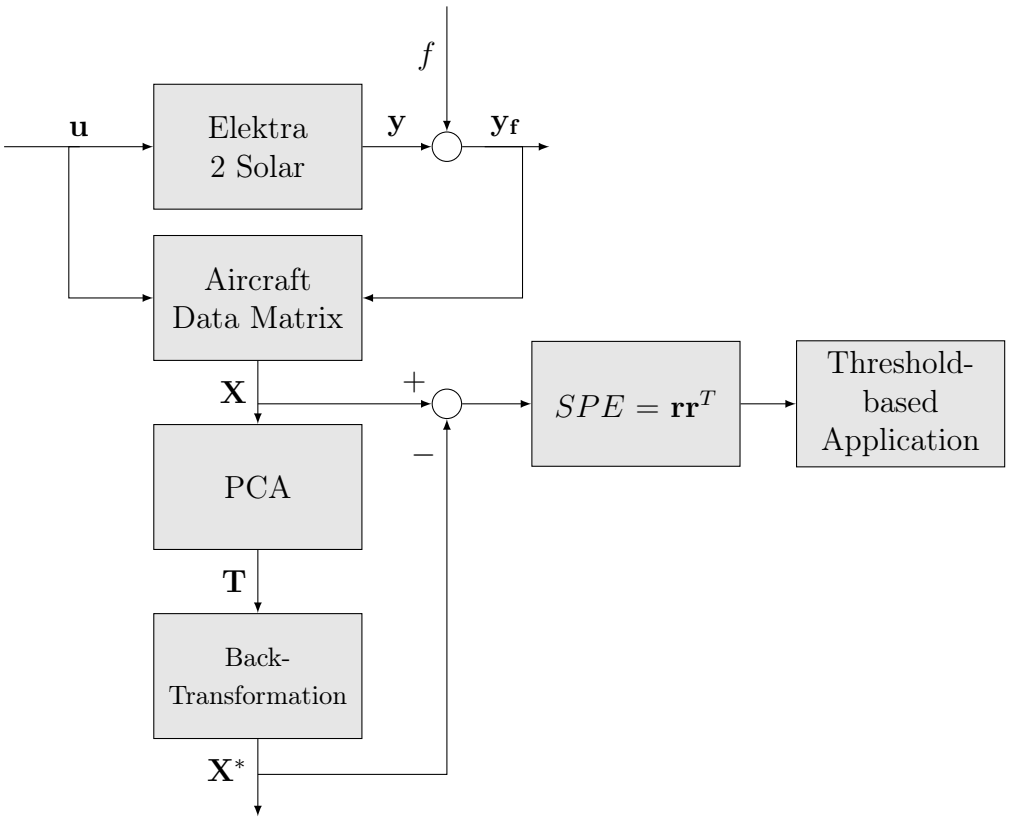

Figure 4.10: General scheme of the PCA method for fault detection. For practical purposes, a learning phase is required, in which fault-free data have first to be stored. Then the reduced data set is calculated and residuals are generated. Finally, the squared prediction error is used as a decision function and a suitable threshold-based application is applied. $\mathbf{u}$ indicates the process input vector; $\mathbf{y}$ is the process output vector; $\mathbf{f}$ is the vector of additive sensor faults; $\mathbf{y}_f$ is the faulty process output; $\mathbf{X}$ data matrix containing measured signals; $\mathbf{T}$ reduced data matrix containing principal components; and $\mathbf{X}^*$ back-transformed data matrix.

as

$$SPE_k = \mathbf{r}_k \mathbf{r}_k^T \tag{4.26}$$

where $\mathbf{r}_k$ is the residual vector at instant k (table 4.12, step 9). A fault alarm flag is activate if the SPE_k exceeds a predefined threshold value (table 4.14) at a given instant k.

Table 4.12: PCA Algorithm for Residual Generation

PCA Algorithm for Residual Generation	
Step 1:	Define aircraft data matrix $\mathbf{X}_{[m\times 12]} = [a_x\ a_y\ a_z\ p\ q\ r\ V_a\ \alpha\ \beta\ \phi\ \theta\ \psi]$ composed of 12 aircraft measurements: accelerations (a_x, a_y, a_z), angular rates (p, q, r), attitude angles (ϕ, θ, ψ), and airspeed, angle of attack and sideslip angle (V_a, α, β)
Step 2:	Compute mean-centered data matrix $\mathbf{X}_{[m\times 12]}$ in which each variable is scaled to have zero mean)
Step 3:	Calculation of covariance matrix $\mathbf{A}_{[12\times 12]} = \dfrac{\mathbf{X}^T\mathbf{X}}{m-1}$
Step 4:	Calculation of the eigenvalues λ_n of matrix $\mathbf{A}$ and respective eigenvectors $\mathbf{p}_n$ with $n = 1, \ldots, 12$
Step 5:	Selection of the most significant eigenvalues λ_r and corresponding unit eigenvectors $\mathbf{p}_r$ with $r = 1, \ldots, 6$ (see table 4.13).
Step 6:	Determination of the transformation matrix $\mathbf{P}_{[12\times 6]} = [\mathbf{p}_1, \mathbf{p}_2, \ldots, \mathbf{p}_6]$
Step 7:	Calculation of the new data matrix $\mathbf{T}_{[m\times 6]} = \mathbf{XP} = [\mathbf{t}_1, \mathbf{t}_2, \ldots, \mathbf{t}_6]$ with $\mathbf{t}_r = \mathbf{X}\mathbf{p}_r$. Matrix $\mathbf{T}$ contains original data described by a reduced number $r_{max} < n_{max}$ of variables, the principal components.
Step 8:	Back-transformation to the original data coordination system leads to $\mathbf{X}^*_{[m\times 12]} = \mathbf{T}_{[m\times 6]}\mathbf{P}^T_{[6\times 12]} = \mathbf{X}_{[m\times 12]}\mathbf{P}_{[12\times 6]}\mathbf{P}^T_{[6\times 12]}$
Step 9:	Online residual generation $\mathbf{r}_{k_{[1\times 12]}} = \mathbf{x}_{k_{[1\times 12]}} - \mathbf{x}^*_{k_{[1\times 12]}}$ as described in [4] where $\mathbf{r}_k$ is the residual vector at instant k

4.4.2 PCA Learning Phase

For practical purposes, the PCA algorithm requires a learning phase, in which fault-free data have first to be stored. Attention should be drawn to monitoring processes that runs in different operating conditions such as the Elektra 2 Solar aircraft. Using conventional PCA in this type of process can produce an excessive number of false alarms. Also, measured disturbances can be detected as faults. In order to deal with this open problem, possible solutions are based on one of the following main ideas

(i) Develop a conventional PCA model to account for all such changes;

(ii) Update the model to reflect the changes in the operation modes;

(iii) Build a PCA model for each operation mode;

The third option was used in this work during simulated flight scenarios with changes in flight conditions as presented in chapter 5.

4.4.3 Selection of Principal Components

Another critical step regarding the implementation of the PCA algorithm is the selection of the number of principal components to be analyzed. Although methods are available for testing component significance (e.g. parallel analysis, [55]), the general practice is problem-specific. An incorrect choice of the number of principal components may lead to the underextraction of components (i.e. loss of information), but it usually results in overextraction (i.e. inclusion of spurious components) [55].

As mentioned in the beginning of this chapter, the PCA algorithm aims to reduce data dimensionality by using fewer variables to represent the original set. The more dependent such variables are, the fewer principal components can be used for such representation. When the relationships between the original variables are nonlinear, more principal components will be necessary to describe the original data set.

Table 4.13 provides the eigenvalues of aircraft data matrix $\mathbf{A}_{[12\times12]}$ (table 4.12, step 3) and figure 4.11 shows the data variance retained by those eigenvalues. The sum of the eigenvalues of matrix $\mathbf{A}_{[12\times12]}$ corresponds to the sum of variances of each variable of the data matrix $\mathbf{X}_{[m\times12]}$, [6]. The eigenvalue λ_1, for example, captures 67% of aircraft data variance while λ_1 and λ_2 captures almost 98%. Using the parallel analysis method ([56]), the number of principal components would be 2. However, in order to decrease the SPE residual, six principal components were chosen ($\lambda_1 - \lambda_6$). Figure 4.12 illustrates the effect of choosing different number of principal components on residual generation and respective thresholds with an

arbitrarily 10% safety offset from the maximum SPE value in fault-free scenario. Threshold values for different number of principal components are given in table 4.14.

Table 4.13: Eigenvalues of $\mathbf{A}_{[12\times12]}$ (table 4.12, step 3) and percentage of the data variance explained by each principal component. The sum of the eigenvalues of matrix $\mathbf{A}_{[12\times12]}$ corresponds to the sum of variances of each variable of the data matrix $\mathbf{X}_{[m\times12]}$ [6].

Eigenvalues of $\mathbf{A}_{[12\times12]}$	$\frac{\lambda_i}{\sum_{i=1}^{12}\lambda_i} \times 100$ (%)
$\lambda_1 = 0.312$	66.86 %
$\lambda_2 = 0.137$	29.38 %
$\lambda_3 = 0.0171$	3.66 %
$\lambda_4 = 2.4 \times 10^{-4}$	0.05 %
$\lambda_5 = 1.0 \times 10^{-4}$	0.02 %
$\lambda_6 = 4.2 \times 10^{-6}$	0.0009 %
$\lambda_7 = 4.1 \times 10^{-6}$	0.0009 %
$\lambda_8 = 4.1 \times 10^{-6}$	0.0009 %
$\lambda_9 = 4.0 \times 10^{-6}$	0.0009 %
$\lambda_{10} = 3.9 \times 10^{-6}$	0.0009 %
$\lambda_{11} = 3.9 \times 10^{-6}$	0.0008 %
$\lambda_{12} = 3.8 \times 10^{-6}$	0.0008 %

Table 4.14: Threshold values for different numbers of principal components

Number of Principal Components	**Maximum SPE**	**Threshold Value**
2	0.93	1.02
4	0.023	0.026
6	1.11×10^{-4}	1.22×10^{-4}

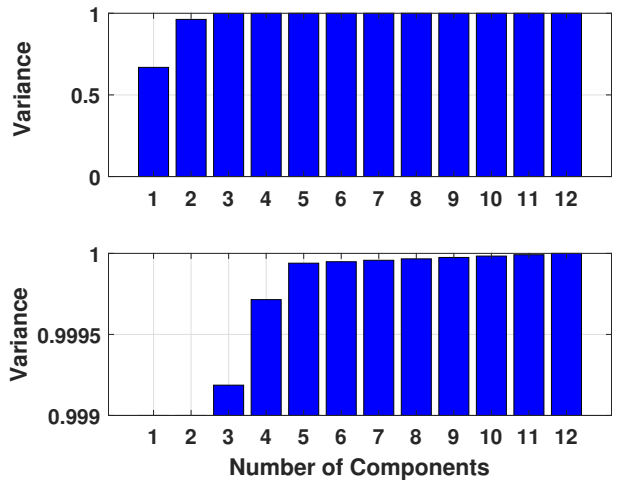

Figure 4.11: Data variance explained by eigenvalues (top) and zoomed plot (bottom).

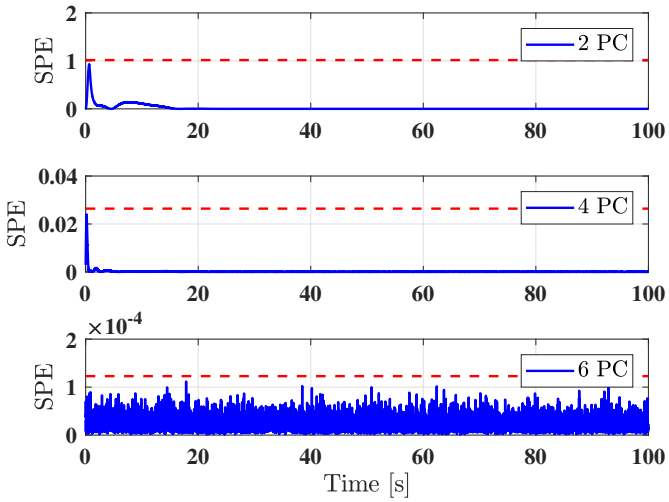

Figure 4.12: Squared prediction error (SPE) for 2, 4, and 6 principal components (PC) and their respective threshold values ($T_{2PC} = 1.02$, $T_{4PC} = 0.026$, and $T_{6PC} = 1.22 \times 10^{-4}$). The higher the number of principal components, the smaller the SPE. In order to decrease the SPE residual, six principal components were chosen ($\lambda_1 - \lambda_6$).

4.4.4 PCA-based Fault Diagnosis Approach

The contribution of each measurement residual to the squared prediction error (SPE) is then used as a tool for fault identification and isolation [54]. The contribution C_i is based on the sum of m residual samples (eq. (4.28)) for each of the $i = a_x$, a_y, a_z, p, q, r, V_a, α, β, ϕ, θ, ψ monitored variables normalized by their respective variances as follows

$$C_i = \frac{g_i}{\sqrt{\text{var}(g_i)}} \tag{4.27}$$

where g_i is the i-th element of the measurement row vector $\mathbf{g}_{[1\times 12]}$

$$\mathbf{g} = \sum_{k=1}^{m} \mathbf{r}_k \tag{4.28}$$

The higher the C_i, the more the variable i contributes to the squared prediction error. Therefore, a significantly higher C_i indicates that measurement i presents faulty behavior as illustrated in figure 4.13 (bottom). Conversely, in a fault-free scenario (fig. 4.13, top), measurement contributions to SPE present similar magnitude. Diagnosis results are presented in section 5.3.

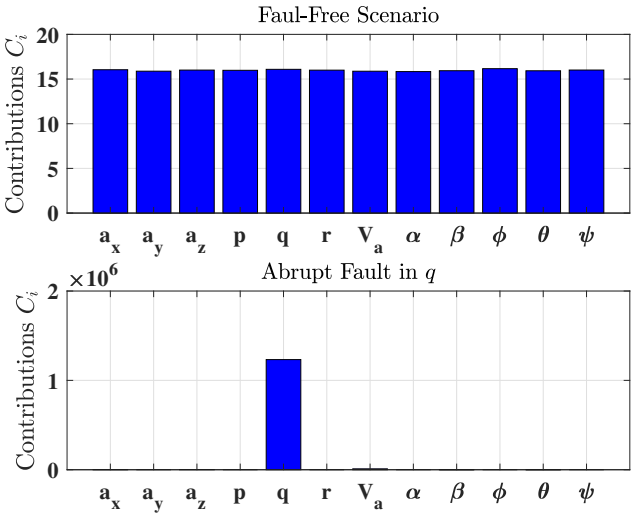

Figure 4.13: Contributions C_i to squared prediction error for each of the i monitored variables in fault-free scenario (top) and abrupt fault scenario in pitch rate q (table 5.3).

4.5 EKF-ATLMS: A Novel Fault Detection and Diagnosis Approach

This approach combines the aircraft kinematic equations (section 4.3.1) and an extended Kalman filter for residual generation (section 4.3.2). Besides that, the ATLMS algorithm (section 4.2.3 and appendix E) is used to minimize false alarms due to changes in flight operating conditions through adequate ATLMS parameter tuning. The EKF-ATLMS approach does not require data training as in PCA approach or the development of aircraft linear models. Figure 4.14 shows the general scheme of the EKF-ATLMS approach.

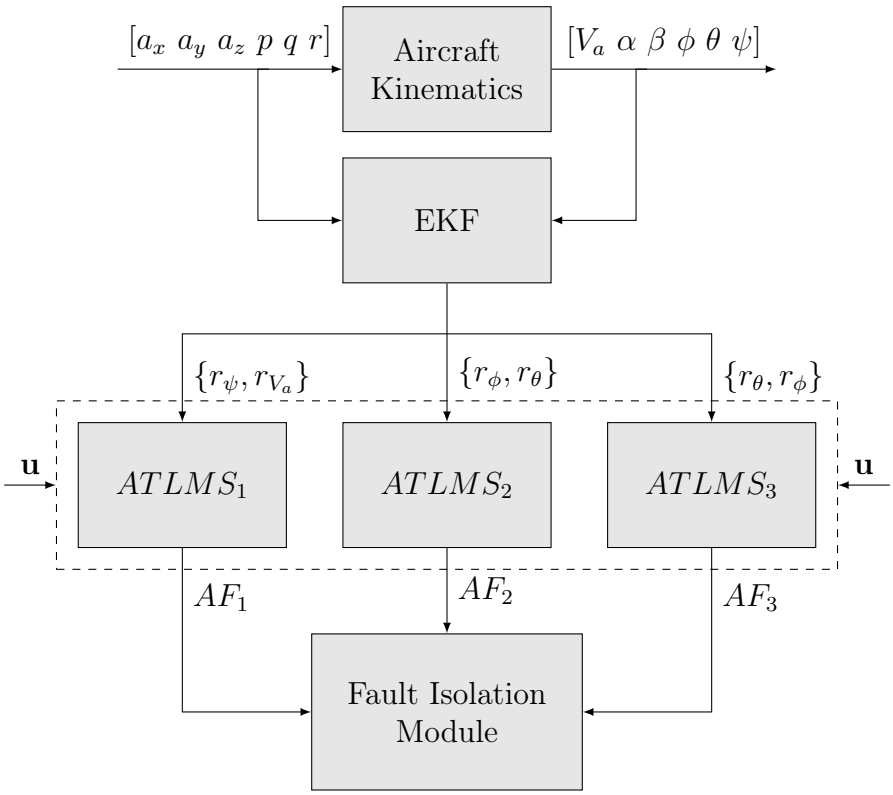

Figure 4.14: A novel fault detection and diagnosis approach based on the aircraft kinematic equations and the ATLMS method. The input vector of the EKF is composed of the aircraft accelerations (a_x, a_y, a_z) and aircraft angular rates (p, q, r); The output vector of the EKF is composed of the attitude angles (ϕ, θ, ψ) and aircraft airspeed V_a, angle of attack α, and sideslip angle β. $\{r_i, r_j\}$ is the pair of EKF-based residuals from measurements i and j, respectively. AF_n, with $n = 1, 2, 3$, indicates the alarm flag of each ATLMS module. $\mathbf{u}$ is the control vector composed of the control signals for the elevator δ_e, aileron δ_a, rudder δ_r, and thrust δ_t.

Instead of using ten ATLMS filters as in the KF-ATLMS fault detection strategy (section 4.2.4), only three ATLMS filters with different pairs of residuals (figure 4.14) are required to detect and diagnosis proposed fault scenarios described in table 5.3. Table 4.15 shows the tuning of ATLMS parameters used for simulations.

Table 4.15: ATLMS parameter tuning for Kinematic ATLMS approach. r_1 and r_0 = evaluated residuals; e_0 = safety offset; a = sensitivity factor; μ = convergence rate.

	r_0	r_1	e_0	a	μ
ATLMS_1	r_ψ	r_{V_a}	3	-0.1	0.005
ATLMS_2	r_ϕ	r_θ	1	-0.1	0.005
ATLMS_3	r_θ	r_ϕ	0.05	-0.1	0.005

4.5.1 EKF-ATLMS Fault Diagnosis Approach

Instead of using sensitive and insensitive residuals from the decoupled linear models, fault isolation takes into account an intrinsic characteristic of the logarithmic likelihood ratio $L_k = \frac{r_{0k}^2 - r_{1k}^2}{2\sigma_0^2}$ (eqs. (E.21) and (E.22)) used in the ATLMS algorithm (table 4.5 and appendix E).

In case of fault occurrence in the variable described by residual r_{1k}, the adaptive threshold ATLMS assumes negative values ($\text{ATLMS}_k < r_{0k}$). Conversely, in case of fault occurrence in the variable described by residual r_{0k}, the adaptive threshold ATLMS assumes positive values ($\text{ATLMS}_k \geq r_{0k}$). As a consequence, suitably defined pairs of EKF-based residuals $\{r_0, r_1\}$ provide different sign patterns of the adaptive threshold that are convenient for fault isolation as presented in table 4.16. Diagnosis results are presented in section 5.3.

Besides that, the deflection of the adaptive threshold can be used to analyze fault severity. The higher the deflection of the adaptive threshold the higher the fault amplitude. This analysis is similar to the contributions to SPE presented in the data-driven approach (section 4.4.4 and section 5.3).

Table 4.16: Isolation patterns for faults in roll rate p, pitch rate q, and aircraft acceleration a_x. The positive sign + indicates that the adaptive threshold keeps positive values after fault occurrence ($\text{ATLMS}_k \geq r_{0k}$). On the other hand, the negative sign − indicates that the adaptive threshold assumes negative values after fault occurrence ($\text{ATLMS}_k < r_{0k}$).

	Adaptive Threshold Sign Patterns for Fault Isolation					
	r_0	r_1	Faults in p	Faults in q	Faults in a_x	No Fault
ATLMS_1	r_ψ	r_{V_a}	−	−	−	+
ATLMS_2	r_ϕ	r_θ	+	−	+	+
ATLMS_3	r_θ	r_ϕ	−	+	+	+

Chapter 5

Comparative Results and Discussion

In this chapter, the simulation results and comparison of the four proposed IMU sensor fault detection and diagnosis approaches for the Elektra 2 Solar aircraft are presented. They are analyzed regarding different fault scenarios in pitch rate q, roll rate p and aircraft acceleration a_x measurements. Besides that, results with real flight data are used for validation purposes.

5.1 Simulation Methodology and General Assumptions

The simulation methodology consists of 9 different flight scenarios with each of the proposed IMU faults presented in tables 5.3 and 5.4, and the following assumptions:

i) Occurrence of single, additive faults in primary IMU;

ii) Proposed fault types are abrupt (bias) and incipient (drift) faults [57];

iii) Backup IMU as well as other aircraft sensors do not fail;

Proposed faults cover both longitudinal and lateral aircraft dynamics and were chosen based on discussions with Elektra Solar team and a benchmark study on fault diagnosis [57]. Abrupt faults f_{abrupt} are modelled as a step function defined by fault amplitude a and time of fault occurrence t_f

$$f_{abrupt} := \begin{cases} 0, & t < t_f \\ a, & t \geq t_f \end{cases} \tag{5.1}$$

and incipient faults $f_{incipient}$ are modelled as a ramp function defined by fault slope a and time of fault occurrence t_f

$$f_{incipient} := \begin{cases} 0, & t < t_f \\ a(t - t_f), & t \geq t_f \end{cases} \tag{5.2}$$

For the sake of simplification, all faults are introduced at $t_f = 50$ s and fault amplitude/slope a is defined in table 5.3.

During the process of fault detection, four decision situations may arise as provided in table 5.1. Based on such decision situations and [57], the performance metrics used to evaluate the four different approaches regarding their capability to detect faults is the True Detection Rate (TDR), also known as probability of detection or detection sensitivity.

$$TDR = \frac{\text{Number of Detected Fault Alarms}}{\text{Number of Detected Fault Alarms} + \text{Number of Missed Alarms}} \tag{5.3}$$

Table 5.1: Decision situations for fault detection strategies. $\mathcal{H}_0$ indicates the hypothesis of no fault and $\mathcal{H}_1$ indicates the hypothesis of fault occurrence.

	Decide $\mathcal{H}_0$	Decide $\mathcal{H}_1$
$\mathcal{H}_0$ true (no fault)	Proper decision	False alarm
$\mathcal{H}_1$ true (fault)	Missed alarm	Proper decision

As shown in table 5.2, all simulations were done in MATLAB/Simulink 2017b with sampling time of 0.01 s.

Table 5.2: MATLAB/Simulink Model Configuration Parameters

Software Version	MATLAB/Simulink 2017b
Simulation Start Time	0
Simulation Stop Time	100 or 120
Solver	ode3 (Bogacki-Shampine)
Solver Type	Fixed-step
Sample Time	0.01

Table 5.3: Simulation Scenarios: faults in pitch rate q covers the longitudinal aircraft dynamics and faults in roll rate p covers the lateral dynamics of the aircraft. Amplitude of abrupt and incipient faults are given in rad/s. Amplitude of faults in aircraft acceleration is given in m/s^2. One hundred simulations were performed in each fault scenario with linearly spaced fault amplitudes within the range indicated in the last column.

Scenarios	**Type**	**Measurement**	**Fault Amplitude/Slope**
Scenario 1	No Fault	-	-
Scenario 2	Abrupt	q	from 0.005 to 0.5 rad/s
Scenario 3	Incipient	q	from 0.0002 to 0.02 rad/s
Scenario 4	Abrupt	p	from 0.005 to 0.5 rad/s
Scenario 5	Incipient	p	from 0.0002 to 0.02 rad/s
Scenario 6	Abrupt	a_x	from 0.1 to 1 m/s^2
Scenario 7	Incipient	a_x	from 0.0002 to 0.02 m/s^2

Table 5.4: Simulation scenarios with changing flight conditions. Faults introduced here are the same from table 5.3. V_a is the aircraft airspeed; ψ is the yaw angle; and AGL is the aircraft altitude above ground.

Scenarios	**Nominal Flight Cond.**	**Updated Flight Cond.**	**Time**
Scenario 8	$V_a = 18$ m/s	$V_a = 20$ m/s	30 s
	$AGL = 500$ m	$AGL = 510$ m	50 s
	$\psi = 138°$	$\psi = 155°$	70 s
	No fault	No fault	-
Scenario 9	$V_a = 18$ m/s	$V_a = 20$ m/s	30 s
	$AGL = 500m$	$AGL = 510m$	50 s
	$\psi = 138°$	$\psi = 155°$	70 s
	No fault	Abrupt fault in p	100 s

5.2 Fault Detection Results

5.2.1 Scenario 1: Fault-free case

Figures 5.1 and 5.2 show the adaptive thresholds and fault flags for longitudinal and lateral aircraft dynamics, respectively. Figure 5.3 shows the decision function (MSE) of the EKF-based approach and their respective thresholds. The normal condition of the decision function (SPE) for the PCA-based approach is shown in figure 4.12 (bottom). As expected for a fault-free scenario, the residuals are close to zero and none of the fault alarms are active. Figures 5.4 - 5.7 present the aircraft accelerations (m/s^2), angular rates (rad/s), airspeed (m/s), aerodynamic angles (rad) and altitude above ground (m) for a typical flight condition ($V_a = 18$ m/s and $AGL = 500$ m).

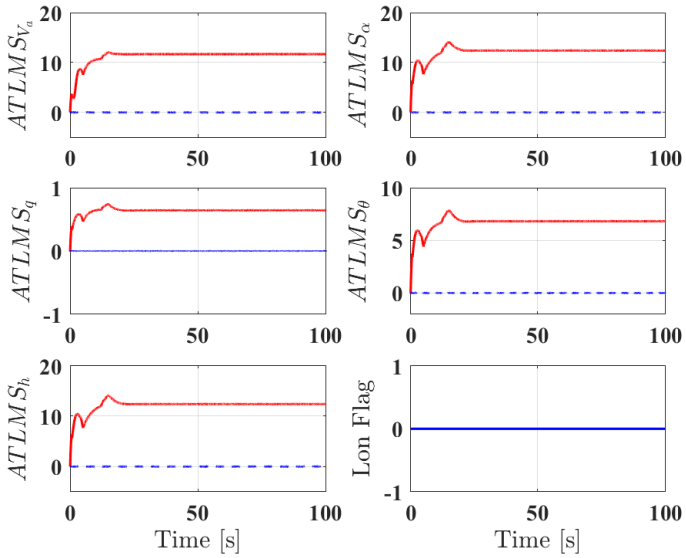

Figure 5.1: Adaptive thresholds (red), insensitive residuals r_0 (blue), and fault flag for longitudinal measurements in fault-free scenario. ATLMS$_i$ refers to the adaptive threshold of measurement $i = V_a$, α, q, θ, h. A fault is detected when ATLMS$_i$ (red) $< r_0$ (blue). As expected, the longitudinal alarm flag *Lon Flag* is not activated in fault-free scenario.

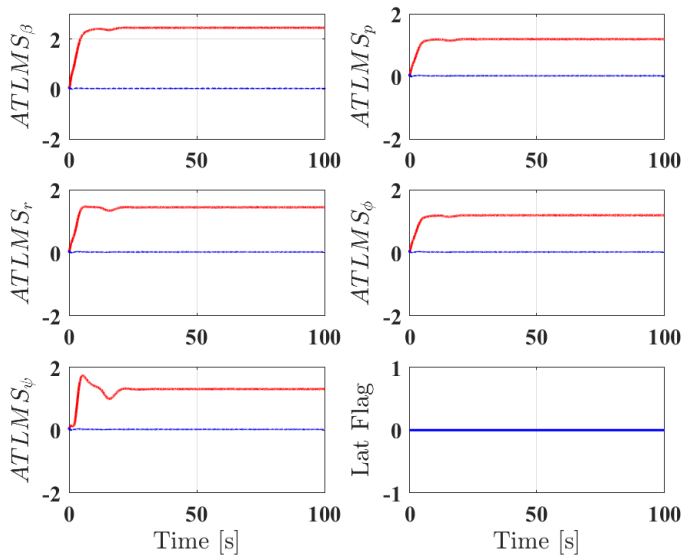

Figure 5.2: Adaptive thresholds (red), insensitive residuals r_0 (blue), and fault flag for lateral measurements in fault-free scenario. ATLMS$_j$ refers to the adaptive threshold of measurement $j = \beta$, p, r, ϕ, ψ. A fault is detected when ATLMS$_j$ (red) $< r_0$ (blue). As expected, the lateral alarm flag *Lat Flag* is not activated in fault-free scenario.

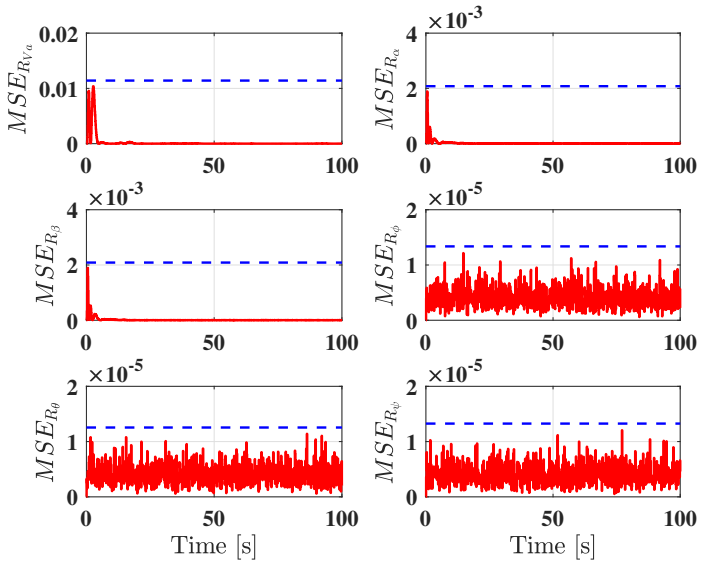

Figure 5.3: Residual mean squared error (red) for the EKF-based approach in fault-free scenario. Decision thresholds (blue) are defined in table 4.11. As expected, none of the residual MSE crosses their respective decision threshold.

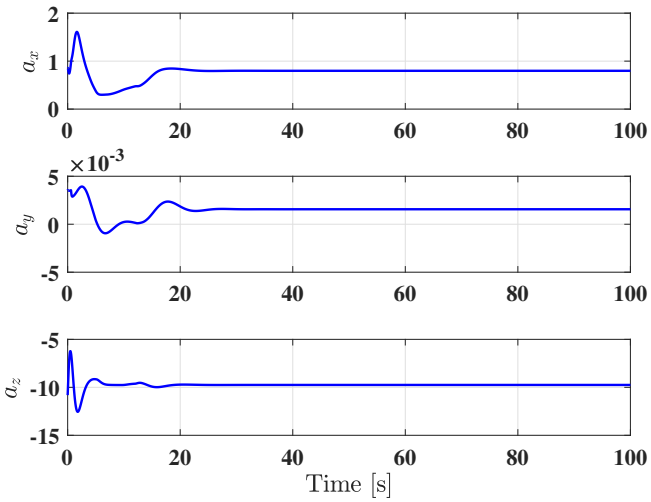

Figure 5.4: Aircraft accelerations a_x, a_y, and a_z (m/s^2) for fault-free scenario.

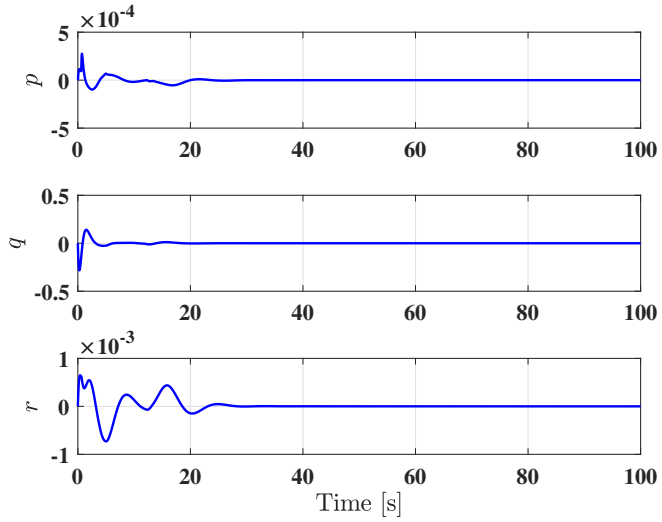

Figure 5.5: Aircraft angular rates p, q, and r (rad/s) for fault-free scenario.

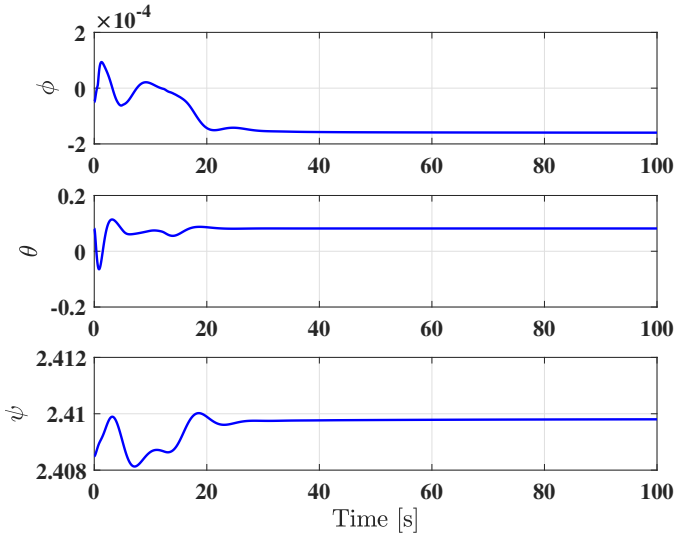

Figure 5.6: Aircraft roll ϕ, pitch θ and yaw ψ angles (rad) for fault-free scenario.

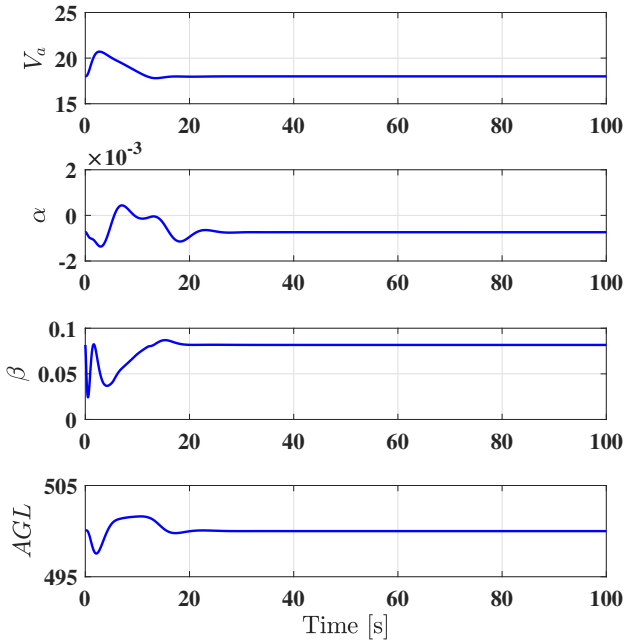

Figure 5.7: Aircraft airspeed V_a (m/s), angle of attack α and sideslip angle β (rad) and altitude above ground AGL (m) for fault-free scenario.

5.2.2 Scenario 2: Abrupt fault in pitch rate q

An abrupt fault in pitch rate q is described as follows

$$q_{fabrupt} = q + f_{abrupt} \tag{5.4}$$

where f_{abrupt} is modelled as a step function described in eq. (5.1) and fault amplitude is defined in table 5.3.

Detection results for scenario 2 are summarized in figure 5.8. Regarding the KF-ATLMS approach, an abrupt fault in pitch rate q affects the longitudinal dynamics of the aircraft but not the lateral one, since longitudinal and lateral linear models were designed to be decoupled. Consequently, the longitudinal alarm flag is activated after fault occurrence while the lateral alarm flag is kept inactive (figs.5.9 and 5.10). However, faults with smaller amplitudes may not be detected by this approach. One reason for this behavior can be related to deficiencies in modelling uncertainties and unknown parameters during the linear model development. Both EKF-based and PCA-based approaches presented excellent detection results considering the proposed scenarios, with a slightly better performance of the latter over the former. Figures 5.11 and 5.12 present the decision function and threshold for the EKF-based approach and data-driven one, respectively.

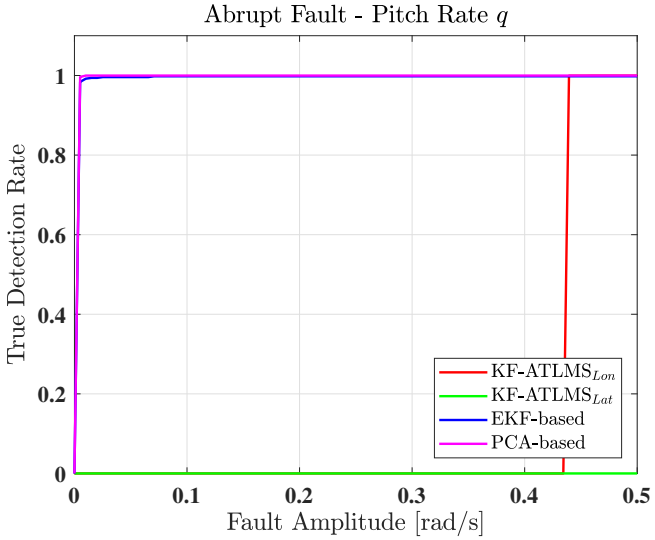

Figure 5.8: True detection rate of KF-ATLMS, EKF-based and PCA-based fault detection approaches regarding abrupt faults in pitch rate q.

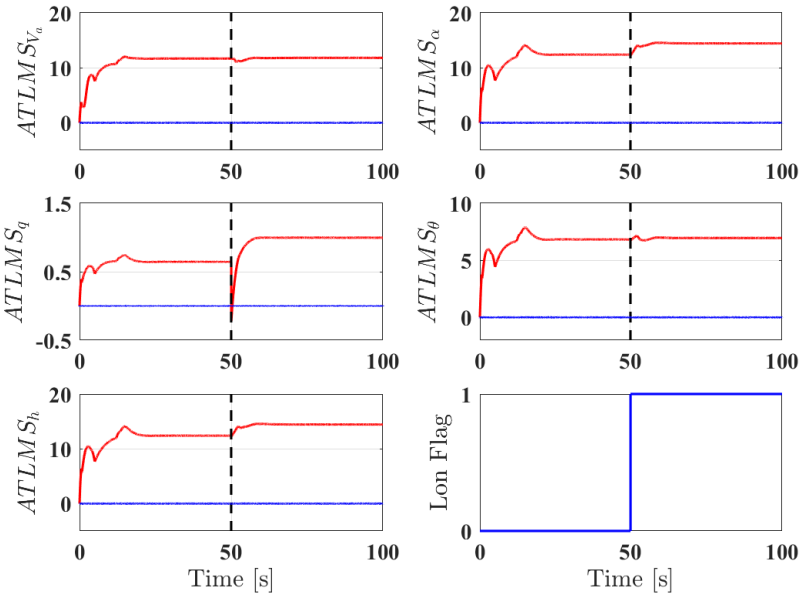

Figure 5.9: Adaptive thresholds (red), insensitive residuals r_0 (blue), and longitudinal fault flag for an abrupt fault of amplitude 0.5 rad/s in pitch rate q. ATLMS$_i$ refers to the adaptive threshold of measurement $i = V_a$, α, q, θ, h. In this case, a fault is detected when ATLMS$_q$ (red) $< r_0$ (blue).

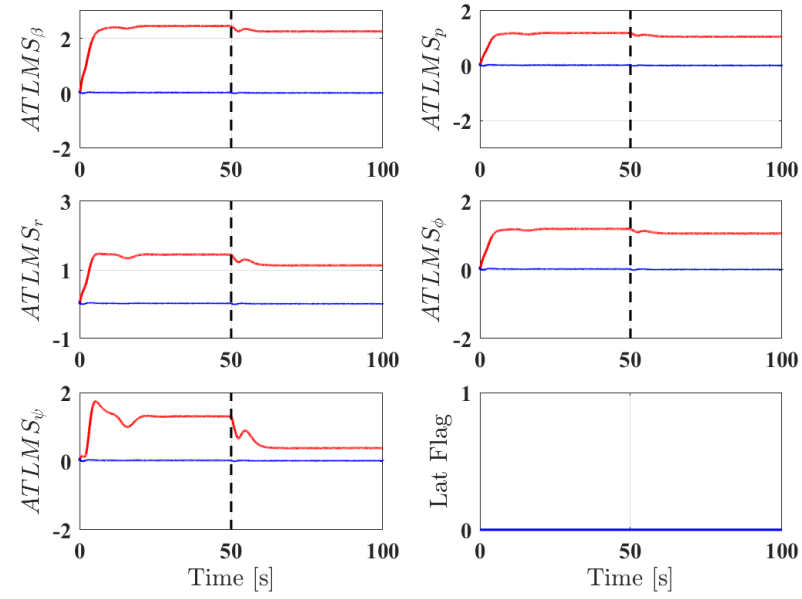

Figure 5.10: Adaptive thresholds (red), insensitive residuals r_0 (blue), and lateral fault flag for an abrupt fault of amplitude 0.5 rad/s in pitch rate q. ATLMS$_j$ refers to the adaptive threshold of measurement $j = \beta$, p, r, ϕ, ψ. A fault is detected when ATLMS$_j$ $< r_0$. In this case, an abrupt fault in pitch rate q is not detected by lateral adaptive thresholds.

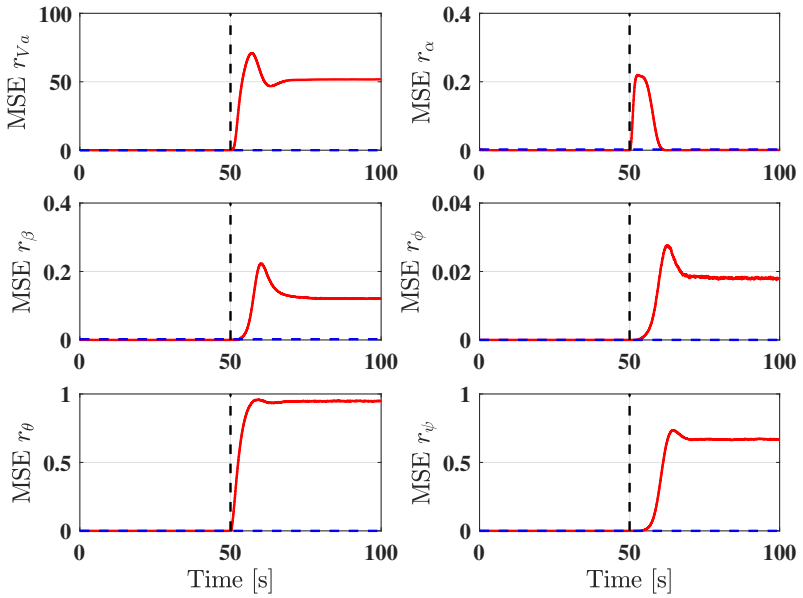

Figure 5.11: Residual mean squared error for EKF-based approach for an abrupt fault of amplitude 0.5 rad/s in pitch rate q. MSE r_i indicates the residual MSE of measurement $i = V_a$, α, β, ϕ, θ, ψ. A fault is detected when any of the decision functions (red) exceeds their respective thresholds (blue).

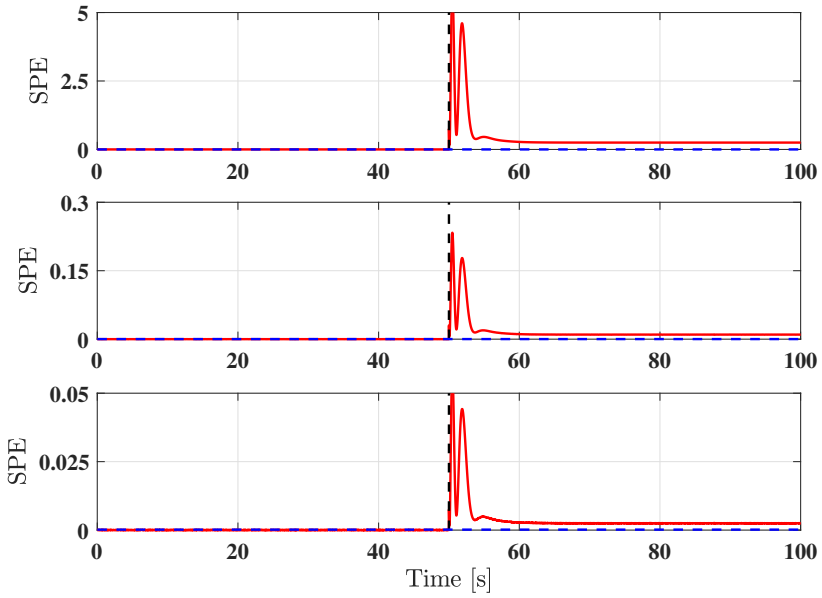

Figure 5.12: Residual squared prediction error for the PCA-based approach regarding abrupt faults in pitch rate q with fault amplitude of 0.5 rad/s (top), 0.1 rad/s (middle), and 0.05 rad/s (bottom). A fault is detected when any of the decision functions (red) exceeds their respective thresholds (blue).

5.2.3 Scenario 3: Incipient fault in pitch rate q

An incipient fault in pitch rate q is described as follows

$$q_{fincipient} = q + f_{incipient} \tag{5.5}$$

where $f_{incipient}$ is modelled as a ramp function described in eq. (5.2) and fault slope is defined in table 5.3.

Detection results for scenario 3 are summarized in figure 5.13. Regarding the KF-ATLMS approach, the proposed incipient fault in pitch rate q is not detected, resulting in undesired missed alarms. Consequently, both longitudinal and lateral alarm flags are not activated after fault occurrence (figs.5.14 and 5.15). The detection performance could be improved by proper tuning of ATLMS parameters. On the other hand, EKF-based and PCA-based approaches presented excellent detection results considering the proposed scenarios, with a slightly better performance of the latter over the former. Figures 5.16 and 5.17 present the decision function and threshold for the EKF-based approach and PCA-based one, respectively.

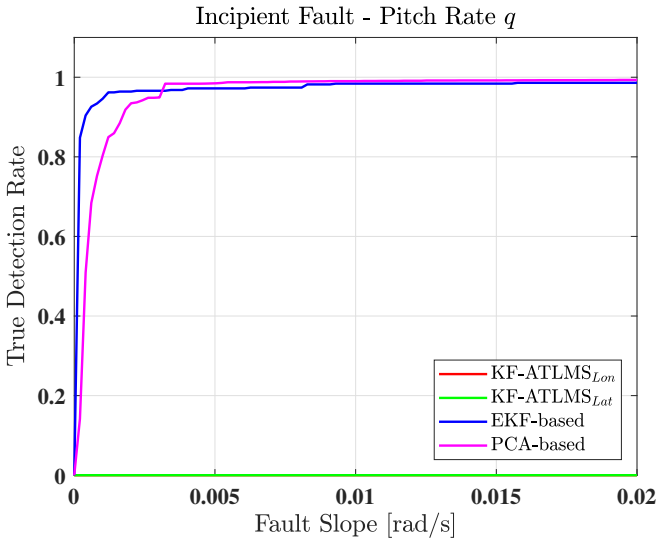

Figure 5.13: True detection rate of KF-ATLMS, EKF-based and PCA-based fault detection approaches regarding incipient faults in pitch rate q.

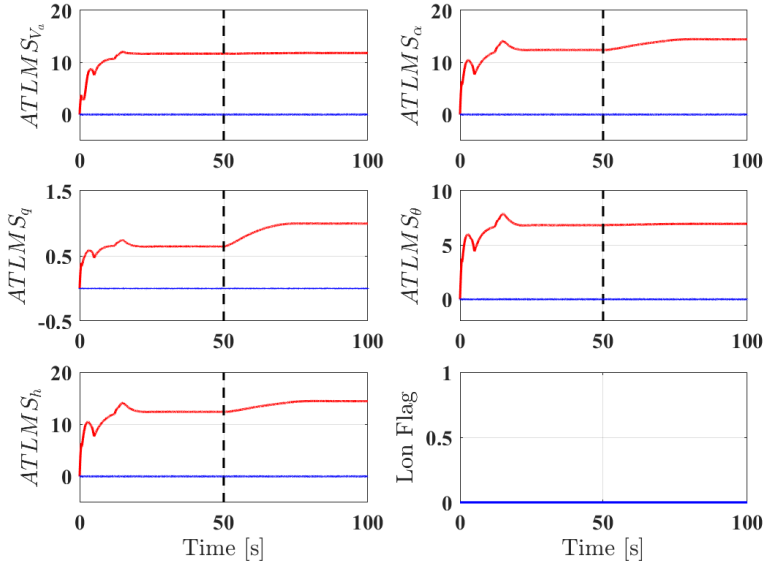

Figure 5.14: Adaptive thresholds (red), insensitive residuals r_0 (blue), and longitudinal fault flag for an incipient fault of slope 0.02 rad/s in pitch rate q. ATLMS$_i$ refers to the adaptive threshold of measurement $i = V_a$, α, q, θ, h. A fault is detected when ATLMS$_i$ (red) $< r_0$ (blue). In this case, the proposed fault is not detected by any longitudinal adaptive thresholds, causing undesired missed alarms.

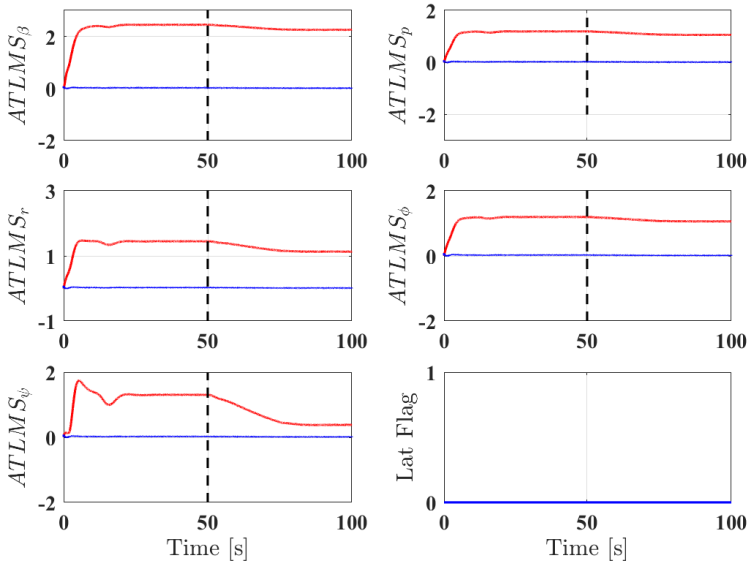

Figure 5.15: Adaptive thresholds (red), insensitive residuals r_0 (blue), and lateral fault flag for with an incipient fault of slope 0.02 rad/s in pitch rate q. ATLMS$_j$ refers to the adaptive threshold of measurement $j = \beta$, p, r, ϕ, ψ. A fault is detected when ATLMS$_j$ $< r_0$. As expected, faults in pitch rate q do not provide lateral fault alarm flags.

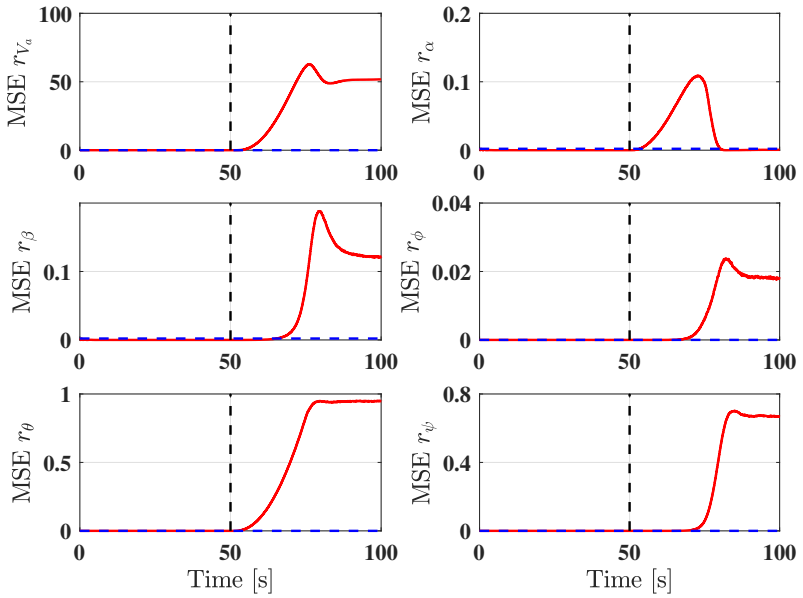

Figure 5.16: Residual mean squared error for EKF-based approach for an incipient fault of slope of 0.02 rad/s. MSE r_i indicates the residual MSE of measurement $i = V_a$, α, β, ϕ, θ, ψ. A fault is detected when any of the decision functions (red) exceeds their respective thresholds (blue).

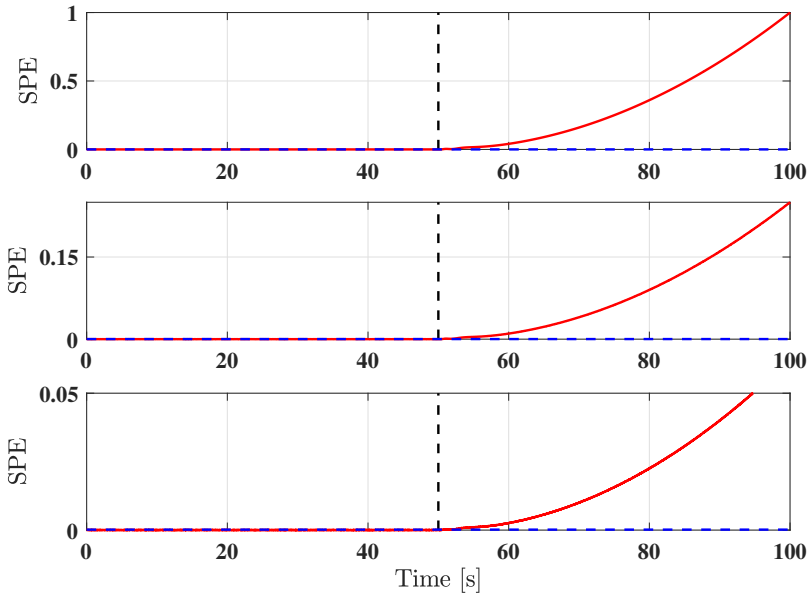

Figure 5.17: Residual squared prediction error for the PCA-based approach regarding incipient faults in pitch rate q with fault amplitude of 0.02 rad/s (top), 0.01 rad/s (middle), and 0.005 rad/s (bottom). A fault is detected when any of the decision functions (red) exceeds their respective thresholds (blue).

5.2.4 Scenario 4: Abrupt Fault in roll rate p

An abrupt fault in roll rate p is described as follows

$$p_{fabrupt} = p + f_{abrupt} \tag{5.6}$$

where f_{abrupt} is modelled as a step function described in eq. (5.1) and fault amplitude is defined in table 5.3.

Detection results for scenario 4 are summarized in figure 5.18. Regarding the KF-ATLMS approach, an abrupt fault in roll rate p affects the lateral dynamics of the aircraft but not the longitudinal one, since longitudinal and lateral linear models were designed to be decoupled. Consequently, the lateral alarm flag is activated after fault occurrence while the longitudinal alarm flag is kept inactive (figs.5.19 and 5.20). However, faults with smaller amplitudes may not be detected by this approach. Both EKF-based and PCA-based approaches presented excellent detection results considering the proposed scenarios, with a slightly better performance of the latter over the former. Figures 5.21 and 5.22 present the decision function and threshold for the EKF-based approach and data-driven ones, respectively.

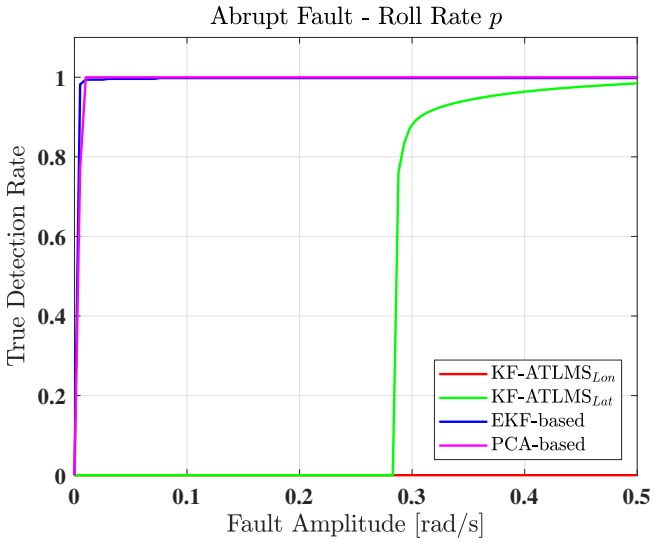

Figure 5.18: True detection rate of KF-ATLMS, EKF-based and PCA-based fault detection approaches regarding abrupt faults in roll rate p.

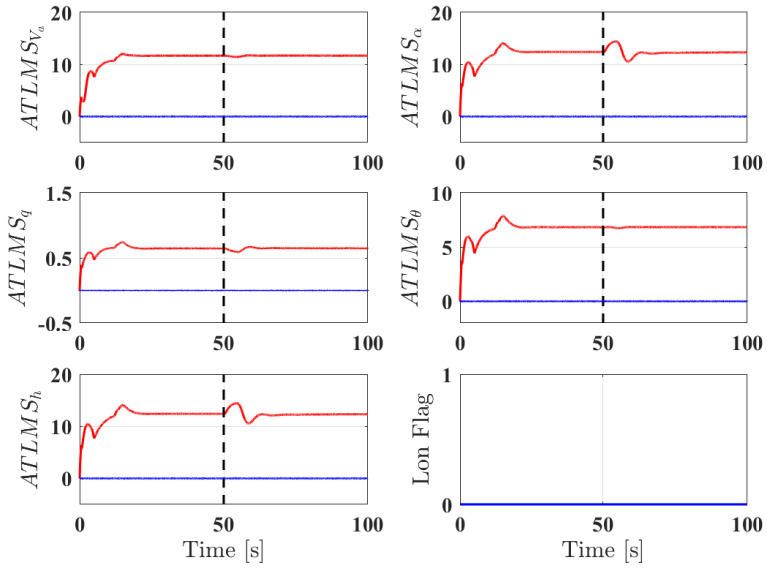

Figure 5.19: Adaptive thresholds (red), insensitive residuals r_0 (blue), and longitudinal fault flag for an abrupt fault of amplitude 0.5 rad/s in roll rate p. ATLMS$_i$ refers to the adaptive threshold of measurement $i = V_a$, α, q, θ, h. A fault is detected when ATLMS$_i$ (red) $< r_0$ (blue). As expected, an abrupt fault in roll rate p is not detected by longitudinal adaptive thresholds.

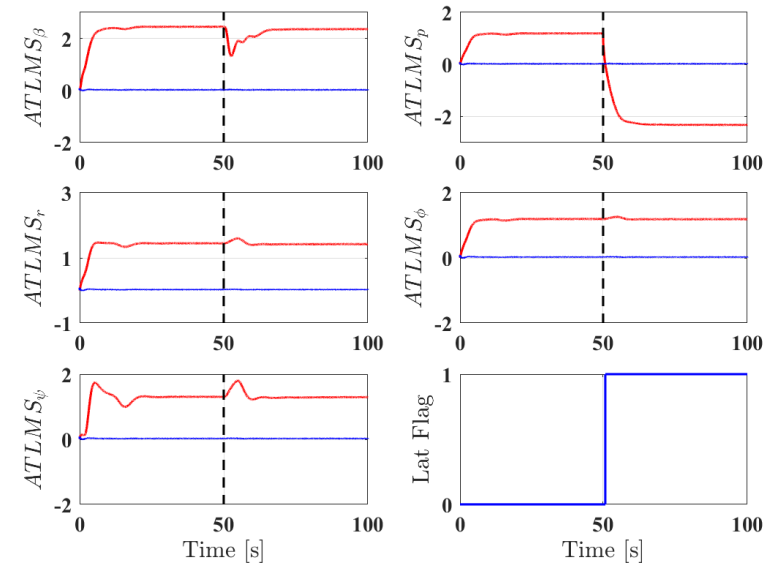

Figure 5.20: Adaptive thresholds (red), insensitive residuals r_0 (blue), and longitudinal fault flag for an abrupt fault of amplitude 0.5 rad/s in roll rate p. ATLMS$_j$ refers to the adaptive threshold of measurement $j = \beta$, p, r, ϕ, ψ. In this case, a fault is detected when ATLMS$_p$ (red) $< r_0$ (blue).

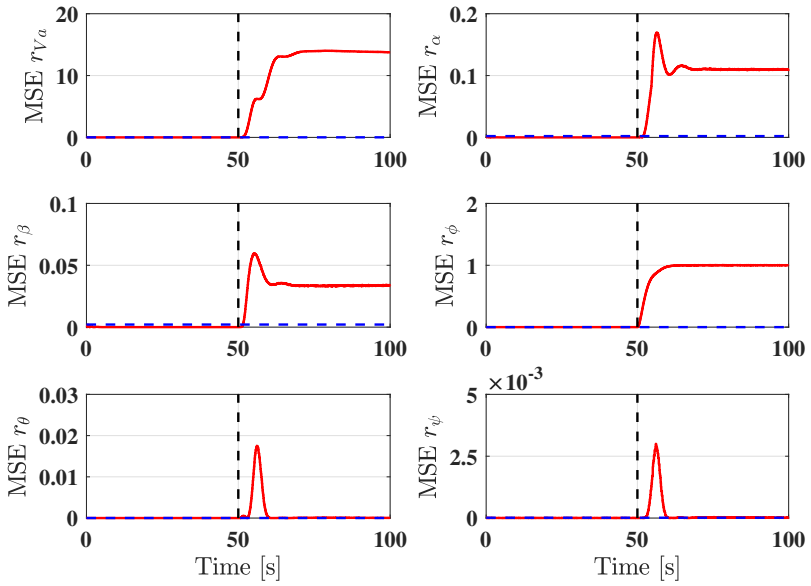

Figure 5.21: Residual mean squared error for EKF-based approach for an abrupt fault of amplitude 0.5 rad/s in roll rate p. MSE_{r_i} indicates the residual MSE of measurement $i = V_a$, α, β, ϕ, θ, ψ. A fault is detected when any of the decision functions (red) exceeds their respective thresholds (blue).

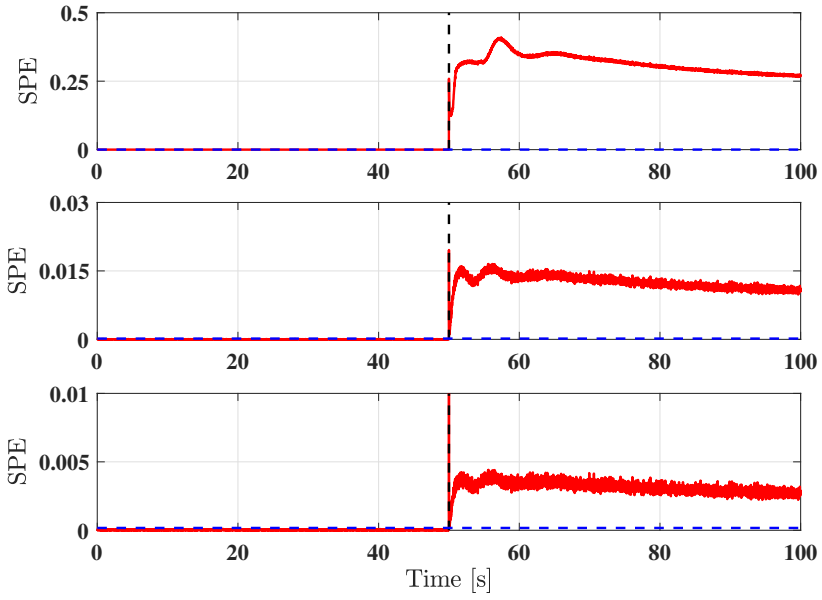

Figure 5.22: Residual squared prediction error for the PCA-based approach regarding abrupt faults in roll rate p with fault amplitude of 0.5 rad/s (top), 0.1 rad/s (middle), and 0.05 rad/s (bottom). A fault is detected when any of the decision functions (red) exceeds their respective thresholds (blue).

5.2.5 Scenario 5: Incipient Fault in roll rate p

An incipient fault in roll rate p is described as follows

$$p_{fincipient} = p + f_{incipient} \tag{5.7}$$

where $f_{incipient}$ is modelled as a ramp function described in eq. (5.2) and fault slope is defined in table 5.3.

Detection results for scenario 5 are summarized in figure 5.23. Regarding the KF-ATLMS approach, an incipient fault in roll rate p affects the lateral dynamics of the aircraft but not the longitudinal one (figs.5.24 and 5.25). For small, incipient faults in p, the detection performance of the ATLMS decreases considerably. The True Detection Rate (TDR) goes from 0.66 (fault slope of 0.02 rad/s) to 0.049 (fault slope of 0.01 rad/s), and then to a missed alarm when the fault amplitude is 0.005 rad/s or less. One way to improve ATLMS detection results - not fully explored in this work - is to develop a systematic methodology for ATLMS parameter tuning. Both EKF-based and PCA-based approaches presented good detection results considering the proposed scenarios, with a slightly better performance of the former over the latter. Figures 5.26 and 5.27 present the decision function and threshold for the EKF-based approach and data-driven one, respectively.

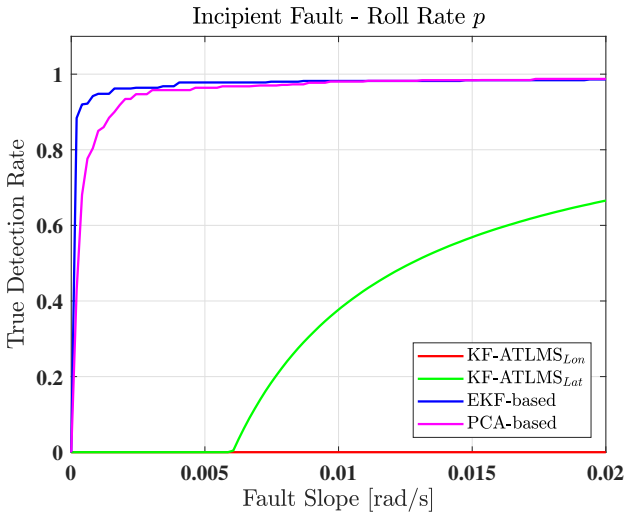

Figure 5.23: True detection rate of KF-ATLMS, EKF-based and PCA-based fault detection approaches regarding incipient faults in roll rate p.

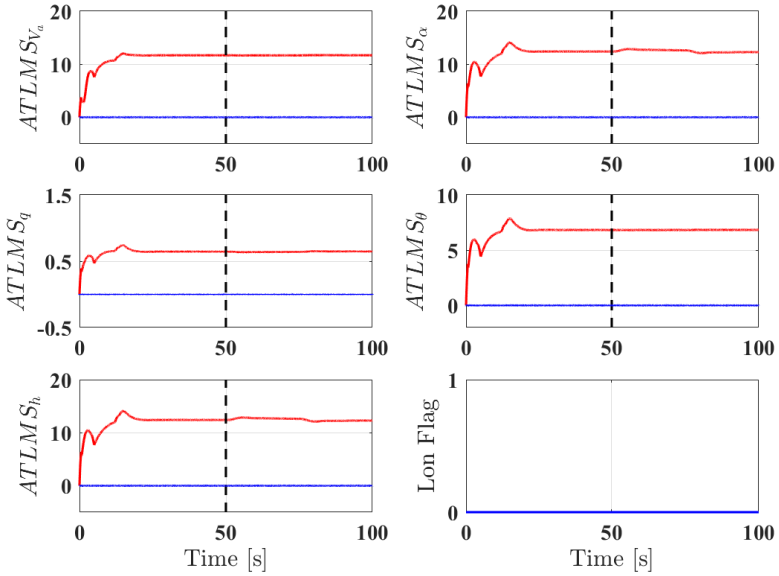

Figure 5.24: Adaptive thresholds (red), insensitive residuals r_0 (blue), and longitudinal fault flag for an incipient fault of slope 0.02 rad/s in roll rate p. ATLMS$_i$ refers to the adaptive threshold of measurement $i = V_a$, α, q, θ, h. A fault is detected when ATLMS$_i$ (red) $< r_0$ (blue). As expected, faults in roll rate p do not provide longitudinal fault alarm flags.

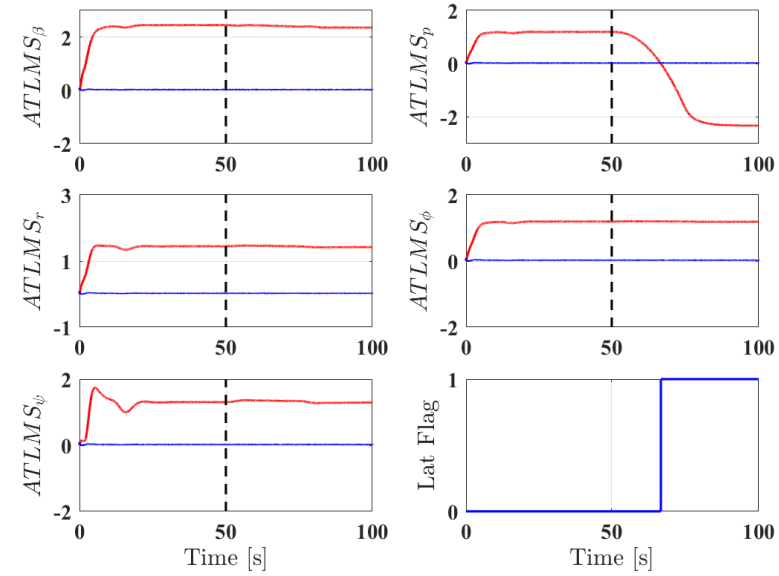

Figure 5.25: Adaptive thresholds (red), insensitive residuals r_0 (blue), and lateral fault flag for with an incipient fault of slope 0.02 rad/s in roll rate p. ATLMS$_j$ refers to the adaptive threshold of measurement $j = \beta$, p, r, ϕ, ψ. In this case, a fault is detected when ATLMS$_p$ (red) $< r_0$ (blue).

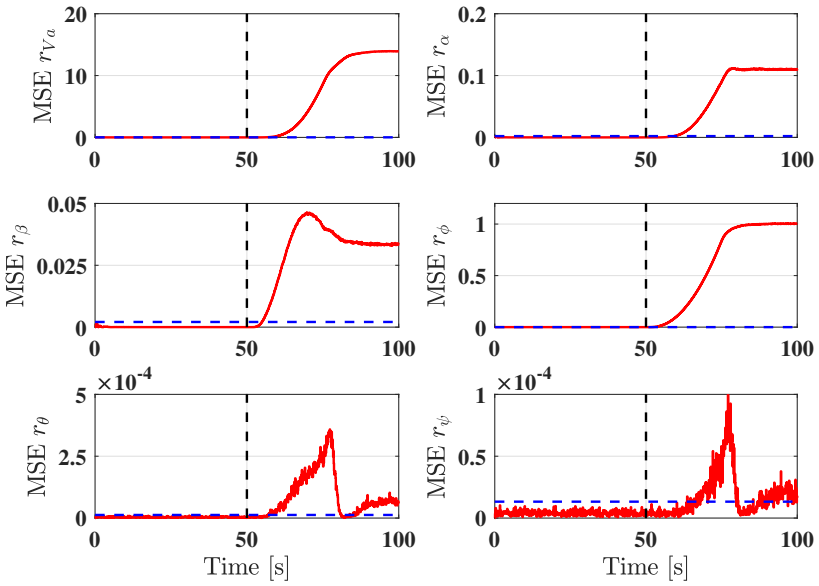

Figure 5.26: Residual mean squared error for EKF-based approach for an incipient fault of slope of 0.02 rad/s. MSE_{r_i} indicates the residual MSE of measurement $i = V_a$, α, β, ϕ, θ, ψ. A fault is detected when any of the decision functions (red) exceeds their respective thresholds (blue).

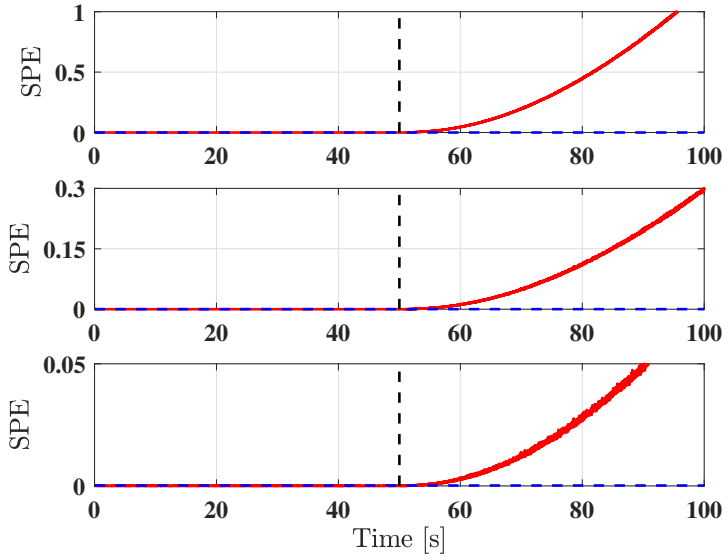

Figure 5.27: Residual squared prediction error for the PCA-based approach regarding incipient faults in roll rate p with fault amplitude of 0.02 rad/s (top), 0.01 rad/s (middle), and 0.005 rad/s (bottom). A fault is detected when any of the decision functions (red) exceeds their respective thresholds (blue).

5.2.6 Scenario 6: Abrupt fault in aircraft acceleration a_x

An abrupt fault in aircraft acceleration a_x is described as follows

$$a_{xf_{abrupt}} = a_x + f_{abrupt} \tag{5.8}$$

where f_{abrupt} is modelled as a step function described in eq. (5.1) and fault amplitude is defined in table 5.3.

Detection results for scenario 6 are summarized in figure 5.28. Regarding the KF-ATLMS approach, the proposed abrupt fault in acceleration measurement a_x was not detected, causing undesired missed alarms (figs.5.29 and 5.30). The reason for that relies on the fact that aircraft accelerations are not taken into account during the linearization procedure (section 4.2.1). Both EKF-based and PCA-based approaches presented good detection results considering fault amplitudes of 1 m/s^2 and 0.5 m/s^2, with a better performance of the latter over the former. With a fault amplitude of 0.1 m/s^2, however, the True Detection Rate (TDR) of the fault detection module based on the kinematic model decreases considerably from 99% to 53.80%. Figures 5.31 and 5.32 present the decision function and threshold for the EKF-based approach and data-driven ones, respectively.

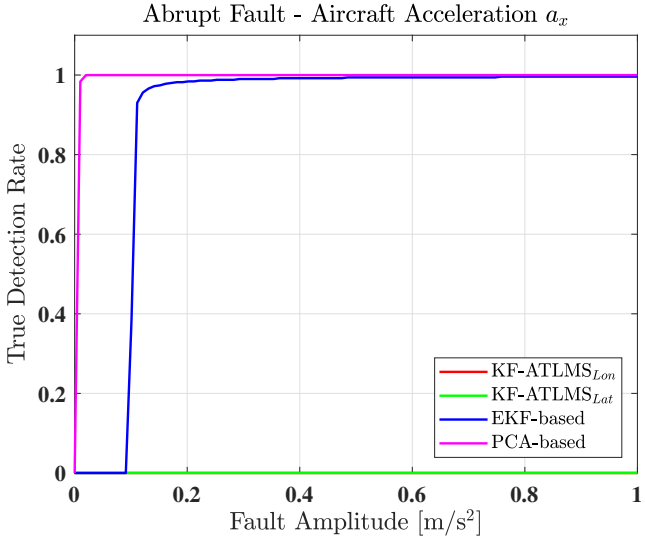

Figure 5.28: True detection rate of KF-ATLMS, EKF-based and PCA-based fault detection approaches regarding abrupt faults in aircraft acceleration a_x.

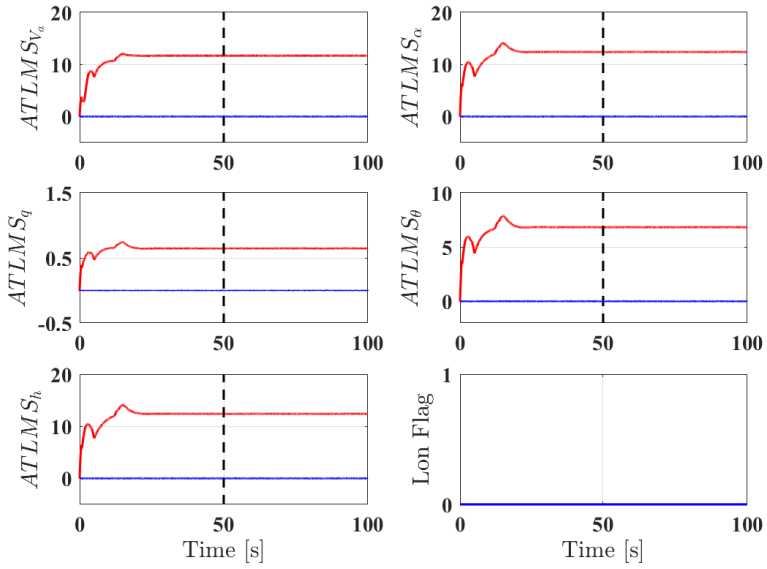

Figure 5.29: Adaptive thresholds (red), insensitive residuals r_0 (blue), and longitudinal fault flag for an abrupt fault of amplitude 1 m/s^2 in aircraft acceleration a_x. ATLMS$_i$ refers to the adaptive threshold of measurement $i = V_a$, α, q, θ, h. A fault is detected when ATLMS$_i$ (red) $< r_0$ (blue). In this case, the proposed fault is not detected by the longitudinal adaptive thresholds, causing undesired missed fault alarms.

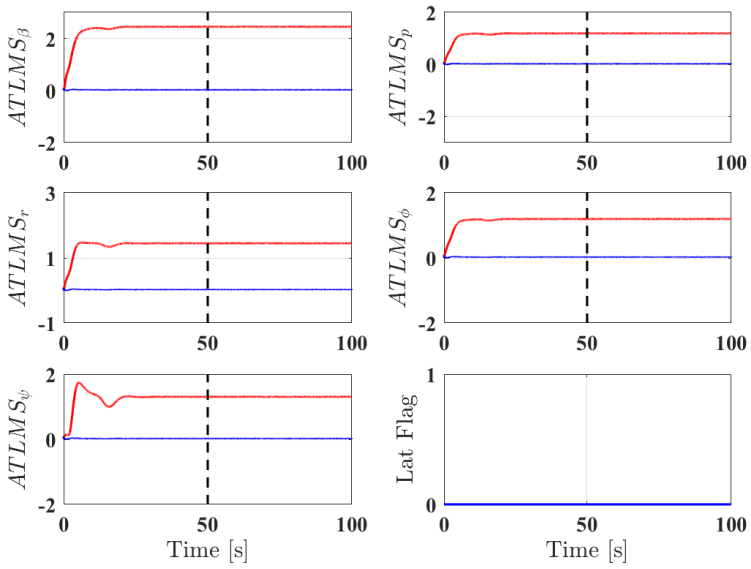

Figure 5.30: Adaptive thresholds (red), insensitive residuals r_0 (blue), and lateral fault flag for an abrupt fault of amplitude 1 m/s^2 in aircraft acceleration a_x. ATLMS$_j$ refers to the adaptive threshold of measurement $j = \beta$, p, r, ϕ, ψ. A fault is detected when ATLMS$_j$ (red) $< r_0$ (blue). In this case, the proposed fault is not detected by the lateral adaptive thresholds, causing undesired missed fault alarms.

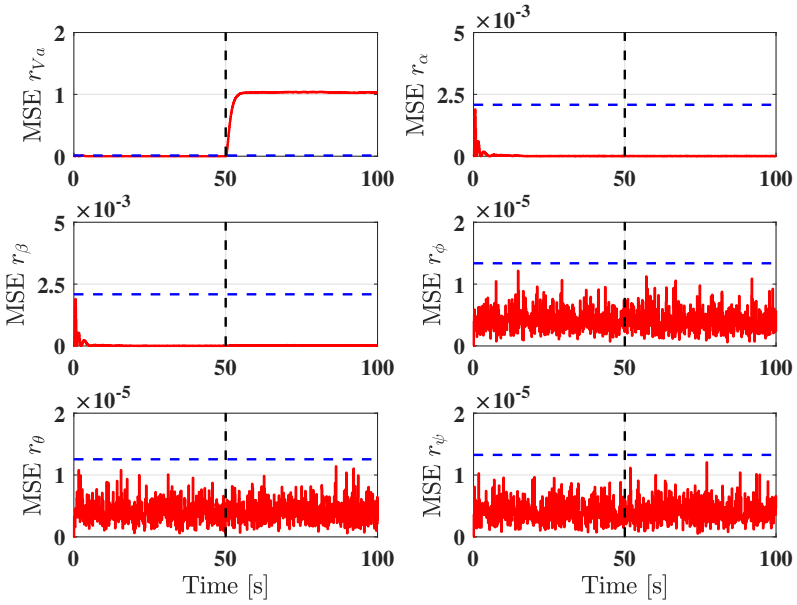

Figure 5.31: Residual mean squared error for EKF-based approach for an abrupt fault of amplitude 1 m/s^2 in aircraft acceleration a_x. MSE_{r_i} indicates the residual MSE of measurement $i = V_a$, α, β, ϕ, θ, ψ. A fault is detected when any of the decision functions (red) exceeds their respective thresholds (blue). In this case, only the MSE of the airspeed residual (r_{V_a}) is greater than its respective threshold, indicating fault occurrence.

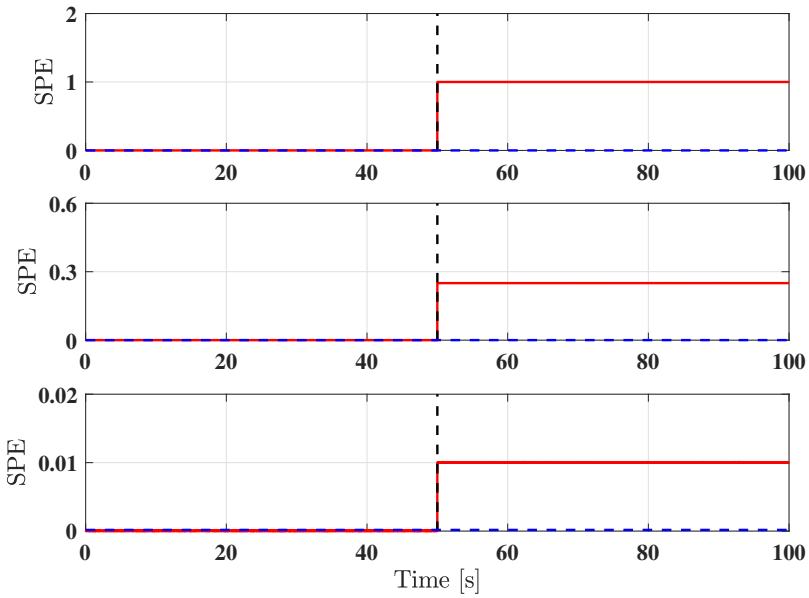

Figure 5.32: Residual squared prediction error for the PCA-based approach regarding abrupt faults in aircraft acceleration a_x with amplitude of 1 m/s^2 (top), 0.5 m/s^2 (middle), and 0.1 m/s^2 (bottom). A fault is detected when any of the decision functions (red) exceeds their respective thresholds (blue).

5.2.7 Scenario 7: Incipient fault in aircraft acceleration a_x

An incipient fault in aircraft acceleration a_x is described as follows

$$a_{xf_{incipient}} = a_x + f_{incipient} \tag{5.9}$$

where $f_{incipient}$ is modelled as a ramp function described in eq. (5.2) and fault slope is defined in table 5.3.

Detection results for scenario 7 are summarized in figure 5.33. Regarding the KF-ATLMS approach, the proposed incipient fault in acceleration measurement a_x was not detected, causing undesired missed alarms (figs.5.34 and 5.35). Again, aircraft accelerations are not taken into account during linear model extraction procedure (section 4.2.1). Both EKF-based and PCA-based approaches presented good detection results considering the range of fault amplitudes, with a better performance of the latter over the former. With a fault amplitude of 0.005 m/s^2, however, the True Detection Rate (TDR) of the fault detection module based on the EKF-based approach decreases considerably from 0.87 (fault amplitude of 0.02 m/s^2) to 0.56. Figures 5.36 and 5.37 present the decision function and threshold for the EKF-based approach and data-driven ones, respectively.

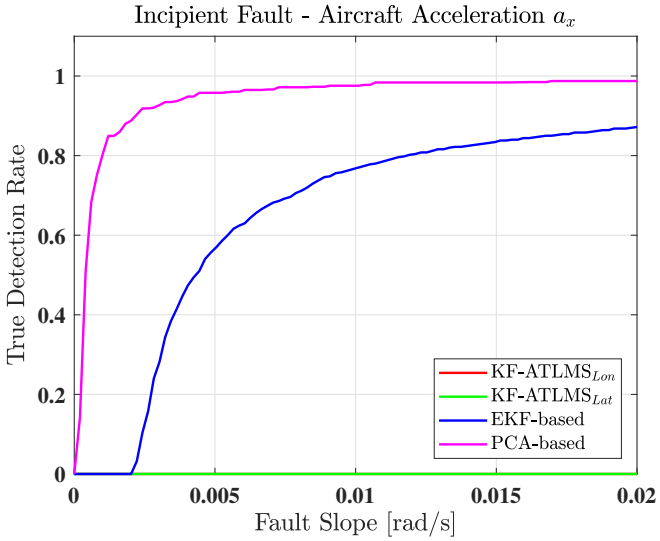

Figure 5.33: True detection rate of KF-ATLMS, EKF-based and PCA-based fault detection approaches regarding incipient faults in aircraft acceleration a_x.

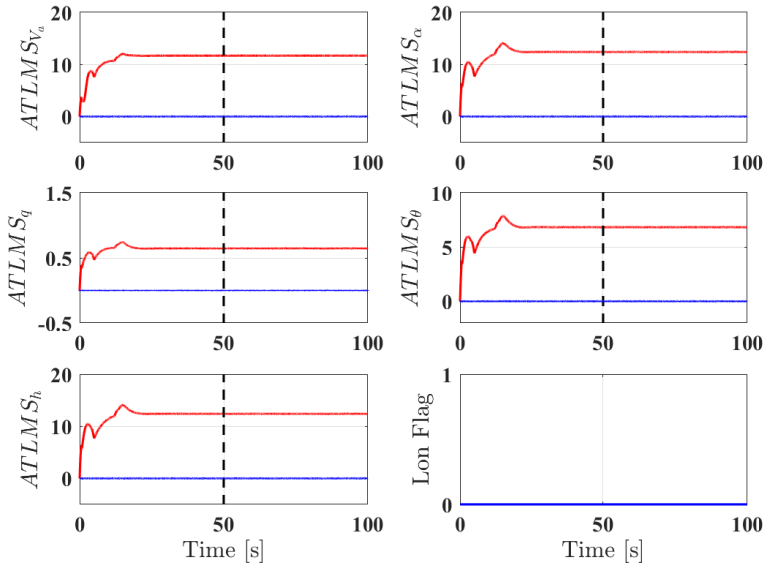

Figure 5.34: Adaptive thresholds (red), insensitive residuals r_0 (blue), and longitudinal fault flag for an incipient fault of slope 0.02 m/s^2 in aircraft acceleration a_x. ATLMS$_i$ refers to the adaptive threshold of measurement $i = V_a$, α, q, θ, h. A fault is detected when ATLMS$_i$ (red) $< r_0$ (blue). In this case, the proposed fault is not detected by the longitudinal adaptive thresholds, causing undesired missed fault alarms.

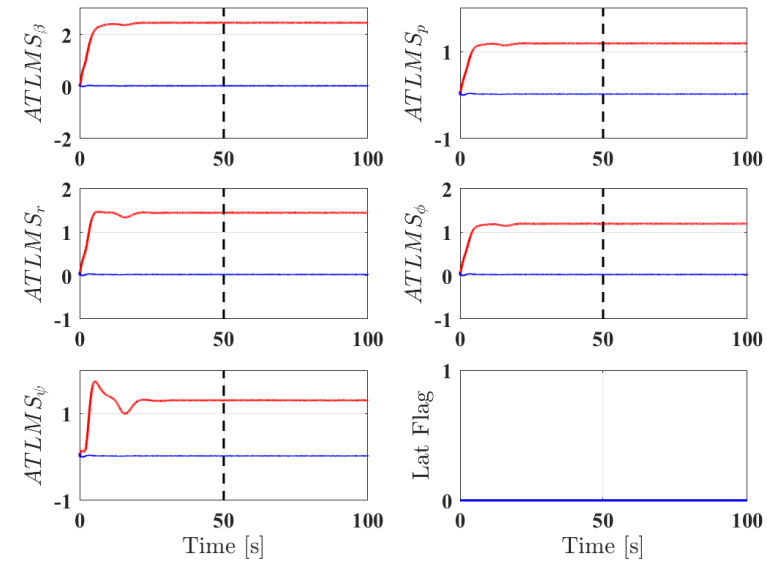

Figure 5.35: Adaptive thresholds (red), insensitive residuals r_0 (blue), and lateral fault flag for an incipient fault of slope 0.02 m/s^2 in aircraft acceleration a_x. ATLMS$_j$ refers to the adaptive threshold of measurement $j = \beta$, p, r, ϕ, ψ. A fault is detected when ATLMS$_j$ $< r_0$. In this case, the proposed fault is not detected by the lateral adaptive thresholds, causing undesired missed fault alarms.

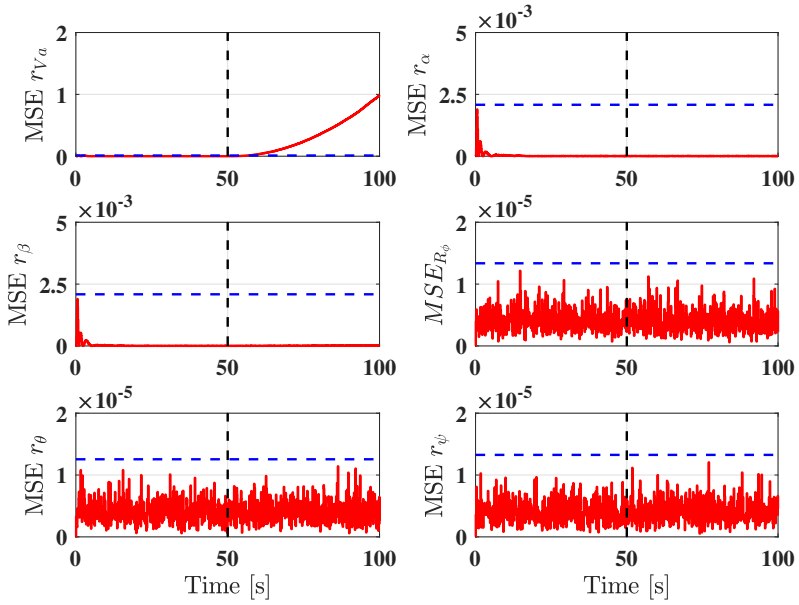

Figure 5.36: Residual mean squared error for EKF-based approach for an incipient fault of amplitude 0.02 m/s^2 in aircraft acceleration a_x. MSE_{r_i} indicates the residual MSE of measurement $i = V_a$, α, β, ϕ, θ, ψ. A fault is detected when any of the decision functions (red) exceeds their respective thresholds (blue). In this case, only the MSE of the airspeed residual (r_{V_a}) is greater than its respective threshold, indicating fault occurrence.

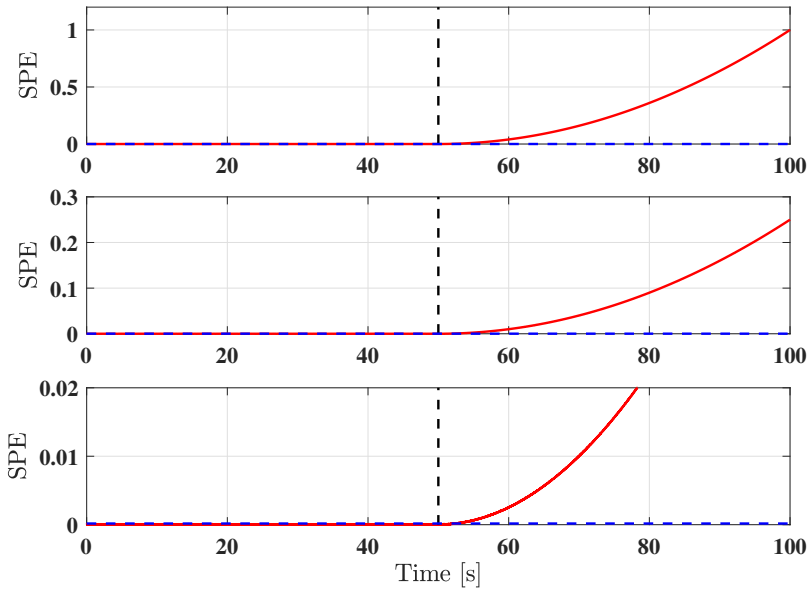

Figure 5.37: Residual squared prediction error for the PCA-based approach regarding incipient faults in aircraft acceleration a_x with slope of 0.02 m/s^2 (top), 0.01 m/s^2 (middle), and 0.005 m/s^2 (bottom). A fault is detected when any of the decision functions (red) exceeds their respective thresholds (blue).

5.2.8 Scenarios 8 and 9: Changing flight conditions

In the next scenarios, it is investigated how planned changes in flight conditions affect the proposed fault detection modules. It is highly recommended that fault detection approaches should be able to distinguish between fault occurrence and nominal changes in flight conditions such as aircraft altitude and velocity updates (table 5.4).

Scenarios 8 and 9 simulate ordinary flight situations and fault detection approaches must not indicate fault alarms. This is the case for KF-ATLMS approach as presented in figures 5.38 and 5.39. Both longitudinal and lateral adaptive thresholds do not cross their respective insensitive residuals.

On the other hand, this is not the case for both the EKF-based (fig. 5.40) and the PCA-based approaches (fig. 5.44, left column, top). They are not able to distinguish between faulty scenarios and changes in flight condition, resulting in undesired false alarm indication. For the EKF-based approach, this behavior is presented in figures 5.40 and 5.43. For the PCA-based approach, this behavior is presented in the left column of figure 5.44 for scenarios 8 (top) and 9 (bottom). As mentioned previously in section 4.4.2, PCA algorithm requires a learning phase with fault-free data. Figure 5.44 (right column) shows an improved PCA model with an adequate learning phase that takes into account usual changes in flight conditions. As a result, the PCA-based approach is able to better distinguish between faults and changes in operating points. Finally, figures 5.41 and 5.42 show the performance of the ATLMS response for scenario 9. The lateral adaptive threshold ATLMS_p (fig. 5.42) correctly detects an abrupt fault in roll rate p while compensating changes in flight conditions.

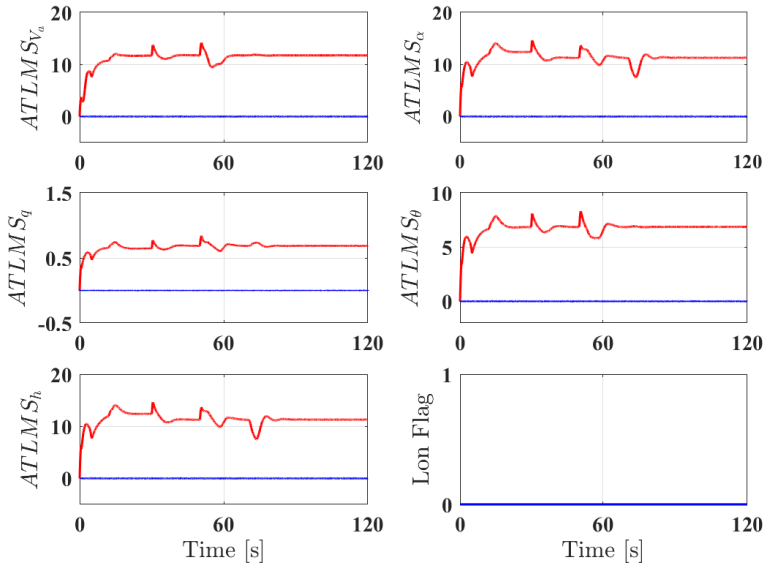

Figure 5.38: Adaptive thresholds (red), insensitive residuals r_0 (blue), and fault flag for longitudinal measurements regarding planned changes in flight conditions (table 5.4, Scenario 8). ATLMS$_i$ refers to the adaptive threshold of measurement $i = V_a$, α, q, θ, h. A fault is detected when ATLMS$_i$ (red) $< r_0$ (blue). As expected, the ATLMS compensates changes in flight conditions. As a result, the longitudinal fault alarm flag is not activated.

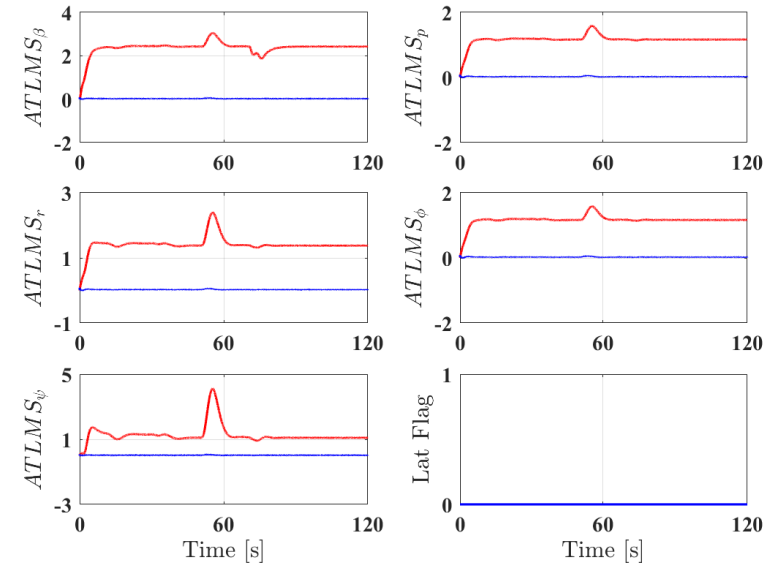

Figure 5.39: Adaptive thresholds (red), insensitive residuals r_0 (blue), and fault flag for lateral measurements regarding planned changes in flight conditions (table 5.4, Scenario 8). ATLMS$_j$ refers to the adaptive threshold of measurement $j = \beta$, p, r, ϕ, ψ. A fault is detected when ATLMS$_j$ (red) $< r_0$ (blue). As expected, the ATLMS compensates changes in flight conditions. As a result, the longitudinal fault alarm flag is not activated.

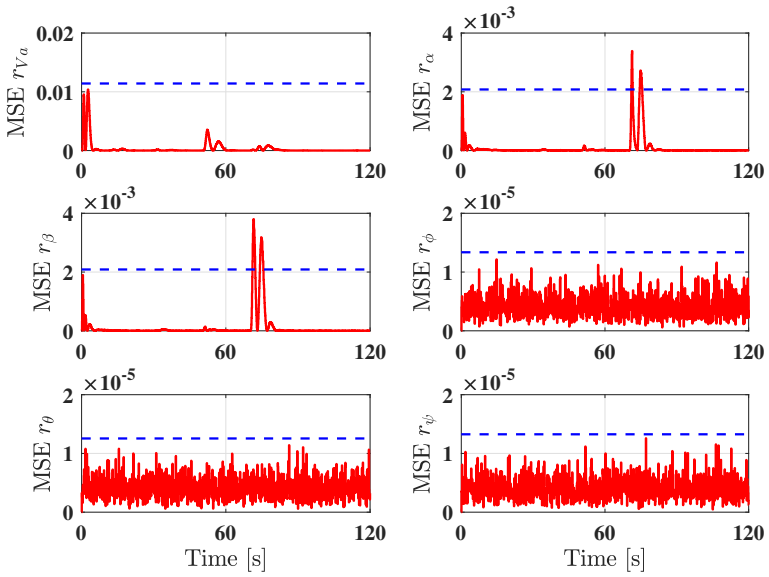

Figure 5.40: Residual mean squared error for EKF-based approach regarding planned changes in flight conditions (table 5.4, Scenario 8). MSE_{r_i} indicates the residual MSE of measurement $i = V_a$, α, β, ϕ, θ, ψ. The decision functions MSE_α and MSE_β cross their respective decision thresholds once the yaw angle ψ is updated at 70s, indicating an undesired false alarm.

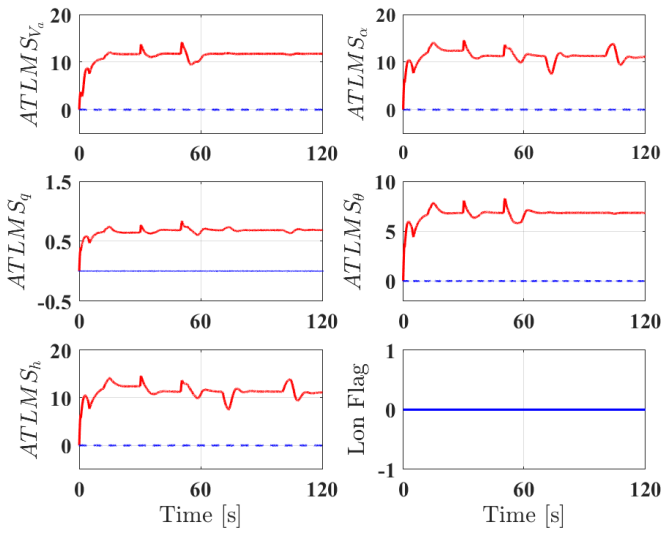

Figure 5.41: Adaptive thresholds (red), insensitive residuals r_0 (blue), and fault flag for longitudinal measurements regarding planned changes in flight conditions (table 5.4, Scenario 9). ATLMS_i refers to the adaptive threshold of measurement $i = V_a$, α, q, θ, h. A fault is detected when ATLMS_i (red) $< r_0$ (blue). As expected, the alarm flag is not activated after fault occurrence at 70s since the applied fault is related to the aircraft lateral dynamics.

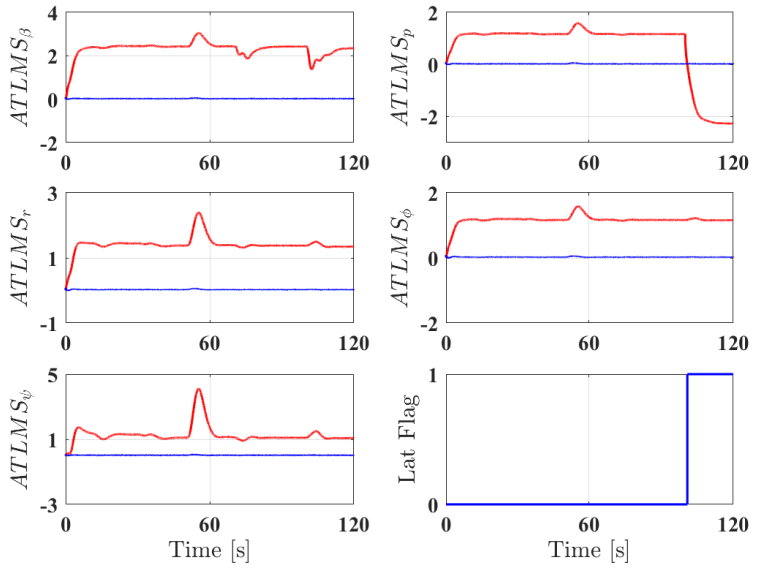

Figure 5.42: Adaptive thresholds (red), insensitive residuals r_0 (blue), and fault flag for lateral measurements regarding planned changes in flight conditions (table 5.4, Scenario 9). ATLMS$_j$ refers to the adaptive threshold of measurement $j = \beta$, p, r, ϕ, ψ. A fault is detected when ATLMS$_j$ (red) $< r_0$ (blue). In this case, a fault is detected when ATLMS$_p$ (red) $< r_0$ (blue) after 70s.

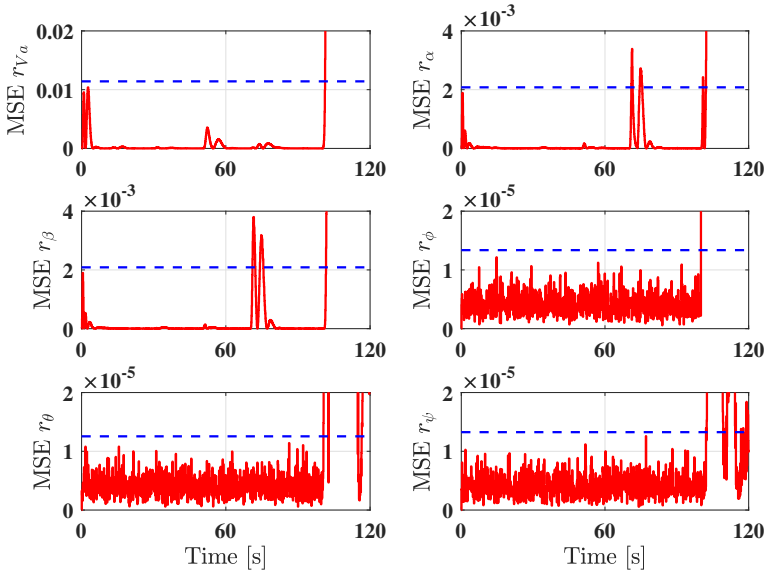

Figure 5.43: Residual mean squared error for EKF-based approach regarding planned changes in flight conditions (table 5.4, Scenario 9). MSE_{r_i} indicates the residual MSE of measurement $i = V_a$, α, β, ϕ, θ, ψ. The decision functions MSE$_\alpha$ and MSE$_\beta$ cross their respective decision thresholds once the yaw angle ψ is updated at 70s, indicating an undesired false alarm.

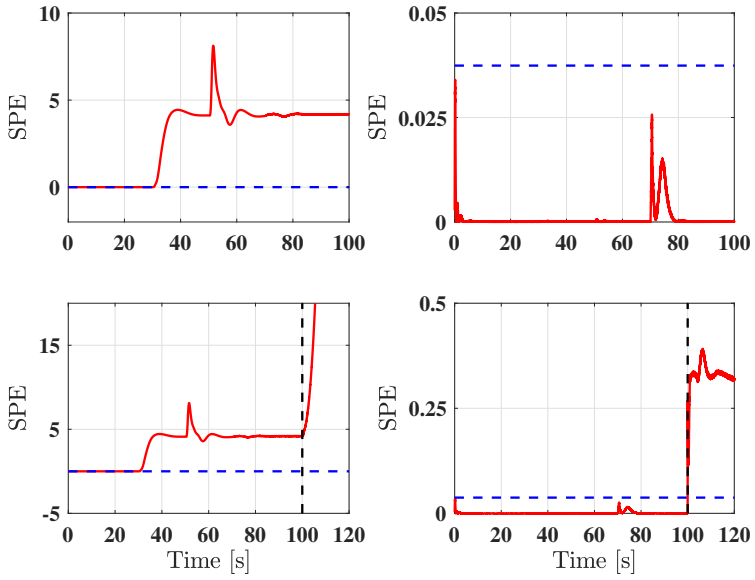

Figure 5.44: Squared prediction error for PCA-based approach regarding scenarios 8 (top) and 9 (bottom). On the left column, the decision function undesirably crosses the thresholds right after changes in flight conditions, causing undesired false alarms. On the right column, an adequate learning phase is applied to PCA algorithm, resulting in an enhanced performance in distinguishing between faults and planned changes in operating conditions.

5.3 Fault Identification and Isolation Results

For fault isolation (fault location) and identification (fault type and size), both KF-ATLMS and EKF-based approaches use a decision logic based on the activation sequence of the alarm flags.

As discussed in chapter 4, the Alarm Flag Activation Sequence (AFAS) metrics indicates which alarm flags have been activated and the sequence of their activation. As a consequence, different faults produce different flag activation sequences.

For the sake of terminology simplification, table 5.5 presents the alarm flag labels used. Therefore, AF_0 indicates no fault, AF_A indicates that the alarm flag associated with the angle of attack α was activated, and AF_{FT} indicates that the alarm flag associated with roll angle ϕ, AF_F, was first activated, followed by the activation of the alarm flag associated with pitch angle θ, AF_T. The patterns formed by the different sequences of fault alarms provide useful information regarding the

identification and isolation of proposed faults.

Table 5.5: Alarm Flag (AF) Captions: AF_i indicates that the alarm flag associated with the measurement i was activated. V_a is the aircraft airspeed, α and β are the angle of attack and sideslip angle, respectively; p, q, and r are the aircraft angular rates; ϕ, θ, ψ are the aircraft attitude angles; and h is the aircraft altitude.

Measurement	V_a	α	β	p	q	r	ϕ	θ	ψ	h	No Fault
Alarm Flag	AF_V	AF_A	AF_B	AF_P	AF_Q	AF_R	AF_F	AF_T	AF_S	AF_H	AF_0

Due to the decoupling nature of longitudinal and lateral linear models, the AFAS for the KF-ATLMS fault detection approach can be clearly split into two parts, resulting in a convenient aspect for fault isolation.

Diagnosis results for an abrupt fault in pitch rate q (fig. 5.45, top-left), for example, show that the longitudinal alarm flag AF_Q associated with pitch rate was active and alarm flags associated with lateral measurements were not. A similar analysis can be made regarding abrupt and incipient faults in roll angle p (fig. 5.45, bottom-left and bottom-right). Although the dynamic decoupling is a useful feature for fault isolation, further residual analysis is also required in order to distinguish between different types of faults.

The AFAS for the EKF-based approach (fig. 5.46) could be also used to indicate the type of a fault as it provides different flag patterns for different faulty scenarios. Taking scenario 2 and 4 with abrupt faults in pitch rate q and roll rate p (fig. 5.46, top-left), it is possible to analyze how AFAS behaves as fault amplitude increases. For abrupt faults in pitch rate q with amplitudes between 0.1 and 0.22 rad/s, for example, the respective AFAS is AF_{TAVSF} while faults with higher amplitudes present a steady AFAS of AF_{TAVSFB}. Further residual analysis is required for fault isolation as well as to distinguish between abrupt and incipient faults in aircraft acceleration a_x measurements since different types of fault provide the same flag sequence (AF_V).

Differently from the AFAS method, the contributions to the squared prediction error provides useful information to distinguish the size of different faults as well as its location. In figure 5.47, for example, it is possible to investigate the severity of a fault in pitch rate q by comparing the contributions to SPE. Figure 5.47 (top) indicates a higher contribution of the pitch rate residual to SPE in scenario 2 with a fault amplitude of 0.5 rad/s when compared to the SPE contributions with smaller fault amplitudes (fig. 5.47, middle and bottom). The higher the contribution the more severe is the fault. Although the contribution plot is a useful tool for fault isolation, further residual analysis is also required in order to distinguish between different types of faults. Figures 5.47 - 5.52 provide the contributions to SPE for all simulated scenarios presented in table 5.3.

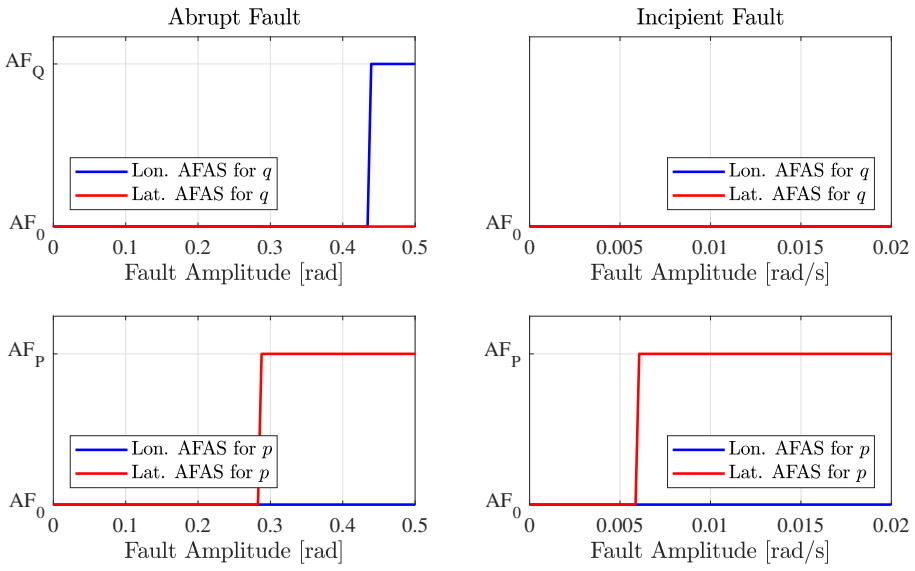

Figure 5.45: Alarm Flag Activation Sequence (AFAS) for ATLMS-based approach regarding abrupt and incipient faults in roll rate p and pitch rate q regarding scenario 2 (top, left), scenario 3 (top, right), scenario 4 (bottom, left), and scenario 5 (bottom, right) as presented in table 5.3.

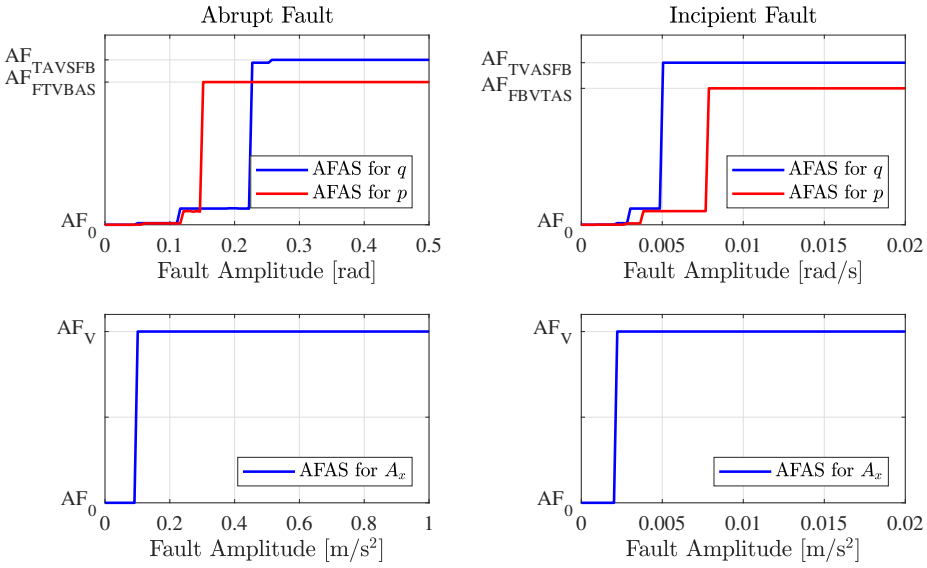

Figure 5.46: Alarm Flag Activation Sequence (AFAS) for kinematic-based approach regarding abrupt and incipient faults in roll rate p, pitch rate q and aircraft acceleration a_x regarding scenario 2 and 4 (top, left), scenario 3 and 5 (top, right), scenario 6 (bottom, left), and scenario 7 (bottom, right) as presented in table 5.3.

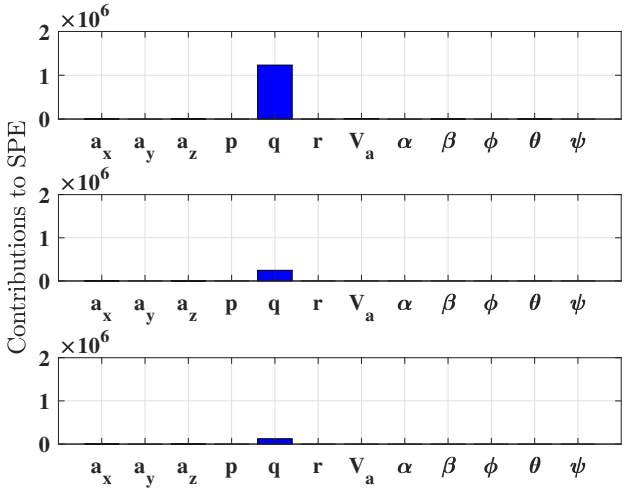

Figure 5.47: Contributions to SPE for an abrupt fault in pitch rate q with amplitude of 0.5 rad/s (top), 0.1 rad/s (middle), and 0.05 rad/s (bottom). a_x, a_y, a_z are the aircraft accelerations; p, q r refers to the aircraft angular rates; ϕ, θ ψ are the aircraft attitude angles; and V_a, α, β refer to the airspeed, angle of attack and sideslip angle, respectively. The higher the contribution of variable q to the SPE, the greater the fault amplitude affecting q.

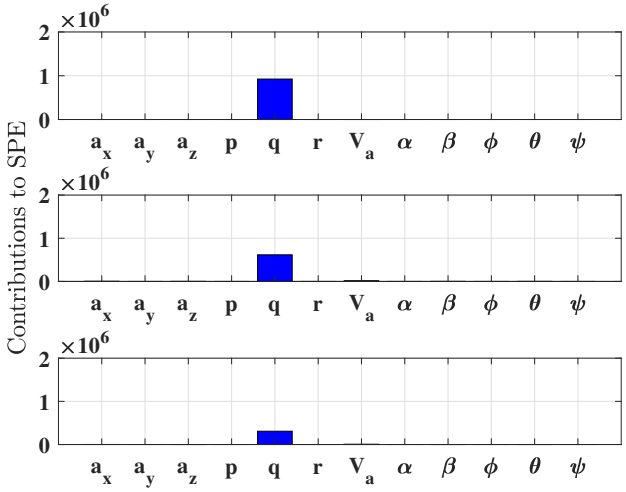

Figure 5.48: Contributions to SPE for an incipient fault in pitch rate q with an amplitude of 0.02 rad/s (top), 0.01 rad/s (middle), and 0.005 rad/s (bottom). a_x, a_y, a_z are the aircraft accelerations; p, q r refers to the aircraft angular rates; ϕ, θ ψ are the aircraft attitude angles; and V_a, α, β refer to the airspeed, angle of attack and sideslip angle, respectively. The higher the contribution of variable q to the SPE, the greater the fault slope affecting q.

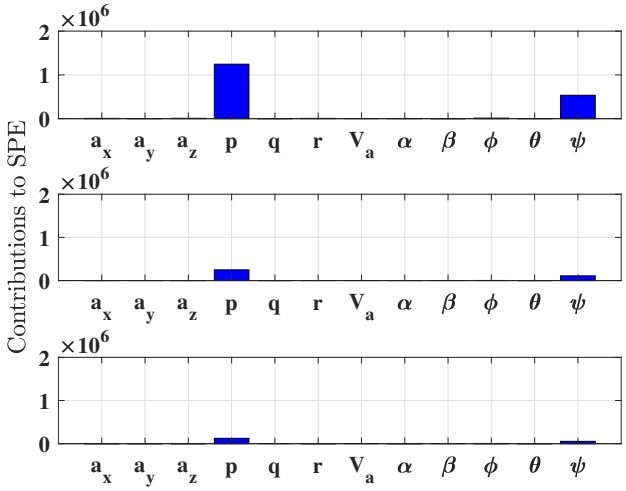

Figure 5.49: Contributions to SPE for an abrupt fault in roll rate p with amplitude of 0.5 rad/s (top), 0.1 rad/s (middle), and 0.05 rad/s (bottom). a_x, a_y, a_z are the aircraft accelerations; p, q r refers to the aircraft angular rates; ϕ, θ ψ are the aircraft attitude angles; and V_a, α, β refer to the airspeed, angle of attack and sideslip angle, respectively. The higher the contribution of variable p to the SPE, the greater the fault amplitude affecting p.

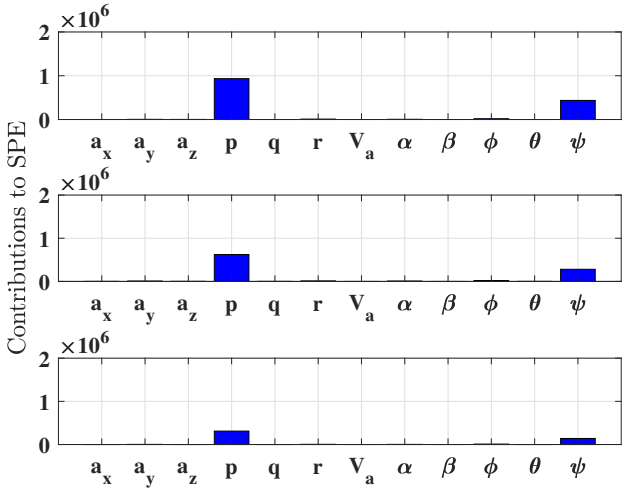

Figure 5.50: Contributions to SPE for an incipient fault in roll rate p with slope of 0.02 rad/s (top), 0.01 rad/s (middle), and 0.005 rad/s (bottom). a_x, a_y, a_z are the aircraft accelerations; p, q r refers to the aircraft angular rates; ϕ, θ ψ are the aircraft attitude angles; and V_a, α, β refer to the airspeed, angle of attack and sideslip angle, respectively. The higher the contribution of variable p to the SPE, the greater the fault slope affecting p.

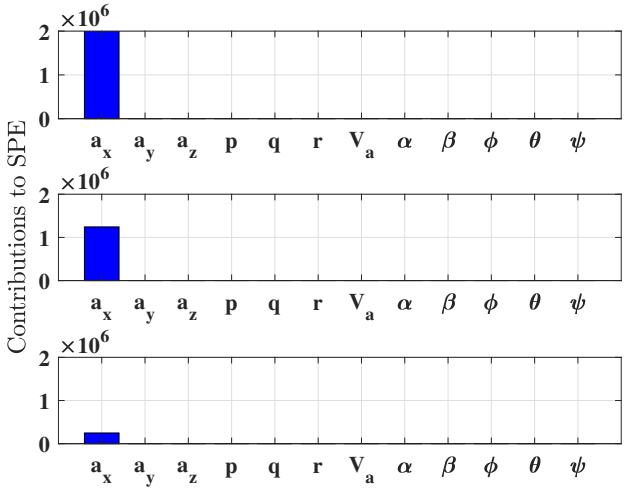

Figure 5.51: Contributions to SPE for an abrupt fault in aircraft acceleration a_x with amplitude of 1 m/s^2 (top), 0.5 m/s^2 (middle), and 0.1 m/s^2 (bottom). a_x, a_y, a_z are the aircraft accelerations; p, q r refers to the aircraft angular rates; ϕ, θ ψ are the aircraft attitude angles; and V_a, α, β refer to the airspeed, angle of attack and sideslip angle, respectively. The higher the contribution of variable a_x to the SPE, the greater the fault amplitude affecting a_x.

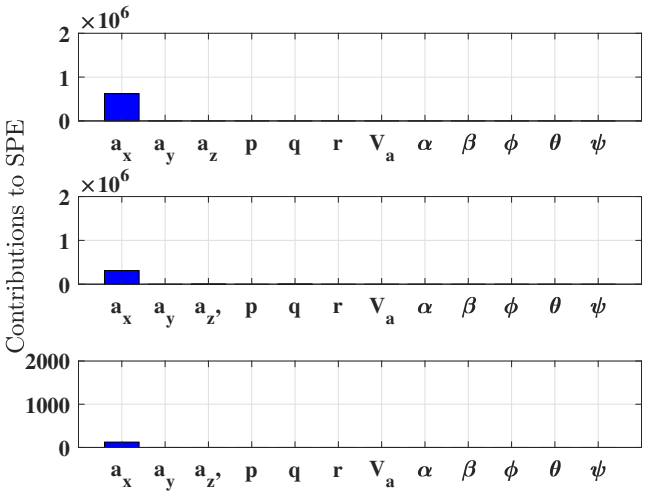

Figure 5.52: Contributions to SPE for an incipient fault in aircraft acceleration a_x with slope of 0.02 m/s^2 (top), 0.01 m/s^2 (middle), and 0.005 m/s^2 (bottom). a_x, a_y, a_z are the aircraft accelerations; p, q r refers to the aircraft angular rates; ϕ, θ ψ are the aircraft attitude angles; and V_a, α, β refer to the airspeed, angle of attack and sideslip angle, respectively. The higher the contribution of variable a_x to the SPE, the greater the fault slope affecting a_x.

5.4 Comparison of Fault Detection Approaches

As exposed in [4], the comparison of different methods for fault detection depends on many aspects such as type of processes, type of disturbances, nonlinearities, proper fault modelling, professional expertise, etc. Major advantages and drawbacks of each approach are presented in table 5.6.

In general, all three proposed approaches rely on the low complexity decision function algorithms for real-time implementation, such as the log-likelihood ratio, mean-squared error (MSE) and squared prediction error (SPE). Regarding the KF-ATLMS approach, the most important advantage relies on the possibility of tuning well-known parameters in the adaptive threshold algorithm (ATLMS). This is a convenient feature for distinguishing between normal flight changes and fault occurrence, reducing the number of false alarms. A brief discussion of ATLMS parameter tuning is presented in appendix E. On the other hand, the KF-ATLMS

approach is aircraft-specific once it relies on the extraction of appropriate linear models. This is a major drawback since linear model development requires the key assumption of small range operation for the model to be valid. Besides that, it is necessary to deal with model uncertainties. Inaccurate linear model parameters may lead to a reduction of the sensitivity of the fault detection module in the presence of small faults, resulting in missed fault alarms.

This is not the case for the EKF-based approach, for example. A major advantage of such approach is that the kinematic model is well defined for the whole operation range and could be used for other fixed-wing aircrafts. This is a desirable feature for system integration purposes. On the other hand, attention must be paid to model nonlinearities. Based on simulation results, a major drawback of this approach is its sensitivity to changes in operation points. A possible solution for that is setting threshold values conveniently high in order to avoid false alarms at the cost of reducing the sensitivity to small amplitude faults.

The major disadvantages of the PCA-based approach are the adequate selection of principal components in the PCA method and the need for suitable algorithm data training (learning phase). Underextraction of principal components causes the elimination of important process information while overextraction may result in misleading interpretation of spurious components. Also, poor data training can lead to misinterpretation of detection results and inaccuracies in distinguishing between changes in operating conditions and fault occurrence. On the other hand, this approach could be used for other aircrafts once it does not require aircraft models.

5.5 EKF-ATLMS Approach: Fault Detection and Diagnosis Results

In view of the comparison of major advantages and drawbacks in section 5.4, a novel fault detection and diagnosis approach is proposed in order to cope with the main disadvantages of the previous approaches and also to exploit their benefits as

Table 5.6: Advantages and Drawbacks regarding the Development of the Proposed Fault Detection Approaches

The KF-ATLMS approach	
	Advantages - Low complexity algorithms for real-time applications; - Tuning of well-known parameters; **Drawbacks** - Rely on appropriate linear models; - Aircraft-specific;
The EKF-based approach	
	Advantages - Well-defined aircraft model; - Could be used for other fixed-wing aircrafts; **Drawbacks** - Deal with model nonlinearities; - Sensitive to changes in operation points;
The PCA-based approach	
	Advantages - Do not need the aircraft model; - Could be used for any fixed-wing aircrafts; - Low complexity algorithm for real-time applications; **Drawbacks** - Possible over/under extraction of data features; - Requires well-defined operation points; - Requires algorithm training

presented in section 4.5.

A simulation campaign is performed in order to analyze the behavior of the EKF-ATLMS approach under different flight circumstances, as provided in table 5.7. Additional results of the EKF-ATLMS fault detection and diagnosis approach is presented in Appendix G. Figure 5.53 presents the adaptive threshold responses regarding 100 different fault-free scenarios with planned changes in flight conditions

(table 5.7). As expected, no false alarm is activated during fault-free simulation campaign. This is a highly desirable characteristic for further integration to the aircraft system.

Table 5.7: Guidelines for simulation campaign.

Number of Simulations	100
Initial desired V_a	random integer between 15 and 21 m/s
Initial desired h	random integer between 500 and 1500 m
Initial desired ψ	random integer between 138° and 160°
Changing Desired Flight Conditions (V_a, h, ψ)	random time instant between 30 and 80 s (cruise flight) with random integer values for V_a, h, and ψ as defined above
Fault occurrence	50 s
Abrupt fault amplitude in q	linearly spaced values between 0.05 and 0.5 rad/s
Drift fault amplitude in q	linearly spaced values between 0.005 and 0.02 rad/s
Abrupt fault amplitude in p	linearly spaced values between 0.1 and 0.5 rad/s
Drift fault amplitude in p	linearly spaced values between 0.005 and 0.02 rad/s
Abrupt fault amplitude in a_x	linearly spaced values between 0.2 and 1 m/s^2
Drift fault amplitude in a_x	linearly spaced values between 0.005 and 0.02 m/s^2

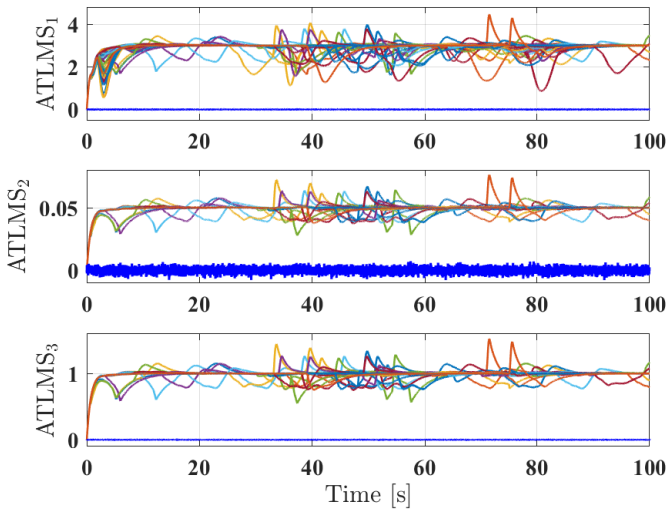

Figure 5.53: Adaptive threshold responses for the EKF-ATLMS approach regarding fault-free simulation campaign.

Figures 5.54 and 5.55 show the adaptive threshold response regarding abrupt and incipient faults in pitch rate q (table 5.7) during simulation campaign. Also, a fault (abrupt or incipient) in pitch rate produces the following adaptive threshold

sign pattern ($- - +$, table 5.8), which significantly contributes for fault diagnosis purposes. In this case, the negative sign ($-$) indicates that $\text{ATLMS}_1 < r_\psi$ and $\text{ATLMS}_2 < r_\phi$ after fault occurrence. On the other hand, the positive sign ($+$) indicates that $\text{ATLMS}_3 > r_\theta$ after fault occurrence (figs. 5.54 and 5.55).

A similar analysis can be done in other fault scenarios. Finally, figures 5.56 - 5.59 show the adaptive threshold response regarding abrupt and incipient faults in roll rate p and aircraft acceleration a_x during simulation campaign according to table 5.7.

Table 5.8: Isolation patterns for faults in roll rate p, pitch rate q, and aircraft acceleration a_x.

	Adaptive Threshold Sign Patterns					
	r_0	r_1	Faults in p	Faults in q	Faults in a_x	No Fault
ATLMS_1	r_ψ	r_{V_a}	$-$	$-$	$-$	$+$
ATLMS_2	r_ϕ	r_θ	$+$	$-$	$+$	$+$
ATLMS_3	r_θ	r_ϕ	$-$	$+$	$+$	$+$

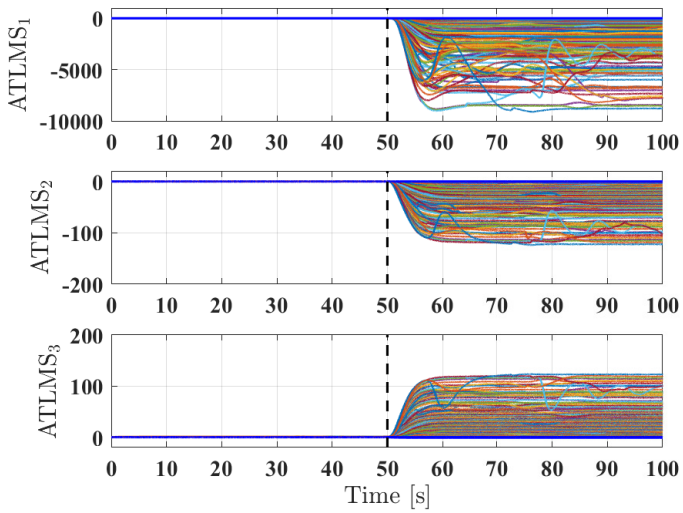

Figure 5.54: Adaptive threshold responses for the EKF-ATLMS approach regarding abrupt faults in pitch rate q during simulation campaign as defined in table 5.7. After fault occurrence, $\text{ATLMS}_1 < r_\psi$, $\text{ATLMS}_2 < r_\phi$, and $\text{ATLMS}_3 > r_\theta$. This behavior produces the adaptive threshold sign pattern ($-$, $-$, $+$) which can provide useful information for fault diagnosis.

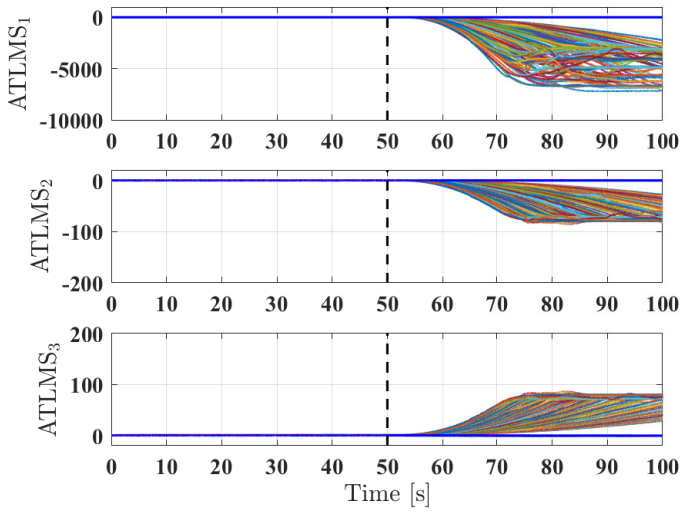

Figure 5.55: Adaptive threshold responses for the EKF-ATLMS approach regarding incipient faults in pitch rate q during simulation campaign as defined in table 5.7. After fault occurrence, $\text{ATLMS}_1 < r_\psi$, $\text{ATLMS}_2 < r_\phi$, and $\text{ATLMS}_3 > r_\theta$. This behavior produces the adaptive threshold sign pattern $(-, -, +)$ which can provide useful information for fault diagnosis.

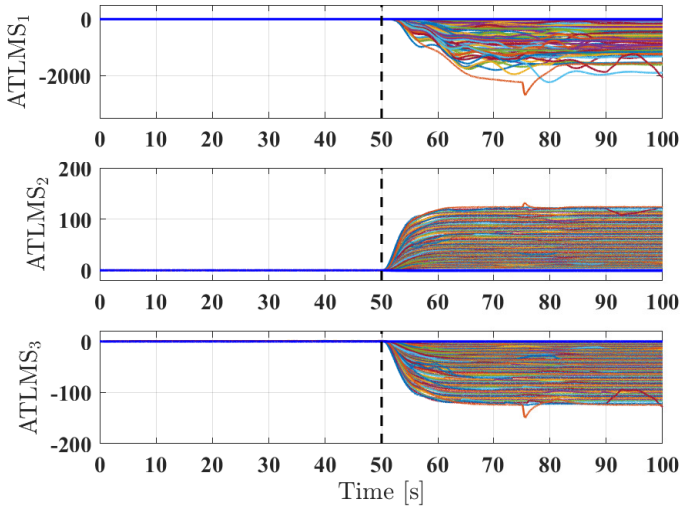

Figure 5.56: Adaptive threshold responses for the EKF-ATLMS approach regarding abrupt faults in roll rate p during simulation campaign as defined in table 5.7. After fault occurrence, $\text{ATLMS}_1 < r_\psi$, $\text{ATLMS}_2 > r_\phi$, and $\text{ATLMS}_3 < r_\theta$. This behavior produces the adaptive threshold sign pattern $(-, +, -)$ which can provide useful information for fault diagnosis.

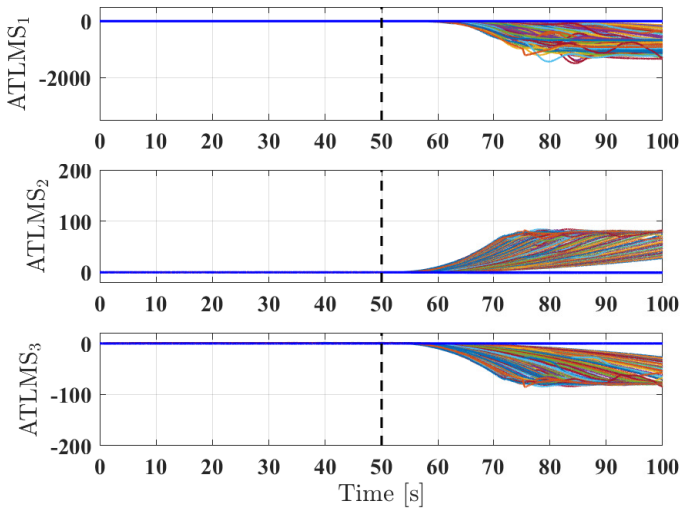

Figure 5.57: Adaptive threshold responses for the EKF-ATLMS approach regarding incipient faults in roll rate p during simulation campaign as defined in table 5.7. After fault occurrence, $\text{ATLMS}_1 < r_\psi$, $\text{ATLMS}_2 > r_\phi$, and $\text{ATLMS}_3 < r_\theta$. This behavior produces the adaptive threshold sign pattern $(-, +, -)$ which can provide useful information for fault diagnosis.

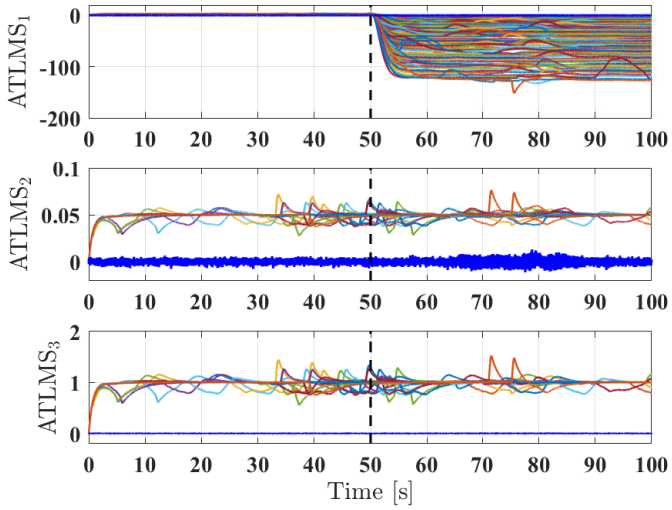

Figure 5.58: Adaptive threshold responses for the EKF-ATLMS approach regarding abrupt faults in aircraft acceleration a_x during simulation campaign as defined in table 5.7. After fault occurrence, $\text{ATLMS}_1 < r_\psi$, $\text{ATLMS}_2 > r_\phi$, and $\text{ATLMS}_3 > r_\theta$. This behavior produces the adaptive threshold sign pattern $(-, +, +)$ which can provide useful information for fault diagnosis.

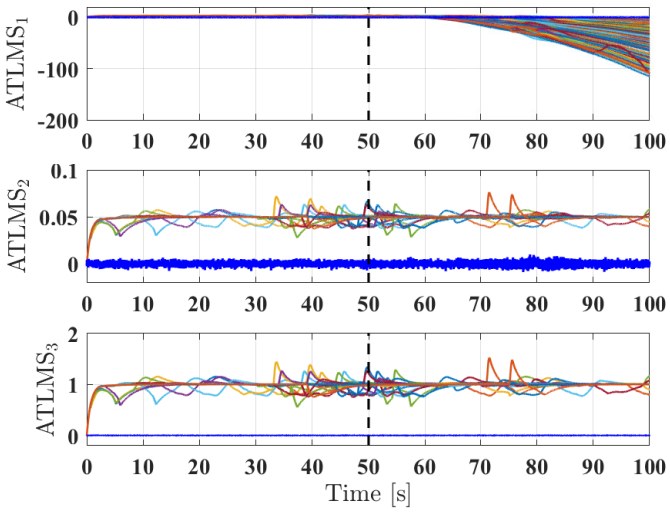

Figure 5.59: Adaptive threshold responses for the EKF-ATLMS approach regarding incipient faults in aircraft acceleration a_x during simulation campaign as defined in table 5.7. After fault occurrence, $\text{ATLMS}_1 < r_\psi$, $\text{ATLMS}_2 > r_\phi$, and $\text{ATLMS}_3 > r_\theta$. This behavior produces the adaptive threshold sign pattern $(-, +, +)$ which can provide useful information for fault diagnosis.

5.6 Summary of Results

The summary of results of the proposed fault detection approaches regarding flight scenarios presented in table 5.3 are provided in figure 5.60. The EKF-ATLMS approach presented satisfactory detection results in all simulation scenarios. Its detection performance is considerably better than the KF-ATLMS Approach and also better than the EKF-based approach regarding fault scenarios 6 and 7.

Table 5.9 presents an overall comparison between the fault detection and diagnosis strategies regarding five different categories (i) detection accuracy, (ii) detection promptness, (iii) changing flight conditions, (iv) fault isolation, (v) Fault Identification;

The category **Detection Accuracy** refers to whether a fault was detected. Since the reconfiguration procedure would not be activated, missed alarms may lead to undesired system response in presence of fault. Simulation results showed that the

KF-ATLMS was not able to detect (alarm missed) small abrupt and/or incipient faults.

Detection Promptness refers to how quickly a fault is detected after its occurrence and it is related to the True Detection Rate metrics (eq. (5.3)). In practice, there will always be a detection delay due to the dynamics of the system itself. Regarding this category, the PCA-based approach presented the best results.

The category **Changing Flight Conditions** indicates if the fault detection system is able to distinguish between unpermitted deviations from normal operation and ordinary changes in flight conditions (e.g. increase aircraft velocity or altitude). Both KF-ATLMS and EKF-ATLMS model approaches presented satisfactory results in this item. If data is not properly trained, the conventional PCA method is not able to determine the difference between fault occurrences and flight condition changes, resulting in false alarms.

As described previously, the category **Fault Isolation** specifies which measurement/sensor provides faulty behavior. Regarding this item, the KF-ATLMS and the EKF-based approaches did not present assertive fault isolation characteristics as the SPE-contribution method from the PCA-based approach and the isolation patterns from the EKF-ATLMS approach.

The last category, **Fault Identification**, specifies the type of the fault and the size/extension of it. The Alarm Flag Activation Sequence (AFAS) method from KF-ATLMS and EKF-based approaches can distinguish between different fault types in some scenarios, but it cannot indicate the severity of a fault. On the other hand, the SPE-contribution method from the PCA-based approach as well as the deflection analysis of the adaptive threshold of the EKF-ATLMS approach provide useful information regarding fault severity. However, further residual analysis is required to indicate fault type (abrupt or incipient) regarding both methods.

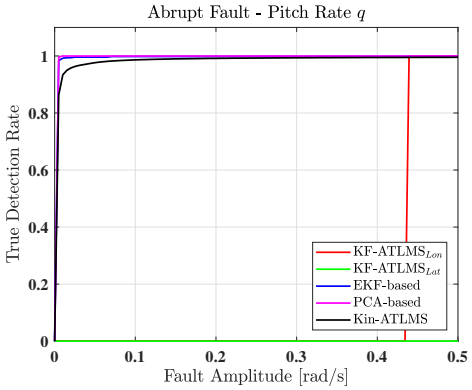

(a) Abrupt fault in pitch rate q

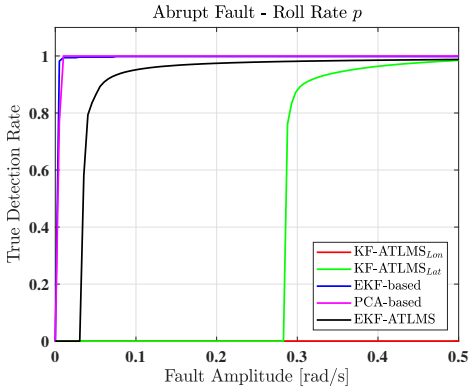

(b) Abrupt fault in roll rate p

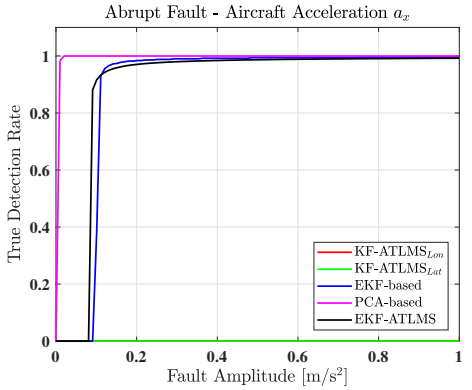

(c) Abrupt fault in aircraft acceleration a_x

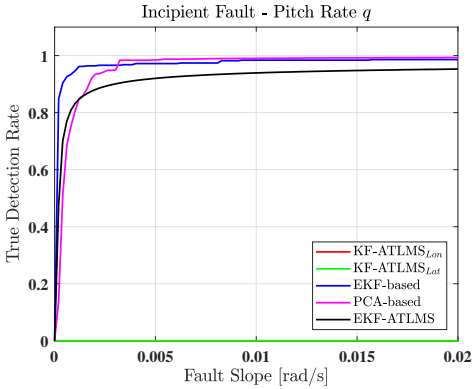

(d) Drift fault in pitch rate q

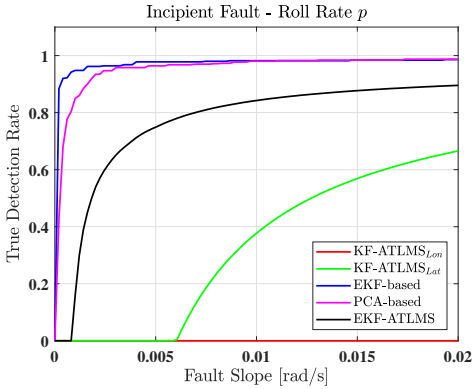

(e) Drift fault in roll rate p

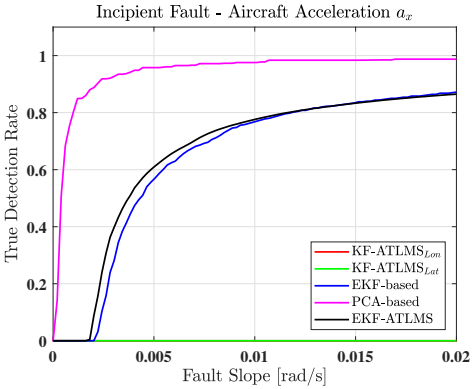

(f) Drift fault in aircraft acceleration a_x

Figure 5.60: Summary of fault detection results and performance of the proposed fault detection methods regarding flight scenarios provided in table 5.3.

Table 5.9: Comparison of fault diagnosis and diagnosis approaches. One star (⋆) indicates very poor performance and five stars represent excellent performance regarding the respective criterion.

	KF-ATLMS Approach	**EKF-based Approach**	**PCA-based Approach**	**EKF-ATLMS Approach**
Detection Accuracy	⋆⋆	⋆⋆⋆⋆⋆	⋆⋆⋆⋆⋆	⋆⋆⋆⋆⋆
Detection Promptness	⋆⋆	⋆⋆⋆⋆	⋆⋆⋆⋆⋆	⋆⋆⋆
Changing Flight Conditions	⋆⋆⋆⋆⋆	⋆	⋆⋆	⋆⋆⋆⋆⋆
Fault Isolation (location)	⋆⋆	⋆⋆	⋆⋆⋆⋆	⋆⋆⋆⋆
Fault Identification (kind, size)	⋆⋆	⋆⋆	⋆⋆⋆	⋆⋆⋆

5.7 Preliminary Flight Experiments

Flight experiments demand enormous technical and logistics efforts to be accomplished. Figure 5.61 shows a nominal flight mission performed on May, 2019 in China. The EKF-based fault detection approach was integrated to the Elektra 2 Solar and flight experiments were carried out regarding a fault-free scenario. Figures 5.62 - 5.64 show the aircraft measurements regarding the aforementioned experiment. Up to this point, no flight experiments with artificial IMU sensor faults were performed.

Figure 5.66 shows EKF-based residuals regarding a flight experiment in normal operation scenario. Most of the residuals are close to zero as expected from a fault-free experiment, except for the yaw angle residual r_ψ. A possible reason for that is the abrupt changes in yaw angle (fig. 5.67) due to the flight maneuvers presented in figure 5.61. As mentioned in section 5.4, residual sensitivity due to changes in flight conditions is an expected drawback of the original kinematic model-based fault detection approach. A possible action to avoid undesired false alarms is to set high threshold values for r_ψ. However, such conservative solution may reduce the sensitivity due to small faults.

For comparison purposes, figure 5.68 shows the results of the EKF-ATLMS approach using the same real flight data set. Differently from the EKF-based approach, the adaptive thresholds compensate for changes in flight conditions and no false alarms are indicated.

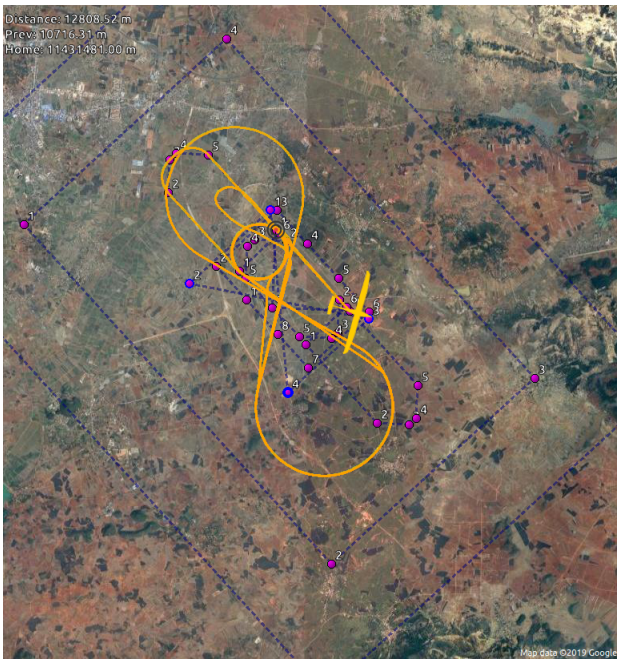

Figure 5.61: Nominal flight experiment of Elektra 2 Solar. (•) indicate flight waypoints.

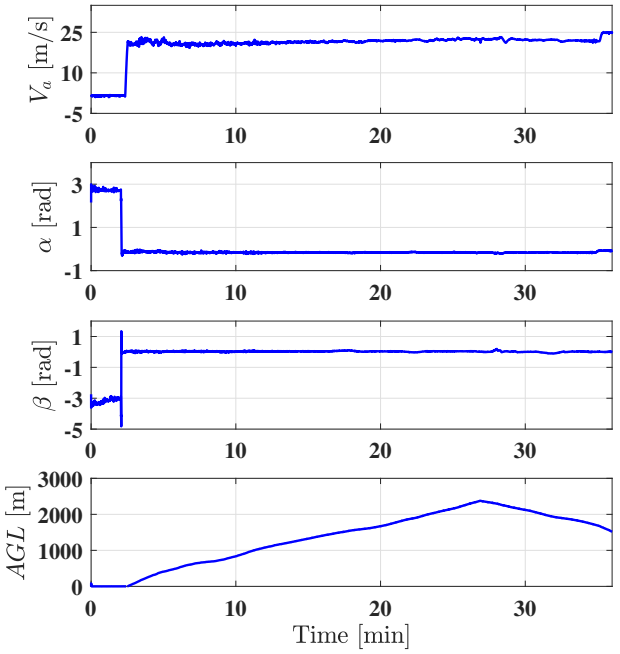

Figure 5.62: Aircraft airspeed V_a, angle of attack α, sideslip angle β, and altitude above ground AGL for a nominal flight experiment of the Elektra 2 Solar.

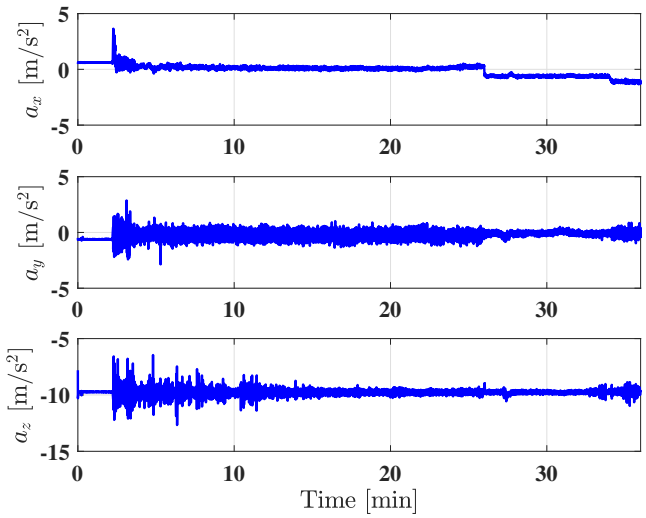

Figure 5.63: Aircraft accelerations for a nominal flight experiment of the Elektra 2 Solar.

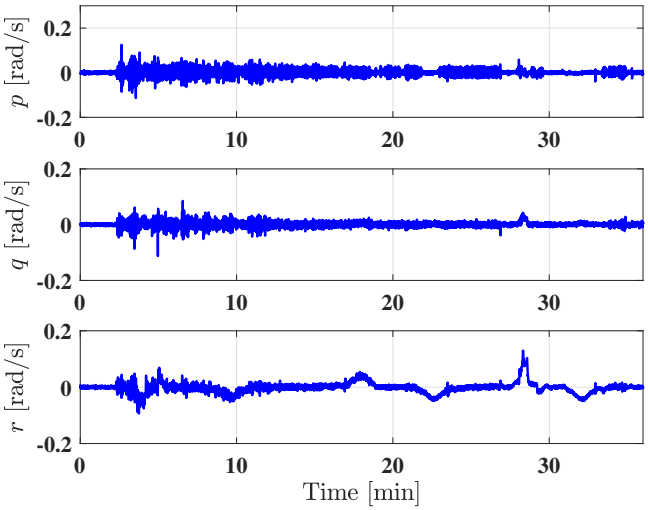

Figure 5.64: Aircraft angular rates for a nominal flight experiment of the Elektra 2 Solar.

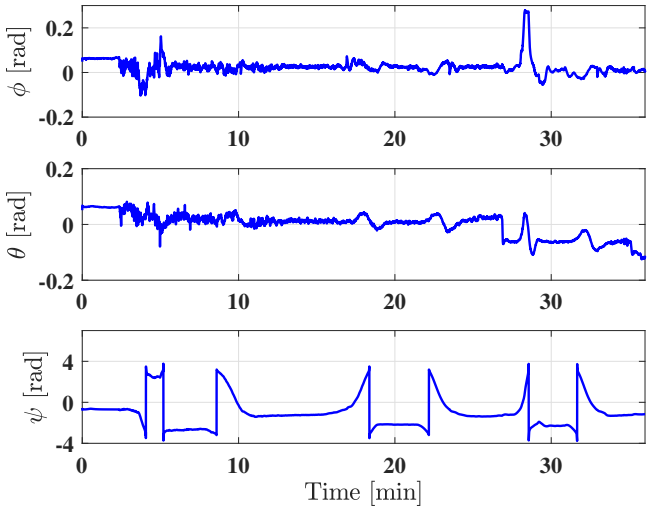

Figure 5.65: Aircraft roll ϕ, pitch θ, and yaw ψ angles for a nominal flight experiment of the Elektra 2 Solar.

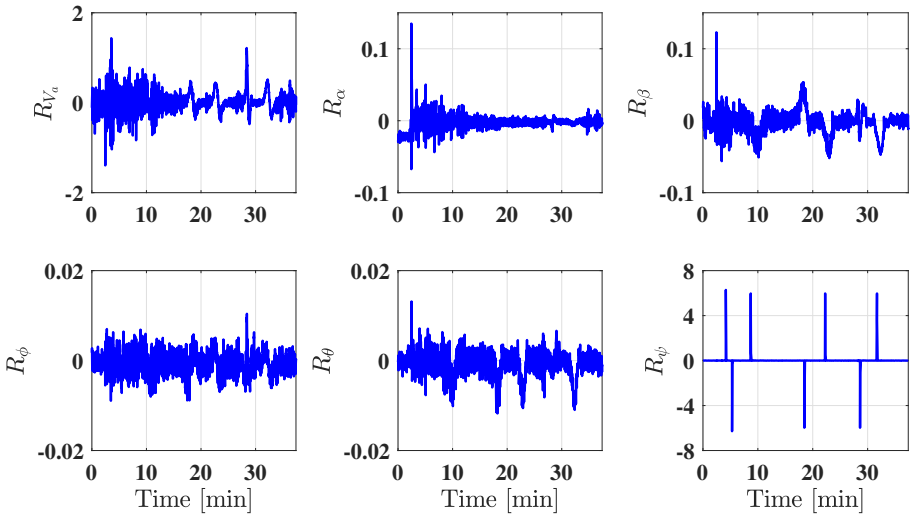

Figure 5.66: Flight experiment in normal operation scenario: residual values for kinematic-model fault detection approach applied to the Elektra 2 Solar aircraft. r_i indicates the residual regarding measurement i.

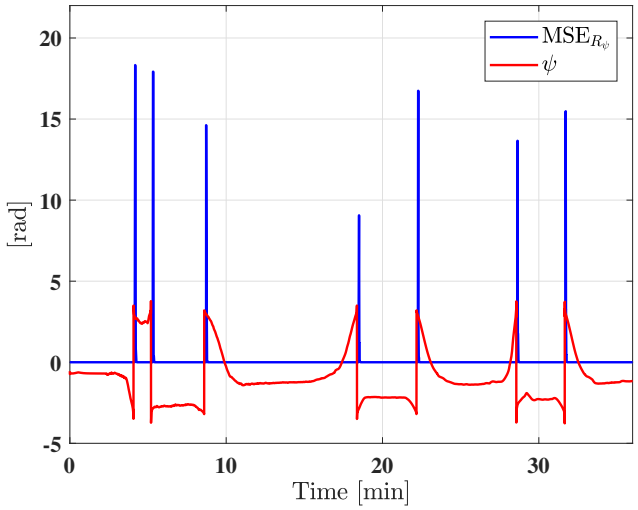

Figure 5.67: Yaw angle ψ measurement and the MSE value of its residual during a fault-free flight experiment.

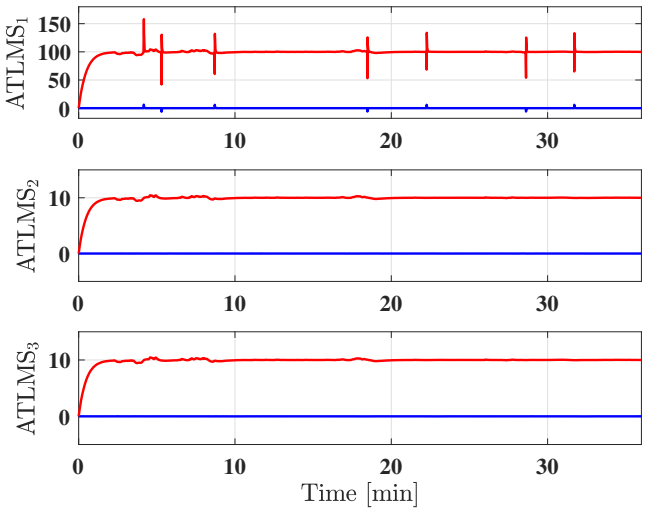

Figure 5.68: Adaptive threshold responses during a fault-free flight experiment regarding the EKF-ATLMS fault detection approach. As expected, no fault alarms are indicated since none of the adaptive thresholds (red) crosses their respective insensitive residuals (blue)

Chapter 6

Conclusion and Future Work

The main contribution of this work was the comparison of suitable IMU sensor fault detection and diagnosis approaches to be used in the Elektra 2 Solar aircraft. In addition to that, a novel fault detection and diagnosis approach was developed.

The KF-ATLMS approach considered aircraft linear models and the design of Kalman filters for residual generation. An adaptive threshold based on the least mean squares filter (ATLMS) was used to detect different types of faults in IMU measurements. One of the major advantages of the ATLMS technique is the possibility - not fully explored in this work - of parameter tuning. This may result in a better fault detection performance. However, the KF-ATLMS approach has presented unsatisfactory detection results for small incipient and abrupt faults. Possible reasons for such behavior may be related to the extraction of suitable linear aircraft models. Besides that, the alarm flag activation sequence provided useful results for fault isolation, but poor results for fault identification.

The second approach, EKF-based approach, considered the nonlinear aircraft kinematic equations and the design of an extended Kalman filter for residual generation. It presented good results regarding fault detection, but it was not able to distinguish between fault occurrence and normal changes in flight conditions. In comparison with the previous approach, the alarm flag activation sequence provided better results.

The third fault detection strategy, the PCA-based approach, presented excellent

results regarding detection promptness and accuracy. However, if not trained properly, the PCA algorithm presents unsatisfactory results in distinguishing between changes in operating conditions and fault occurrence. Residual contributions to squared prediction error (SPE) were used as a fault diagnosis tool and provided relevant results in fault isolation.

In order to minimize the major drawbacks of the three previous fault detection an diagnosis strategies, a fourth approach was developed. Combining the ATLMS algorithm, aircraft kinematic model and the design of an extended Kalman filter for residual generation, the EKF-ATLMS fault detection approach presented satisfactory results regarding detection accuracy and detection promptness. It was also able to distinguish between changes in flight conditions and faults. This is a major desirable attribute for the implementation of a fault detection module in real flights. Another important aspect refers to the usability of the fault detection module in other similar aircrafts. Once the kinematic equations are well defined for fixed-wing aircrafts - which is the case of the aircrafts designed by Elektra Solar - a fault detection approach based on such equations could be easily integrated to other aircraft models.

The EKF-based approach and the EKF-ATLMS strategy were tested with real flight data from a nominal, fault-free flight experiment. The EKF-ATLMS fault detection approach provided significantly better results in dealing with changes in flight conditions while the EKF-based approach showed undesired residual behavior that could lead to false fault alarms.

Based on the comparative performance exposed in table 5.9 and simulations with real flight data, the EKF-ATLMS fault detection approach seems a reasonable choice for further integration to the Elektra 2 Solar.

6.1 Future Work

Many possibilities for advanced studies are on the table, such as

- **Fault Detection and Diagnosis:**
  - Development of strategies for ATLMS parameter tuning;
  - Improve ATLMS MATLAB/Simulink toolbox in order to evaluate signals with different distributions since it currently deals with normal distributed signals only;
  - Improvement of fault diagnosis approaches through further residual statistical analysis;
- **Fault Tolerant Control:**
  - Development of reconfiguration strategies to compensate fault effects in the system so that the stability performance is maintained.
- **Integration and Operation**
  - Integration of the EKF-ATLMS fault detection and diagnosis approach to the aircraft flight management system.
  - Validation of selected the EKF-ATLMS fault detection approach with real faulty flight data.

Bibliography

[1] AIRCRAFT ACCIDENT INVESTIGATION BUREAU OF ETHIOPIA, A. *Aircraft Accident Investigation Preliminary Report - B737-8 (MAX) Registered ET-AVJ*, 2019.

[2] "ELEKTRA SOLAR-Solar-powered aircraft". 2019. Available in: <`https://www.elektra-solar.com/`>.

[3] TECHNOLOGIES, X. *MTi User Manua: MTi 10-series and MTi 100-series 5th generation*, 2018.

[4] ISERMANN, R. *Fault-diagnosis Systems: An Introduction from Fault Detection to Fault Tolerance*. Springer, 2006.

[5] UNMANNED DYNAMICS, L. *AeroSim User's Guide, v.1.2*, 2007.

[6] WISE, B., RICKER, N., KOWALSKI, B. "A theoretical basis for the use of principal component models for monitoring multivariate processes." In: *Process Control and Quality*, v. 1.

[7] GERTLER, J. "Survey of model-based failure detection and isolation in complex plants", *Annual Reviews in Control*, v. 8, pp. 3–11, 1988.

[8] BLANKE, M., KINNAERT, M., LUNZE, J. *Diagnosis and Fault-Tolerant Control*. Springer, 2016.

[9] ZHANG, Y., CHAMSEDDINE, A., RABBATH, C. "Development of advanced FDD and FTC techniques with application to an unmanned quadrotor helicopter testbed". In: *IEEE Transactions on Automatic Control*, v. 45.

[10] HEREDIA, G., OLLERO, A. "Sensor fault detection in small autonomous helicopters using observer/Kalman filter identification". In: *IEEE International Conference on Mechatronics*, 2009.

[11] HANSEN, S., BLANKE, M., ADRIAN, J. "A framework for diagnosis of critical faults in Unmanned Aerial Vehicles". In: *IFAC World Congress on International Federation of Automatic Control*, v. 19.

[12] FREDDI, A., LONGHI, S., MONTERIU, A. "A Model-Based Fault Diagnosis System for Unmanned Aerial Vehicles". In: *IFAC Proceedings*, v. 42.

[13] BATEMAN, F., NOURA, H., OULADSINE, M. "Fault Diagnosis and Fault-Tolerant Control Strategy for the Aerosonde UAV". In: *IEEE Transactions on Aerospace and Electronic Systems*, pp. 2199–2137, 2011.

[14] AVRAM, R., ZHANG, X., CAMPBELL, J., et al. "IMU sensor fault diagnosis and estimation for quadrotor UAVs", *9th IFAC Symposium on Fault Detection, Supervision and Safety for Technical Processes*, v. 28, n. 21, pp. 380–385, 2015.

[15] YOON, S., KIM, S., KIM, Y., et al. "Experimental evaluation of model-free hybrid fault detection and isolation", *AIAA Guidance, Navigation, and Control Conference 2007*, v. 2, pp. 1823–1844, 2007.

[16] MAGRABI, S., GIBBENS, P. "Decentralized fault detection and diagnosis in navigation systems for unmanned aerial vehicles", *IEEE 2000 Position, Location and and Navigation Symposium*, v. 2, pp. 363–370, 2000.

[17] AVRAM, R., ZHANG, X., MUSE, J. "Quadrotor Sensor Fault Diagnosis with Experimental Results". In: *Journal of Intelligent Robotic Systems*, v. 86.

[18] ZHANG, Q.AND XIANG, J., ZHANG. "An active Fault-Tolerant Control method for a low-cost and fixed-wing UAV". In: *2016 IEEE Advanced Information Management, Communicates, Electronic and Automation Control Conference (IMCEC).*

[19] LU, P., VAN KAMPEN, E. "Aircraft inertial measurement unit fault identification with application to real flight data". In: *AIAA Guidance, Navigation, and Control Conference.*

[20] ABBASPOUR, A., YEN, K., NOEI, S., et al. "Detection of Fault Data Injection Attack on UAV Using Adaptive Neural Network", *Complex Adaptive Systems*, v. 95, pp. 193–200, 2016.

[21] ABBASPOUR, A., ABOUTALEBI, P., YEN, K., et al. "Neural adaptive observer-based sensor and actuator fault detection in nonlinear systems: Application in UAV", *ISA Transactions*, v. 67, pp. 317–329, 2017.

[22] SAMY, I., POSTLETHWAITE, I., GU, D.-W. "Detection and accommodation of sensor faults in UAVs - A comparison of NN and EKF based approaches", *49th IEEE Conference on Decision and Control*, pp. 4365–4372, 2010.

[23] BONDYRA, A., GASIOR, P.AND GARDECKI, S. "Fault diagnosis and condition monitoring of UAV rotor using signal processing". In: *2017 Signal Processing: Algorithms, Architectures, Arrangements, and Applications (SPA)*.

[24] CHOW, E., WILLSKY, A. "Analytical redundancy and the design of robust failure detection systems", *IEEE Transactions on Automatic Control*, v. 29, n. 7, pp. 603 – 614, 1984.

[25] PADRAO, P., HSU, L., VILZMANN, M., et al. "Model-based Sensor Fault Detection and Reconfiguration for an Autonomous Solar-powered Aircraft", *Aerospace Technology Congress 2019, FT 2019*, 2019.

[26] PADRAO, P., HSU, L., VILZMANN, M., et al. "A Comparative Study of Sensor Fault Detection Approaches applied to an Autonomous Solar-powered Aircraft", *19^{th} International Conference on Advanced Robotics - ICAR 2019*, 2019.

[27] PADRAO, P., HSU, L., VILZMANN, M., et al. "Kinematic Model-based Sensor Fault Detection and Diagnosis Applied to an Autonomous Solar-Powered Aircraft", *32^{nd} Congress of the International Council of the Aeronautical Sciences - ICAS 2020, accepted for publication*, 2020.

[28] ISERMANN, R., BALLE, P. "Trends in the Application of Model-Based Fault Detection and Diagnosis of Technical Processes". In: *Control Engineering Practice*, pp. 709–719, 1997.

[29] ZHANG, Q., BASSEVILE, M., BENVENISTE. "Early warning of slight changes in systems", *Automatica*, v. 30, pp. 95–113, 1994.

[30] SIMANI, S., FANTUZZI, C., PATTON, R. *Model-based fault diagnosis in dynamic systems using identification techniques*. Springer, 2003.

[31] PATTON, R., FRANK, P., CLARK, R. *Fault diagnosis in dynamic systems: theory and applications*. Prentice Hall, 1989.

[32] FRANK, P. "Fault diagnosis in dynamic systems using analytical and knowledge-based redundancy", *Automatica*, v. 26, pp. 459–474, 1990.

[33] ISERMANN, R. "Process fault detection based on modeling and estimation methods—A survey." *Automatica*, v. 20, pp. 387–404, 1984.

[34] FRANK, P., DING, X. "Survey of robust residual generation and evaluation methods in observer-based fault detection systems." *Journal of Process Control*, v. 7, pp. 403–424, 1997.

[35] ISERMANN, R. "Model-based fault-detection and diagnosis – status and applications", *Annual Reviews in Control*, v. 29, pp. 71–85, 2005.

[36] ISERMANN, R. "Supervision, fault-detection and fault-diagnosis methods — An introduction." *Control Engineering Practice*, v. 5, pp. 639–652, 1997.

[37] BASSEVILLE, M. "Detecting changes in signals and systems—A survey." *Annual Reviews in Control*, v. 24, pp. 309–326, 1988.

[38] FRISK, E., NIELSEN, L. "Robust residual generation for diagnosis including a reference model for residual behavior." *Automatica*, v. 42, pp. 437–445, 2006.

[39] GERTLER, J. "Residual Generation from Principal Component Models for Fault Diagnosis in Linear Systems - Part I: Review of Static Systems". In: *Proceedings of the 2005 IEEE International Symposium on Automation Intelligent Control*, .

[40] FRISK, E. "Residual generation in linear stochastic systems - A polynomial approach". In: *Proceedings of the IEEE Conference on Decision and Control*, v. 3.

[41] GERTLER, J. "Residual generation in model-based fault diagnosis". In: *Proceedings of the 9th IFAC/IFORS Symposium on Identification and Systems Parameter Estimation*, v. 9, .

[42] PATTON, R., C. J. "Observer-based fault detection and isolation: Robustness and applications", *Control Engineering Practice*, v. 5, pp. 671–682, 1997.

[43] NYBERG, M., FRISK, E. "Residual Generation for Fault Diagnosis of Systems Described by Linear Differential-Algebraic Equations". In: *IEEE Transactions on Automatic Control*, v. 51.

[44] GERTLER, J. "Residual Generation from Principal Component Models for Fault Diagnosis in Linear Systems - Part II: Extension to Optimal Residuals and Dynamic Systems". In: *Proceedings of the 2005 IEEE International Symposium on Automation Intelligent Control*, .

[45] PATTON, R., CHEN, J., NIELSEN, S. "Model-based methods for fault diagnosis: some guide-lines". In: *Transactions of the Institute of Measurement and Control*, v. 17.

[46] SAMPATH, M., LAFORTUNE, S., TENEKETZIS, D. "Diagnosability of Discrete-Event Systems." *IEEE Transactions on Automatic Control*, v. 40, 1995.

[47] ZHANG, Y., JIANG, J. "Bibliographical review on reconfigurable fault-tolerant control systems"." *Annual Reviews in Control*, v. 322, 2008.

[48] DING, S. *Model-based fault diagnosis techniques: Design schemes, algorithms, and tools*. Springer, 2008.

[49] RANDAL, W., MCLAIN, T. *Small Unmanned Aircraft Theory and Practice*. Princeton University Press, 2012.

[50] CARVALHO, A. *Fault detection, diagnosis and reconfiguration for optimized design of safe space vehicles applied to the PMM and planetary rovers*. Ph.d. dissertation, Instituto Nacional de Pesquisas Espaciais (INPE), Sao Jose dos Campos, Brazil, 2012.

[51] WALD, A. *Sequential analysis*. Dover Publications, 2004.

[52] WIDROW, B., STEARNS, S. *Adaptive Signal Processing*. Prentice Hall, 1985.

[53] MARZAT, J., PIET-LAHANIER, H., DAMONGEOT, F., et al. "Model-based fault diagnosis for aerospace systems: A survey.v", *Journal of Aerospace Engieering*, v. 226, n. 10, pp. 1329–1360, 2012.

[54] TIEN, D., LIM, K., JUN, L. "Comparative Study of PCA Approaches in Process Monitoring and Fault Detection", 2004.

[55] FRANKLIN, S., GIBSON, D., ROBERTSON, P. "Parallel Analysis: a method for determining significant principal components." In: *Practical Assessment Research and Evaluation*.

[56] LEDESMA, R., VALERO, P. "Determining the Number of Factors to Retain in EFA: An easy-to-use computer program for carrying out Parallel Analysis". In: *Practical Assessment Research and Evaluation*, v. 12.

[57] BARTYS, M., PATTON, R. J., SYFERT, M., et al. "Introduction to the DAMADICS actuator FDI benchmark study", *Control Engineering Practice*, v. 14, n. 6, pp. 577—-596, 2006.

[58] BALMER, G. R. *Modelling and Control of a Fixed-wing UAV for Landings on a Mobile Landing Platform. Dissertation*. Master thesis, Royal Institute of Technology, Stockholm, Sweden, 2015.

[59] PERSSON, L. *Cooperative Control for Landing a Fixed-Wing Unmanned Aerial Vehicle on a Ground Vehicle*. Ph.d. dissertation, Royal Institute of Technology, Stockholm, Sweden, 2016.

[60] NATIONAL IMAGERY MAPPING AGENCY, N. *NIMA Report TR8350.2*, 1984.

[61] CHULLIAT, A., MACMILLAN, S., ALKEN, P., et al. *The US/UK World Magnetic Model for 2015-2020*, 2015.

[62] NATIONAL OCEANIC ATMOSPHERIC ADMINISTRATION, N. *Standard Atmosphere Report, 1976*, 1976.

[63] SIMON, D. *Optimal State Estimation: Kalman, H Infinity, and Nonlinear Approaches*. Wiley, 2006.

[64] FRANGIPANI, V. *Localização Submarina utilizando uma única Referência Acústica via Filtro UKF*. Master thesis, Universidade Federal do Rio de Janeiro (UFRJ), Rio de Janeiro, Brazil, 2015.

Appendix A

Elektra 2 Solar Technical Specifications

Technical Specifications [2]	
Electric Motor	23 kW
Propeller speed for cruise	1250 rpm
Wingspan	24.8 m
Wing Area	27 m^2
Solar Cells	26.5 m^2
Maximum Weight	400 kg
Empty Weight (w/o battery)	160 kg
Battery Weight	120 kg
Maximum Payload	120 kg
Wing Aspect Ratio	23
Maximum Altitude	20 km
Max. glide ratio	≈1:40

Appendix B

Aerodynamic Coefficients for the Elektra Solar Aircraft

B.1 General Parameters

Parameters	Values
m	400 kg
J_x	2909 kg.m^2
J_y	823 kg.m^2
J_z	3718 kg.m^2
J_{xz}	0 kg.m^2
S	27 m^2
b	24.8 m
c	1.0970 m
AR	22.77
e_w	0.9
S_{prop}	2.01 m^2

B.2 Parameters for Lift Coefficient

$$C_L = C_{L_0} + C_{L_\alpha}\alpha + C_{L_{\delta f}}\delta_f + C_{L_{\delta e}}\delta_e + \frac{c}{2V_a}\Big(C_{L_{\dot{\alpha}}}\dot{\alpha} + C_{L_q}q\Big) + C_{L_{Mach}}Mach \quad \text{(B.1)}$$

Parameters	Values
C_{L_0}	0.533
C_{L_α}	5.946
$C_{L_{\delta f}}$	0
$C_{L_{\delta e}}$	0.396
$C_{L_{\dot{\alpha}}}$	0
C_{L_q}	8.366
C_{L_M}	0

B.3 Parameters for Drag Coefficient

$$C_D = C_{D_0} + \frac{(C_L - C_{L_0})^2}{\pi e_w AR} + C_{D_{\delta f}}\delta_f + C_{D_{\delta e}}\delta_e + C_{D_{\delta a}}\delta_a + C_{D_{\delta r}}\delta_r + C_{D_{Mach}}Mach \quad \text{(B.2)}$$

Parameters	Values
C_{D_0}	0.022
$C_{D_{\delta f}}$	0
$C_{D_{\delta e}}$	0.004
$C_{D_{\delta a}}$	0
$C_{D_{\delta r}}$	0
C_{D_M}	0

B.4 Parameters for Side Force Coefficient

$$C_Y = C_{Y_\beta}\beta + C_{Y_{\delta a}}\delta_a + C_{Y_{\delta r}}\delta_r + \frac{b}{2V_a}(C_{Y_p}p + C_{Y_r}r) \tag{B.3}$$

Parameters	Values
C_{Y_β}	-0.185
$C_{Y_{\delta a}}$	-0.038
$C_{Y_{\delta r}}$	0.1
C_{Y_p}	-0.058
C_{Y_r}	0.1

B.5 Parameters for Pitch Moment Coefficient

$$C_m = C_{m_0} + C_{m_\alpha}\alpha + C_{m_{\delta f}}\delta_f + C_{m_{\delta e}}\delta_e + \frac{c}{2V_a}(C_{m_{\dot\alpha}}\dot\alpha + C_{m_q}q) + C_{m_{Mach}}Mach \tag{B.4}$$

Parameters	Values
C_{m_0}	-0.027
C_{m_α}	-1.345
$C_{m_{\delta f}}$	0
$C_{m_{\delta e}}$	-1.677
$C_{m_{\dot\alpha}}$	0
C_{m_q}	-16.895
C_{m_M}	0

B.6 Parameters for Roll Moment Coefficient

$$C_l = C_{l_\beta}\beta + C_{l_{\delta a}}\delta_a + C_{l_{\delta r}}\delta_r + \frac{b}{2V_a}(C_{l_p}p + C_{l_r}r) \tag{B.5}$$

Parameters	**Values (rad)**
C_{l_β}	-0.086
$C_{l_{\delta a}}$	-0.297
$C_{l_{\delta r}}$	0.002
C_{l_p}	-0.724
C_{l_r}	0.211

B.7 Parameters for Yaw Moment Coefficient

$$C_n = C_{n_\beta}\beta + C_{n_{\delta a}}\delta_a + C_{n_{\delta r}}\delta_r + \frac{b}{2V_a}(C_{n_p}p + C_{n_r}r) \tag{B.6}$$

Parameters	**Values (rad)**
C_{n_β}	0.025
$C_{n_{\delta a}}$	-0.001
$C_{n_{\delta r}}$	-0.023
C_{n_p}	-0.071
C_{n_r}	-0.023

Appendix C

MATLAB/Simulink Aircraft Model Description

This section briefly describes the MATLAB/Simulink model of the Elektra 2 aircraft and is based on the works of [58] and [59].

C.1 Simulation Environment

The simulation environment used in this work is MATLAB/Simulink®and the simulation model was built using the AeroSim Blockset [5]. Figure C.1 shows the complete aircraft Simulink model used for simulations. Appendix C describes the aircraft block diagram in more details. A simplified simulation model diagram is presented in figure C.2.

The *Earth Model* provides the local gravitational acceleration and the local Earth radius based on the World Geodetic System 1984 (WGS84) [60]. Besides that, the altitude above mean sea level according to the Earth Gravitational Model 1996 (EGM96 [60]) is also calculated. It also provides the local magnetic field according to the World Magnetic Model [61].

The *Atmosphere Model* provides standard atmosphere data and modelling blocks for background wind, turbulence and wind shear, respectively. It gives the possibility to investigate the effects of turbulence acting on the aircraft, for example.

The *Aerodynamics Model* calculates the aerodynamic coefficients $(C_D, ..., C_n)$ and provides the aerodynamic forces and moments acting on the aircraft $(f_x,\ f_y,\ f_z,\ m_x,\ m_y,\ m_z)$.

The *Propulsion Model* consists of a simplified representation of an electric motor and propeller that relates the motor commands with the resulting propulsion forces and moments. For piston-engine aircrafts - which is not the case here - it also provides the fuel consumption, updating the aircraft mass as the simulation evolves.

The *Inertia Model* provides the moments and products of inertia as well as the position of the center of gravity.

Finally, the *Equations of Motion* are solved by one of the numerical integration techniques provided by MATLAB/Simulink. The calculations of the velocities and angular rates are given in body reference frame. The complete list of measurements provided by the Simulink aircraft model is presented in table C.1.

Table C.1: Simulink Aircraft Model Measurements

Measurement	**Unit**
Position (Lat, Lon, Alt)	rad, rad, m
Ground Speed (v_n, v_e, v_d)	m/s
Body Accelerations (a_x, a_y, a_z)	m/s^2
Angular Rates (p, q, r)	rad/s
Euler Angles (ϕ, θ, ψ)	rad
Magnetic Field (m_{f_x}, m_{f_y}, m_{f_z})	nT
Airspeed (V_a)	m/s
Angle of Attack (α)	rad
Sideslip Angle (β)	rad
Altitude above Ground (AGL)	m
Altitude above Mean-Sea-Level ($AMSL$)	m
Dynamic Pressure	Pa
Static Pressure	Pa
Outside Air Temperature	K

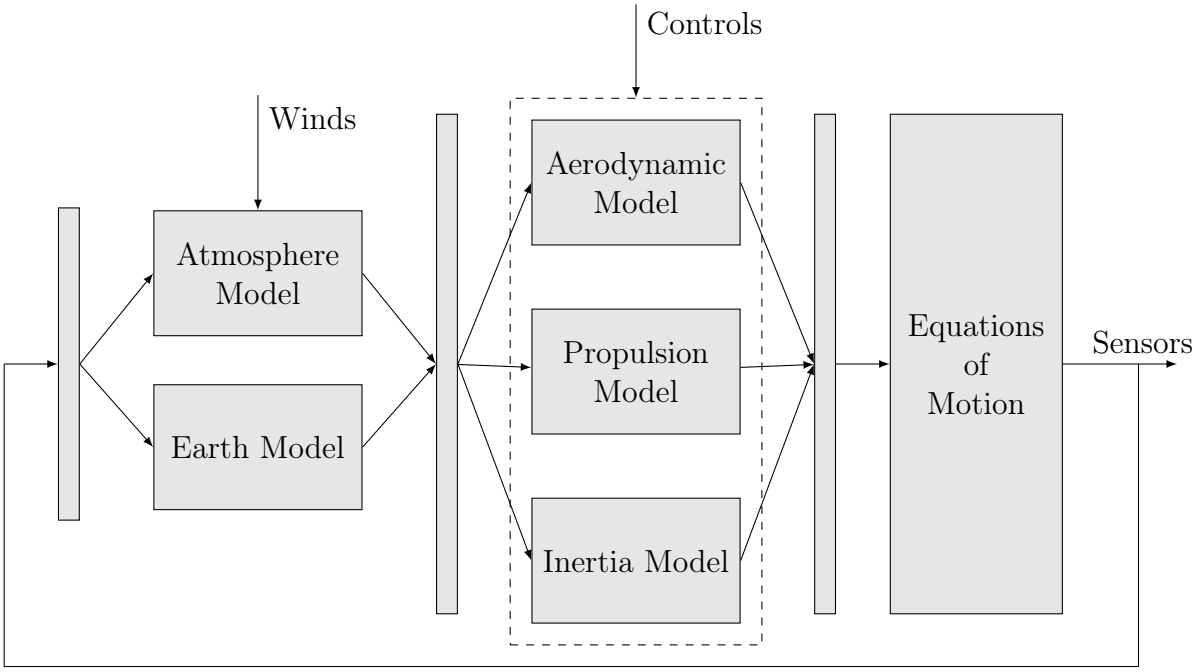

Figure C.2: Simplified Diagram of the Aircraft Simulink Model

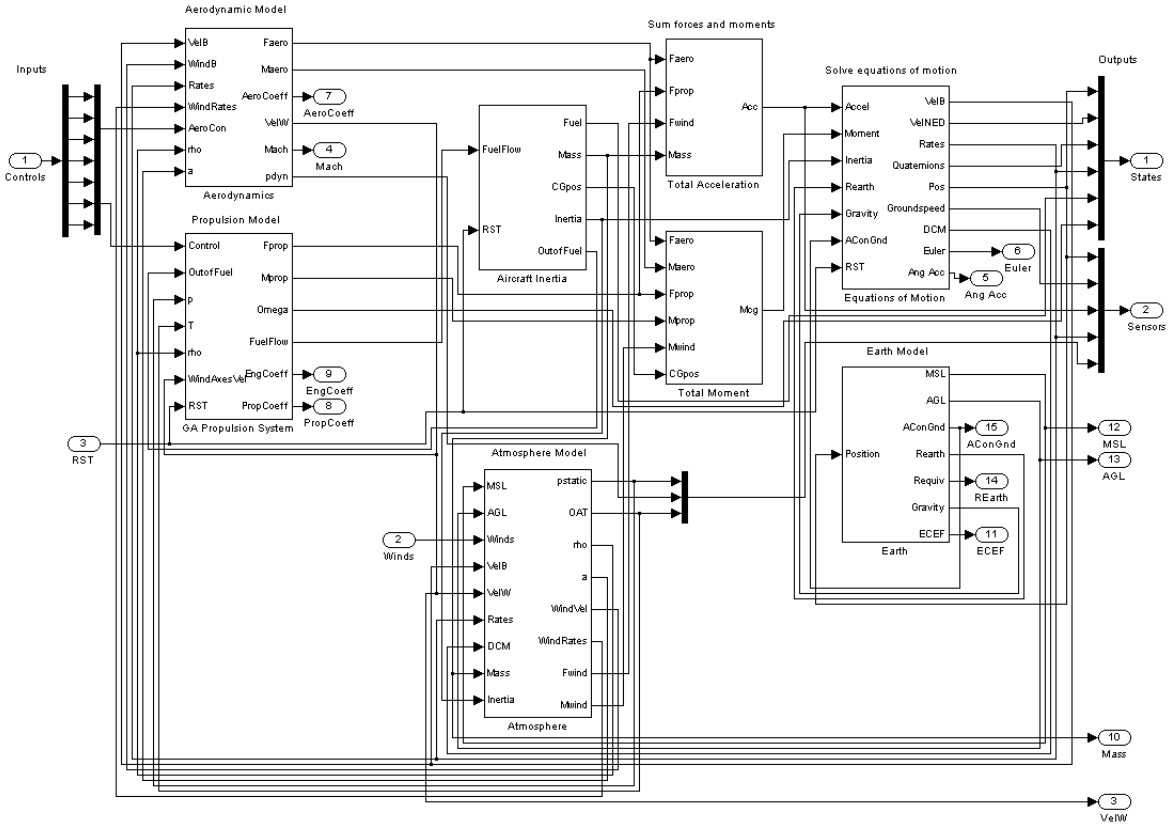

Figure C.1: Complete Aircraft Simulink Model [5]

C.2 Aerodynamics Model Subsystem

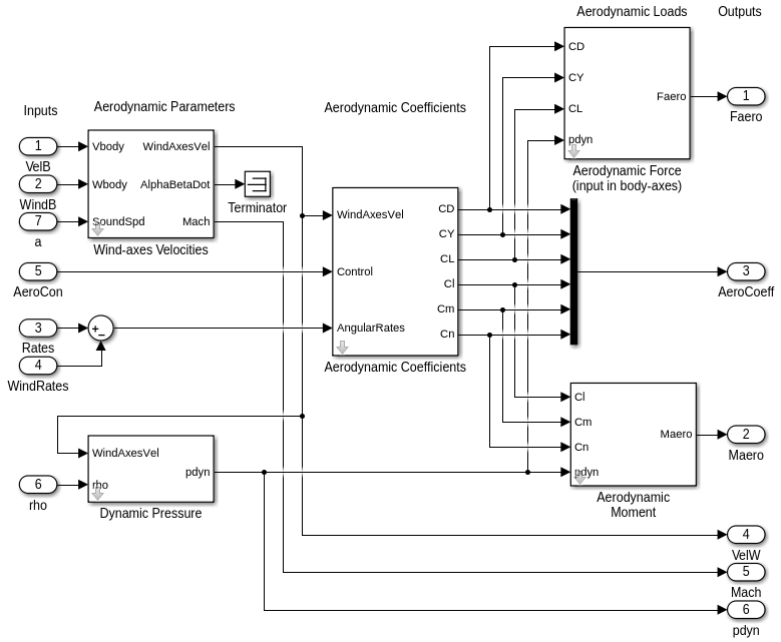

Figure C.3: Simulink Aerodynamics Model: Elektra 2 Solar Aircraft

As shown in figure C.3, the aerodynamics subsystem is composed of five different main blocks, namely: `Wind-axes Velocities`, `Dynamic Pressure`, `Aerodynamic Coefficients`, `Aerodynamic Moments`, and `Aerodynamic Forces`. The resulting forces and moments, expressed in body axes, are the main output of the Aerodynamics subsystem.

C.3 Propulsion Model Subsystem

As shown in figure C.4, the propulsion subsystem is composed of two main blocks, namely: `Electric Motor` and `Fixed-pitch Propeller`. These blocks basically describe the dynamic model of the propeller rotation and the motor. The propeller thrust force and the motor torque are the main outputs of the subsystem.

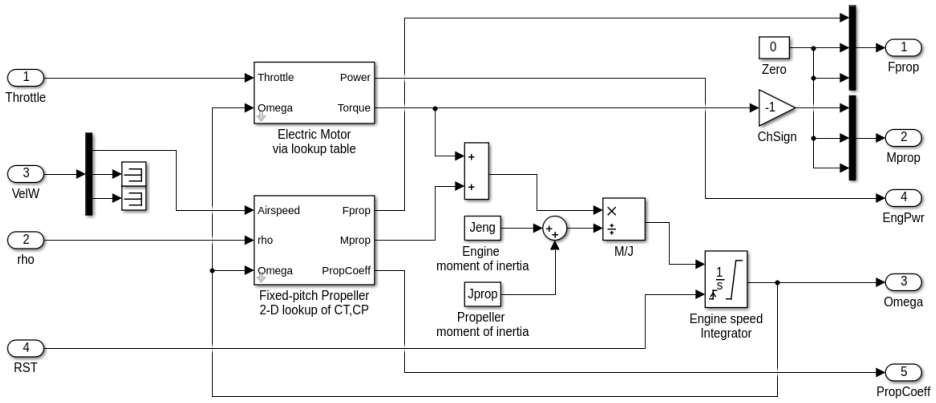

Figure C.4: Simulink Propulsion Model: Elektra 2 Solar Aircraft

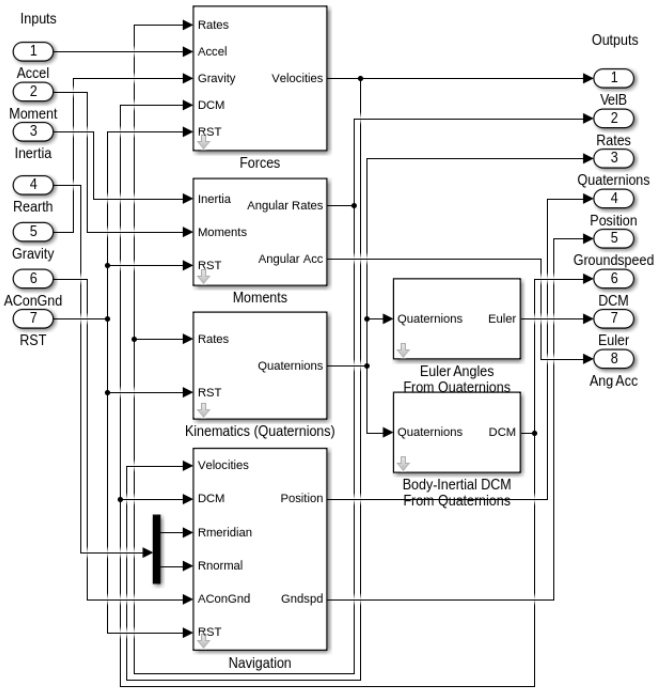

Figure C.5: Simulink Equations of Motion Model: Elektra 2 Solar Aircraft

C.4 Equations of Motion Subsystem

As shown in figure C.5, the EoM subsystem is composed of six main blocks, namely: `Forces`, `Moments`, `Kinematics`, `Navigation`, transformation from quaternions representation to Euler angle, and transformation from quaternions to direction cosine matrix. This subsystem is responsible for grouping the differential equations describing the aircraft motion. The main outputs of the EoM subsystem are the

aircraft velocities, angular rates, attitude and position.

C.5 Earth Model

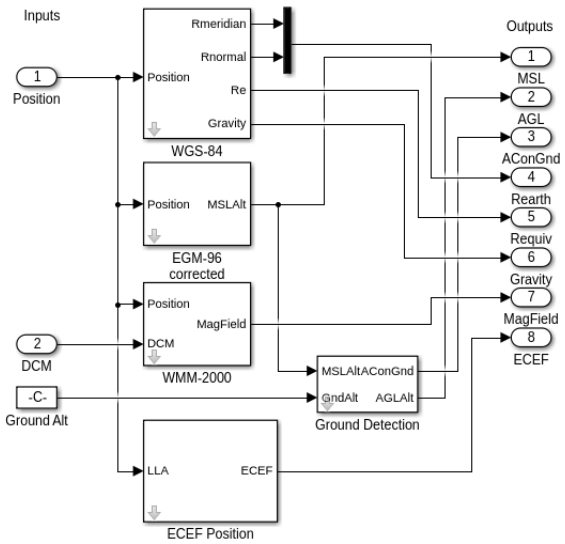

Figure C.6: Simulink Earth Model: Elektra 2 Solar Aircraft

As shown in figure C.6, the Earth subsystem is composed of five main blocks, namely: World Geodetic System 1984 (`WGS-84`) used for computing Earth radius and gravity at current aircraft location [60], Earth Gravitational Model 1996 (`EGM-96`) used for computing sea-level altitude [60], World Magnetic Model (`WMM-2000`) used for computing the local magnetic field according to [61], Earth-Centered Earth-Fixed (`ECEF Position`) used for computing the aircraft coordinates in the Earth-Centered Earth-Fixed frame, and finally `Ground Detection` block used for comparing user-specified ground altitude and sea-level altitude in order to detect collisions with the ground.

C.6 Atmosphere Model

As shown in figure C.7, the Atmosphere subsystem is composed of four main blocks, namely: `Standard Atmosphere` used for computing pressure, temperature, density

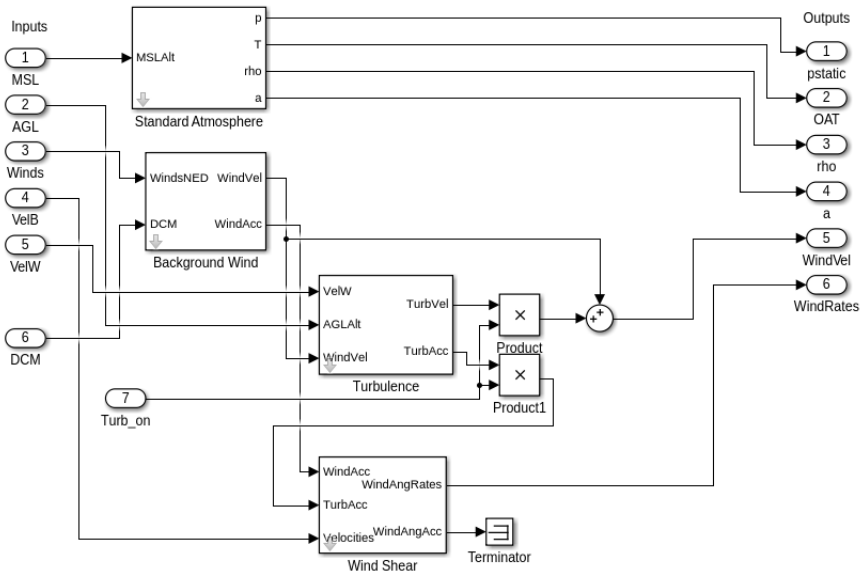

Figure C.7: Simulink Atmosphere Model: Elektra 2 Solar Aircraft

and speed of sound according to [62], `Background Wind` that transforms the wind vector to body axes and calculates the wind acceleration, the `Wind Shear` block calculates the angular rate effects of changes in background wind or turbulence, and the `Turbulence` block implements a model of continuous gusts commonly used in analysis and simulation of aircrafts.

Appendix D

Overview of State Estimation Algorithms

As defined in [63], an optimal estimator is a computational algorithm that processes measurements in order to obtain an estimate with minimal system state error. It is based on an initial estimate, the dynamic model of the system and measurements, and statistical parameters of system noise and measurement noise. This section is based of the works of [64] and [63].

D.1 The Kalman Filter Algorithm

The Kalman filter considers linear models, defined here by

$$\begin{aligned} \mathbf{x}_k &= \mathbf{A}_k\mathbf{x}_{k-1} + \mathbf{B}_k\mathbf{u}_k + \mathbf{W}_k\mathbf{q}_k \\ \mathbf{z}_k &= \mathbf{H}_k\mathbf{x}_k + \mathbf{G}_k\mathbf{r}_k \end{aligned} \tag{D.1}$$

where $\mathbf{q}_k$ and $\mathbf{r}_k$ are zero-mean, uncorrelated, white-noise

$$
\begin{aligned}
\mathbf{q}_k &\sim (0, \mathbf{Q}_k) \\
\mathbf{r}_k &\sim (0, \mathbf{R}_k) \\
E[\mathbf{q}_k q_j^T] &= \mathbf{Q}_k \delta_{k-j} \\
E[\mathbf{r}_k r_j^T] &= \mathbf{R}_k \delta_{k-j} \\
E[\mathbf{q}_k r_j^T] &= 0
\end{aligned}
\tag{D.2}
$$

The Kalman filter algorithm (table D.1) can be split into two main phases: prediction and update. The first is based on the system model to update an initial estimate, obtaining a new estimate, the so-called *a priori* estimate. The update phase obtains a so-called *posteriori* estimate from measurement and its respective model.

D.1.1 Prediction

Given an estimate of the previous state ($\hat{\mathbf{x}}_{k-1|k-1}$) with an uncertainty defined by the covariance matrix $\mathbf{P}_{k-1|k-1}$, the prediction phase obtains an *a priori* estimate ($\hat{\mathbf{x}}_{k|k-1}$) with its respective covariance $\mathbf{P}_{k|k-1}$.

The initial estimate is propagated using the system model, eq. D.9, and its expected value results in the *a priori* estimate

$$
\begin{aligned}
\hat{\mathbf{x}}_{k|k-1} &= E[\mathbf{A}_k \hat{\mathbf{x}}_{k-1|k-1} + \mathbf{B}_k \mathbf{u}_k + \mathbf{W}_k \mathbf{q}_k] \\
&= \mathbf{A}_k \hat{\mathbf{x}}_{k-1|k-1} + \mathbf{B}_k \mathbf{u}_k
\end{aligned}
\tag{D.3}
$$

Once there is no correlation between the estimate at time instant t_k and noise $\mathbf{q}_k$, the covariance of the *a priori* estimate error is

$$
\mathbf{P}_{k|k-1} = \mathbf{A}_k \mathbf{P}_{k-1|k-1} \mathbf{A}_k^T + \mathbf{Q}_k \tag{D.4}
$$

Equations (D.3) and (D.4) summarizes the prediction phase of the Kalman filter algorithm.

D.1.2 Update

Considering the *a priori* estimate, it is obtained an *a posteriori* estimate $\hat{\mathbf{x}}_{k|k}$ that embodies the measurement $\mathbf{z}_k$

$$\hat{\mathbf{x}}_{k|k} = \hat{\mathbf{x}}_{k|k-1} + K_k(\mathbf{z}_k - \mathbf{H}_k\hat{\mathbf{x}}_{k|k-1}) \tag{D.5}$$

The Kalman gain K_k is obtained by minimizing a cost function J_k based on the expected squared error of the estimate

$$J_k = E[\tilde{\mathbf{x}}_{k|k}^T\tilde{\mathbf{x}}_{k|k}] \tag{D.6}$$

where $\tilde{\mathbf{x}}_{k|k} = \hat{\mathbf{x}}_{k|k} - \mathbf{x}_k$ is the *a posteriori* estimate error. It results in

$$K_k = \mathbf{P}_{k|k-1}\mathbf{H}_k^T(\mathbf{H}_k\mathbf{P}_{k|k-1}\mathbf{H}_k^T + \mathbf{R}_k)^{-1} \tag{D.7}$$

Finally, the *a posteriori* covariance error is given by

$$\mathbf{P}_{k|k} = (\mathbf{I} - K_k\mathbf{H}_k)\mathbf{P}_{k|k-1} \tag{D.8}$$

Table D.1: Kalman Filter Algorithm

	Kalman Filter Algorithm: KF($\hat{\mathbf{x}}_{k-1\|k-1}$, $\mathbf{P}_{k-1\|k-1}$, $\mathbf{u}_k$, $\mathbf{z}_k$)
1:	$\hat{\mathbf{x}}_{k\|k-1} = \mathbf{A}_k\hat{\mathbf{x}}_{k-1\|k-1} + \mathbf{B}_k\mathbf{u}_k$
2:	$\mathbf{P}_{k\|k-1} = \mathbf{A}_k\mathbf{P}_{k-1\|k-1}\mathbf{A}_k^T + \mathbf{Q}_k$
3:	$K_k = \mathbf{P}_{k\|k-1}\mathbf{H}_k^T(\mathbf{H}_k\mathbf{P}_{k\|k-1}\mathbf{H}_k^T + \mathbf{R}_k)^{-1}$
4:	$\hat{\mathbf{x}}_{k\|k} = \hat{\mathbf{x}}_{k\|k-1} + K_k(\mathbf{z}_k - \mathbf{H}_k\hat{\mathbf{x}}_{k\|k-1})$
5:	$\mathbf{P}_{k\|k} = (\mathbf{I} - K_k\mathbf{H}_k)\mathbf{P}_{k\|k-1}$
6:	**return** $\hat{\mathbf{x}}_{k\|k}$, $\mathbf{P}_{k\|k}$

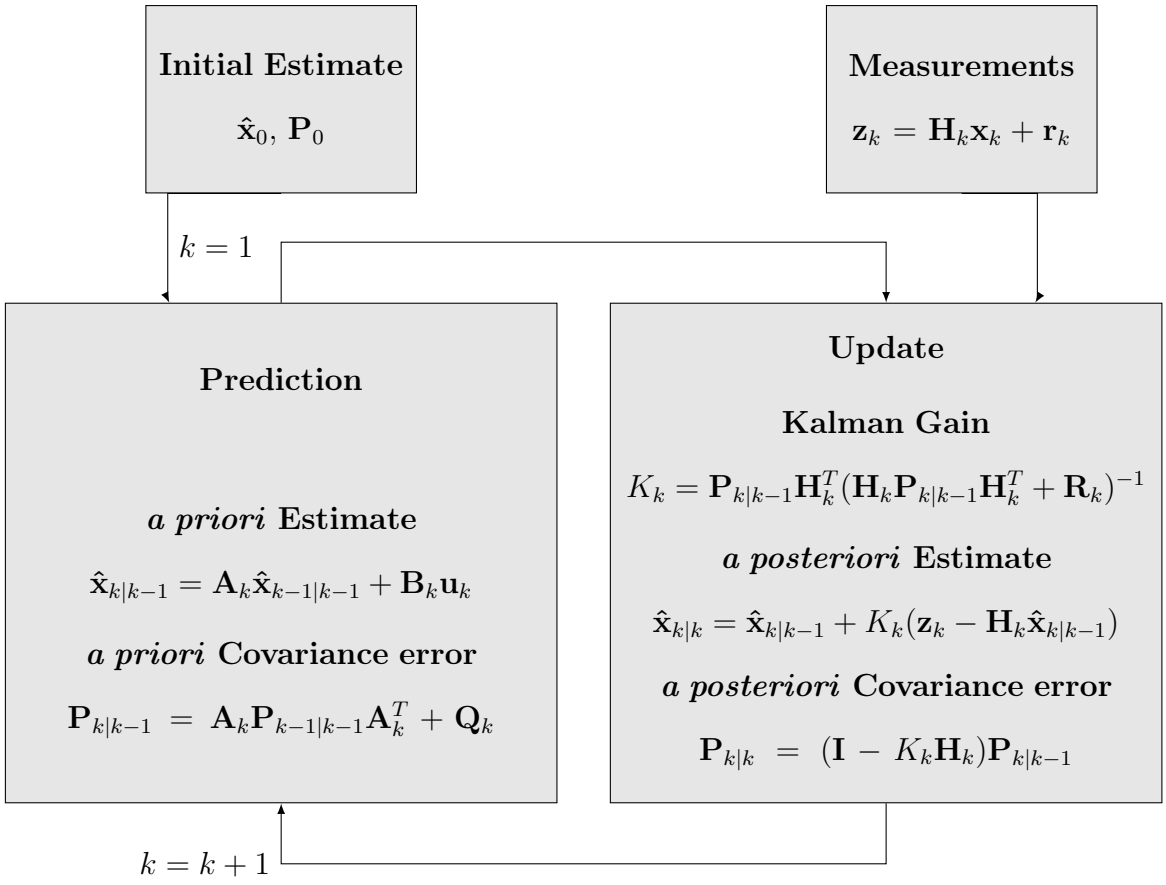

Figure D.1: Kalman Filter Block Diagram

D.2 The Extended Kalman Filter Algorithm

When the system or measurement model is nonlinear, it is not possible to apply the Kalman filter as presented above and an approximation must be obtained. The extended Kalman filter algorithm is summarized in table D.2.

Given the nonlinear system defined as

$$\begin{aligned} \mathbf{x}_k &= \mathbf{f}_k(\mathbf{x}_k) + \mathbf{q}_k \\ \mathbf{z}_k &= \mathbf{h}_k(\mathbf{x}_k) + \mathbf{r}_k \end{aligned} \tag{D.9}$$

where $\mathbf{q}_k$ and $\mathbf{r}_k$ are zero-mean, uncorrelated, white-noise

$$
\begin{aligned}
\mathbf{q}_k &\sim (0, \mathbf{Q}_k) \\
\mathbf{r}_k &\sim (0, \mathbf{R}_k) \\
E[\mathbf{q}_k q_j^T] &= \mathbf{Q}_k \delta_{k-j} \\
E[\mathbf{r}_k r_j^T] &= \mathbf{R}_k \delta_{k-j} \\
E[\mathbf{q}_k r_j^T] &= 0
\end{aligned}
\tag{D.10}
$$

The approximation used by the extended Kalman filter algorithm is based on truncated Taylor series expansion with the assumption that higher order terms are negligible. Consequently, the approximation of the nonlinear function $f(x)$ is defined as

$$
f(x) \approx f(\hat{x}) + \mathbf{F}\tilde{x} \tag{D.11}
$$

where $\mathbf{F}$ is the Jacobian of $f(x)$ evaluated at $\hat{x}$

$$
\mathbf{F} = \frac{\partial f(x)}{\partial x}\Big|_{\hat{x}} \tag{D.12}
$$

and $\tilde{x} = x - \hat{x}$ is the error from the Taylor series expansion.

The EKF algorithm is also split into prediction and update steps.

D.2.1 Prediction

Given a previous estimate $\hat{\mathbf{x}}_{k-1|k-1}$, the *a priori* estimate is defined as

$$
\hat{\mathbf{x}}_{k|k-1} = f(\hat{\mathbf{x}}_{k-1|k-1}) \tag{D.13}
$$

and the estimation error is

$$
\begin{aligned}
\tilde{\mathbf{x}}_{k|k-1} &\triangleq \hat{\mathbf{x}}_{k|k-1} - \mathbf{x}_k \\
&= \mathbf{f}_k(\hat{\mathbf{x}}_{k-1|k-1}) - \mathbf{f}_k(\mathbf{x}_{k-1}) - \mathbf{q}_k \\
&\approx \mathbf{F}_k \tilde{x}_{k-1|k-1} - \mathbf{q}_k
\end{aligned}
\tag{D.14}
$$

The *a priori* covariance error is then calculated as

$$\begin{aligned}\mathbf{P}_{k|k-1} &= E[\tilde{\mathbf{x}}_{k|k-1}\tilde{\mathbf{x}}_{k|k-1}^T] \\ &= \mathbf{F}_k\mathbf{P}_{k-1|k-1}\mathbf{F}_k^T + \mathbf{Q}_k\end{aligned} \tag{D.15}$$

D.2.2 Update

For the update phase, the measurement model is approximated by a linear system. The desired structure is given by

$$\hat{\mathbf{x}}_{k|k} = \hat{\mathbf{x}}_{k|k-1} + K_k[\mathbf{z}_k - \mathbf{h}_k(\hat{\mathbf{x}}_{k|k})] \tag{D.16}$$

Considering that the *a priori* estimate error is uncorrelated with the measurement noise, the *a posteriori* covariance is obtained by

$$\mathbf{P}_{k|k} = \mathbf{P}_{k|k-1} + K_k E[(\mathbf{h}_k(\mathbf{x}_k) - E[\mathbf{h}_k(\mathbf{x}_k)])\tilde{\mathbf{x}}_{k|k-1}^T] \tag{D.17}$$

As in the prediction phase, $\mathbf{h}_k(\mathbf{x}_k)$ is linearized through Taylor series expansion around $\hat{\mathbf{x}}_{k|k-1}$ to obtain

$$\mathbf{h}_k(\mathbf{x}_k) \approx \mathbf{h}_k(\hat{\mathbf{x}}_{k|k-1}) - \mathbf{H}_k\tilde{\mathbf{x}}_{k|k-1} \tag{D.18}$$

Equation (D.17) is then rewritten as

$$\mathbf{P}_{k|k} = \mathbf{P}_{k|k-1} + K_k\mathbf{H}_k\mathbf{P}_{k|k-1} = (I - K_k\mathbf{H}_k)\mathbf{P}_{k|k-1} \tag{D.19}$$

and the Kalman gain is given by

$$K_k = \mathbf{P}_{k|k-1}\mathbf{H}_k^T(\mathbf{H}_k\mathbf{P}_{k|k-1}\mathbf{H}_k^T + \mathbf{R}_k)^{-1} \tag{D.20}$$

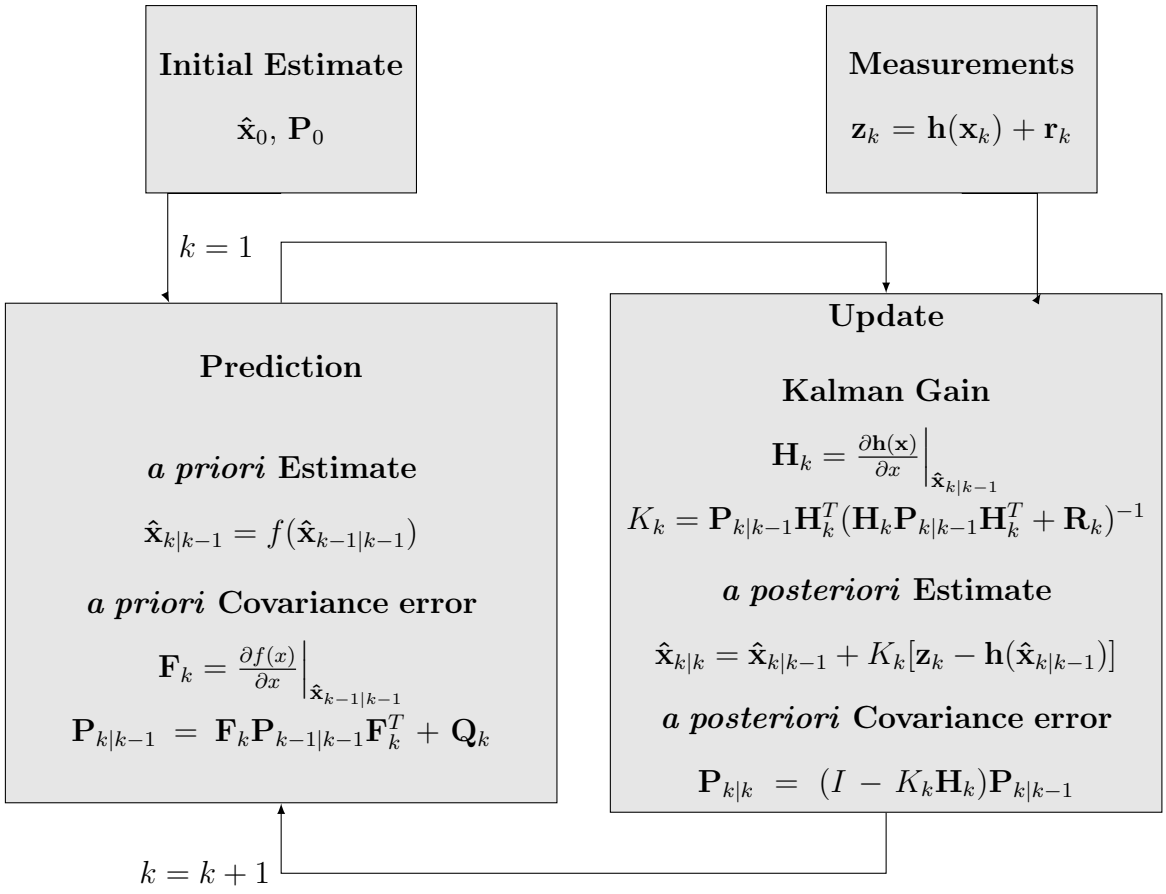

Figure D.2: Extended Kalman Filter Block Diagram

Table D.2: Extended Kalman Filter Algorithm

	Extended Kalman Filter Algorithm: EKF($\hat{\mathbf{x}}_{k-1\|k-1}$, $\mathbf{P}_{k-1\|k-1}$, $\mathbf{z}_k$)
1:	$\hat{\mathbf{x}}_{k\|k-1} = f(\hat{\mathbf{x}}_{k-1\|k-1})$
2:	$\mathbf{F}_k = \frac{\partial f(x)}{\partial x}\Big\|_{\hat{\mathbf{x}}_{k-1\|k-1}}$
3:	$\mathbf{P}_{k\|k-1} = \mathbf{F}_k\mathbf{P}_{k-1\|k-1}\mathbf{F}_k^T + \mathbf{Q}_k$
4:	$\mathbf{H}_k = \frac{\partial \mathbf{h}(\mathbf{x})}{\partial x}\Big\|_{\hat{\mathbf{x}}_{k\|k-1}}$
5:	$K_k = \mathbf{P}_{k\|k-1}\mathbf{H}_k^T(\mathbf{H}_k\mathbf{P}_{k\|k-1}\mathbf{H}_k^T + \mathbf{R}_k)^{-1}$
6:	$\hat{\mathbf{x}}_{k\|k} = \hat{\mathbf{x}}_{k\|k-1} + K_k(\mathbf{z}_k - \mathbf{h}_k(\hat{\mathbf{x}}_{k\|k}))$
7:	$\mathbf{P}_{k\|k} = (I - K_k\mathbf{H}_k)\mathbf{P}_{k\|k-1}$
8:	**return** $\hat{\mathbf{x}}_{k\|k}$, $\mathbf{P}_{k\|k}$

Appendix E

ATLMS Overview

In this section, the mathematical background of the ATLMS technique is presented based on the work of [50] and numerical simulation examples are provided. The LMS filter mathematical background is extracted from [52] and the SPRT mathematical background is extracted from [51].

E.1 Least Mean Squares Filter

The least mean squares (LMS) filter is a class of adaptive algorithm based on the stochastic gradient descent method [52]. The output y_k of the LMS filter is obtained as

$$y_k = \mathbf{x}_k^T \mathbf{w}_k \tag{E.1}$$

which is a linear combination of input components $\mathbf{x}_k = [x_0, x_1, x_2, ...]$ and adaptive weights $\mathbf{w}_k = [w_0, w_1, w_2, ...]$.

During the adaptation process, the weight vector $\mathbf{w}_k$ is adjusted to let the output of the filter y_k match a desired response signal d_k. In other words, the LMS algorithm minimizes a cost function based of the output error $\varepsilon_k = (d_k - y_k)$ as follows

$$\begin{aligned} \varepsilon_k^2 &= (d_k - y_k)^2 \\ &= (d_k - \mathbf{x}_k^T \mathbf{w}_k)^2 \end{aligned} \tag{E.2}$$

by adapting the weight vector $\mathbf{w}_k$.

The LMS algorithm is given as follows

$$\begin{aligned} \mathbf{w}_{k+1} &= \mathbf{w}_k - \mu\hat{\bigtriangledown}_k \\ &= \mathbf{w}_k + 2\mu\varepsilon_k\mathbf{x}_k \end{aligned} \tag{E.3}$$

where μ is the convergence gain that deals with the speed and stability of adaptation, $\hat{\bigtriangledown}_k$ is the gradient estimate, $\mathbf{x}_k$ is the vector of input samples and ε_k is the output error.

As discussed in [52], some adaptive algorithms estimate the gradient by taking the expected value of the mean-square error $\xi_k = E[\varepsilon_k^2]$. Instead, the LMS algorithm takes the squared error ε_k^2 itself as an estimate of its expected value ξ_k. With this simplification, the gradient estimate $\hat{\bigtriangledown}_k$ is computed at each iteration of the adaptive process as

$$\hat{\bigtriangledown}_k = \begin{bmatrix} \dfrac{\partial\varepsilon_k^2}{\partial w_0} \\ \vdots \\ \dfrac{\partial\varepsilon_k^2}{\partial w_L} \end{bmatrix} = 2\varepsilon_k \begin{bmatrix} \dfrac{\partial\varepsilon_k}{\partial w_0} \\ \vdots \\ \dfrac{\partial\varepsilon_k}{\partial w_L} \end{bmatrix} = -2\varepsilon_k\mathbf{x}_k \tag{E.4}$$

Consequently, the derivatives of ε_k with respect to the weights are obtained directly from the output error $\varepsilon_k = d_k - \mathbf{x}_k^T\mathbf{w}_k$.

E.2 The SPRT as a Decision Function for Fault Detection

Developed by A. Wald during the Second World War, the SPRT is a well known technique to compare random signals [51]. For fault detection purposes, the SPRT can be used to compare residual signals as described in definitions 4.1 and 4.2. Thus, for each data sample, three decisions can be made:

(i) In favor of a faulty mode (Hypothesis $\mathcal{H}_1$);

(ii) In favor of a normal mode (Hypothesis $\mathcal{H}_0$);

(iii) There is insufficient information to decide in favor of faulty or normal mode.

where decision (i) describes the behavior of the residual signal in case of faulty mode, decision (ii) describes the behavior of the residual signal in case of normal mode, and decision (iii) means that the system can be either in faulty or normal mode. One of the main features of the SPRT algorithm is that the number of observations required to make a decision is not determined a priori and it is also considerably lower than the required for similar hypothesis tests with fixed number of observations [51].

Let the normal mode hypothesis $\mathcal{H}_0$ be described by the residual signal r_0 with probability density function described by

$$f(r_0|\mathcal{H}_0) \tag{E.5}$$

and the faulty mode hypothesis $\mathcal{H}_1$ be described by the residual signal r_1 with probability density function of

$$f(r_1|\mathcal{H}_1) \tag{E.6}$$

Thus, the likelihood ratio of the residual signals r_1 and r_0 based on the first m observations is

$$\frac{p_{1m}}{p_{0m}} = \frac{f(r_{1m}|\mathcal{H}_1)}{f(r_{0m}|\mathcal{H}_0)} \tag{E.7}$$

In order to solve equation (E.7), the joint probability density function of residuals r_1 and r_0 need to be known. If it is assumed that residual observations are statistically independent and have the same distribution, the likelihood ratio of m residual samples can be defined as

$$\frac{p_{1m}}{p_{0m}} = \frac{f(r_{1m}|\mathcal{H}_1)}{f(r_{0m}|\mathcal{H}_0)} = \prod_{k=1}^{m} \frac{f(r_{1k}|\mathcal{H}_1)}{f(r_{0k}|\mathcal{H}_0)} \tag{E.8}$$

Therefore, according to [51], the sequential probability ratio test for testing $\mathcal{H}_0$ against $\mathcal{H}_1$ is defined as follows: if

$$B < \frac{p_{1m}}{p_{0m}} < A \tag{E.9}$$

the process is continued by taking an additional observation. A and B are chosen positive constants ($B < A$). Details of A and B selection are presented in [51]. If

$$\frac{p_{1m}}{p_{0m}} \geq A \tag{E.10}$$

the process is terminated with the rejection of the normal mode hypothesis $\mathcal{H}_0$ (i.e. acceptance of faulty mode hypothesis $\mathcal{H}_1$). If

$$\frac{p_{1m}}{p_{0m}} \leq B \tag{E.11}$$

the process is terminated with the acceptance of the normal mode hypothesis $\mathcal{H}_0$.

For implementation purposes, it is more convenient to apply the logarithm to equation (E.7), [51]. The reason for this is that $\log \frac{p_{1m}}{p_{0m}}$ can be written as the sum of m terms as follows

$$\log \frac{p_{1m}}{p_{0m}} = \log \frac{f(r_{11}|\mathcal{H}_1)}{f(r_{01}|\mathcal{H}_0)} + \log \frac{f(r_{12}|\mathcal{H}_1)}{f(r_{02}|\mathcal{H}_0)} + \ldots + \log \frac{f(r_{1m}|\mathcal{H}_1)}{f(r_{0m}|\mathcal{H}_0)} \tag{E.12}$$

Let r_{0k}, $k = 1, 2, \ldots, m$, be the representation of the k^{th} sample of the residual signal r_0 and r_{1k}, $k = 1, 2, \ldots, m$, be the representation of the k^{th} sample of the residual signal r_1. Thus, the k^{th} sample of equation (E.12) can be written as

$$L_k = \log \frac{f(r_{1k}|\mathcal{H}_1)}{f(r_{0k}|\mathcal{H}_0)} \tag{E.13}$$

As described previously, the SPRT test procedure is then carried out as follows: the cumulative sum $L_1 + \ldots + L_m$ is computed for a window of m samples. If

$$\log B < L_1 + L_2 + \ldots + L_m < \log A \tag{E.14}$$

there is not enough information to make a decision in favor of either faulty mode $\mathcal{H}_1$ or normal mode $\mathcal{H}_0$ and the procedure is continued by taking an additional observation. If

$$L_1 + L_2 + \ldots + L_m \geq \log\, A \tag{E.15}$$

the process is terminated with the acceptance of faulty mode $\mathcal{H}_1$ (rejection of normal mode $\mathcal{H}_0$). If

$$L_1 + L_2 + \ldots + L_m \leq \log\, B \tag{E.16}$$

the process is terminated with the acceptance of normal mode $\mathcal{H}_0$.

For implementation purposes, the cumulative likelihood ratio $\dfrac{p_{1m}}{p_{0m}}$ needs successive re-initializations over a predefined window of m samples. Thus, a certain time is needed to the cumulative procedure and respective declaration of SPRT decision. In order to simplify on-line implementation, the recursive characteristic of $\dfrac{p_{1m}}{p_{0m}}$ can be achieved in terms of the logarithmic likelihood ratio L_k as follows

$$L_k = L_{k-1} + \log \frac{p_{1k}}{p_{0k}} \tag{E.17}$$

E.3 ATLMS Mathematical Background

The main idea of the proposed adaptive threshold ATLMS is to use the adaptability of the LMS algorithm to reinitialize an SPRT-based test automatically [50]. The ATLMS is computed at each sampling time as:

$$\text{ATLMS}_k = \underbrace{\begin{bmatrix} u_{1k} & u_{2k} & \ldots u_{nk} & r_{0k} & 1 \end{bmatrix}}_{\phi_k^T} \overbrace{\begin{bmatrix} w_{1k} \\ w_{2k} \\ \vdots \\ w_{(n+2)k} \end{bmatrix}}^{\mathbf{w}_k} \tag{E.18}$$

where $\mathbf{w}_k$ is the weight vector of the LMS algorithm, and ϕ_k is the input signal vector composed of n control signals u_{1k}, u_{2k}, ..., u_{nk} and the insensitive residual

r_{0k} (Definition 4.2). As presented in [50], the last element of the input vector ϕ_k^T is responsible for the difference between evaluated residual r_0 and adaptive threshold. It is specially important when null values are present in all other elements of the input vector in a fault-free scenario.

As described in section E.2, the logarithmic likelihood ratio of the sensitive and insensitive residuals r_1 and r_0 (definitions 4.1 and 4.2) can be calculated at each sample k as

$$L_k = L_{k-1} + \ln \frac{p_1(r_{1k})}{p_0(r_{0k})} \tag{E.19}$$

Considering that r_0 and r_1 present Gaussian distribution with zero mean and same variance σ_0^2, the ratio $\ln \dfrac{p_1}{p_0}$ can be simplified as follows

$$\begin{aligned} \ln \frac{p_1(r_{1k})}{p_0(r_{0k})} &= \ln \frac{\dfrac{1}{\sigma_0\sqrt{2\pi}} e^{-\frac{1}{2}\left(\frac{r_{1k}}{\sigma_0}\right)^2}}{\dfrac{1}{\sigma_0\sqrt{2\pi}} e^{-\frac{1}{2}\left(\frac{r_{0k}}{\sigma_0}\right)^2}} \\ &= -\frac{1}{2}\frac{r_{1k}^2}{\sigma_0^2} + \frac{1}{2}\frac{r_{0k}^2}{\sigma_0^2} \\ &= \frac{r_{0k}^2 - r_{1k}^2}{2\sigma_0^2} \end{aligned} \tag{E.20}$$

Thus, equation (E.19) can be rewritten in terms of equation (E.20) as

$$L_k = L_{k-1} + \frac{r_{0k}^2 - r_{1k}^2}{2\sigma_0^2} \tag{E.21}$$

As described in [50], the expected value of the logarithmic likelihood ratio L_k presents trends ($\dot{L}_k$) in opposite directions under different hypotheses. This behavior can be mathematically translated as follows

$$
\begin{aligned}
E\left\{\frac{r_{0k}^2 - r_{1k}^2}{2\sigma_0^2}|\mathcal{H}_1\right\} < 0 \rightarrow \dot{L}_k < 0 \\
E\left\{\frac{r_{0k}^2 - r_{1k}^2}{2\sigma_0^2}|\mathcal{H}_0\right\} > 0 \rightarrow \dot{L}_k > 0
\end{aligned}
\tag{E.22}
$$

where $\dot{L}_k$ is approximate by equation (E.26). The usefulness of such characteristic for fault detection is discussed below.

Let γ_k be defined as the difference between the adaptive threshold ATLMS_k and the insensitive residual r_{0k} as follows

$$
\gamma_k = \text{ATLMS}_k - r_{0k} \tag{E.23}
$$

Thus, the ATLMS algorithm decision update, either (i) in favor of a faulty mode hypothesis $\mathcal{H}_1$ or (ii) in favor of a normal mode hypothesis $\mathcal{H}_0$, is defined in terms of γ_k as follows

$$
\begin{aligned}
\gamma_k \geq 0 \rightarrow \text{in favor of normal mode } \mathcal{H}_0 \\
\gamma_k < 0 \rightarrow \text{in favor of faulty mode } \mathcal{H}_1
\end{aligned}
\tag{E.24}
$$

The γ_k update should also be affected by a varying term e_k as

$$
e_k = e_0 - a\dot{L}_k \tag{E.25}
$$

where $\dot{L}_k$ is the expected trend of the likelihood ratio, e_0 is the safe distance between the adaptive threshold ATLMS_k and insensitive residual r_{0k}, and a is the sensitivity due to changes in the trend of the likelihood ratio L_k at instant k. Details about the tuning of such parameters are shown in section E.5.

Without loss of generality and for the sake of implementation procedures, the derivative of the expected value of L_k, $\dot{L}_k$, is simplified by the approximation $\dot{\hat{L}}_k$ as

$$
\dot{\hat{L}}_k \triangleq \frac{L_k - L_{k-1}}{T_s} \tag{E.26}
$$

where the additional parameter T_s is the sampling period. Let the estimation error

be defined as

$$\varepsilon_k = \gamma_k - e_k \tag{E.27}$$

Thus, the objective function to the synthesis of the adaptive threshold is defined in terms of the estimation error ε_k as

$$\min(\gamma_k - e_k)^2 \tag{E.28}$$

and the LMS algorithm is used to find the optimal weight vector $\mathbf{w}_k^*$ that minimizes such objective function.

The quadratic performance index can be rewritten as

$$\begin{aligned}(\gamma_k - e_k)^2 &= \Bigg(\phi_k^T \mathbf{w}_k - \underbrace{r_{0k} - e_0 + \left(\frac{a}{2T_s\sigma_0^2}\right)(r_{0k}^2 - r_{1k}^2)}_{s_k}\Bigg)^2 \\ &= \mathbf{w}_k^T \phi_k \phi_k^T \mathbf{w}_k - 2\phi_k^T \mathbf{w}_k s_k + s_k^2\end{aligned} \tag{E.29}$$

The weight vector $\mathbf{w}_k$ that minimizes the quadratic performance index can be found by the gradient method as in the LMS algorithm (eq. E.3) as follows

$$\mathbf{w}_k = \mathbf{w}_{k-1} + \mu \Bigg[- \frac{\partial(\gamma_k - e_k)^2}{\partial \mathbf{w}} \Bigg]_{\mathbf{w}=\mathbf{w}_{k-1}} \tag{E.30}$$

.

An approximate estimate of the gradient at each sampling instant is given by

$$\frac{\partial(\gamma_k - e_k)^2}{\partial \mathbf{w}} = 2(\gamma_k - e_k)\frac{\partial(\gamma_k - e_k)}{\partial \mathbf{w}} = 2(\gamma_k - e_k)\phi_k \tag{E.31}$$

and its proof is provided in E.4. The final form of the adaptive threshold is defined in equation (E.32) and its block diagram is presented in figure E.1.

$$
\begin{aligned}
\text{ATLMS}_k &= \phi_k^T \mathbf{w}_k \\
\mathbf{w}_k &= \mathbf{w}_{k-1} - 2\mu(\gamma_{k-1} - e_{k-1})\phi_{k-1} \\
&= \mathbf{w}_{k-1} - 2\mu\left[\phi_{k-1}^T \mathbf{w}_{k-1} - r_{0k-1} - e_0 + \frac{a}{T_s}\left(\frac{r_{0k-1}^2 - r_{1k-1}^2}{2\sigma_0^2}\right)\right]\phi_{k-1}
\end{aligned}
\tag{E.32}
$$

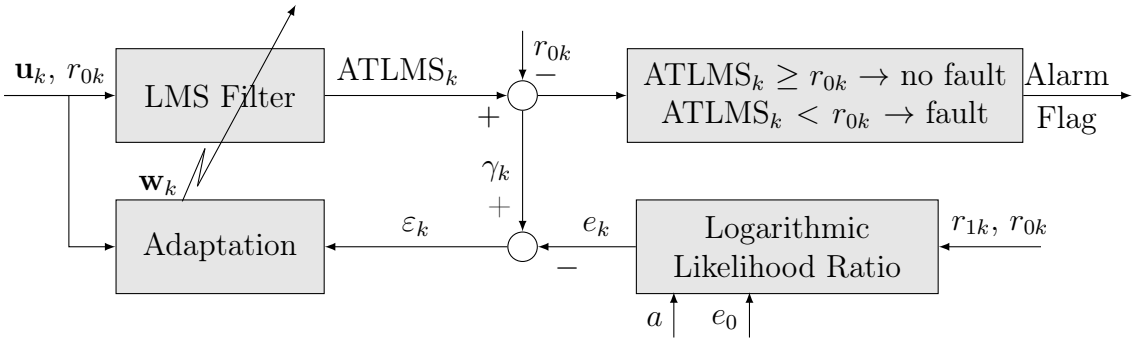

Figure E.1: ATLMS Block diagram: $\mathbf{u}_k$ is the control signal vector, r_{0k} is the insensitive residual, r_{1k} is the sensitive residual, ε is the LMS error, $\mathbf{w}_k$ is the weight vector of the LMS algorithm. Both safety offset e_0 and sensitivity factor a are ATLMS tuning parameters. A fault alarm flag is raised if the adaptive threshold $ATLMS$ crosses downwards the insensitive residual r_0 (ATLMS$_k < r_{0k}$).

E.4 ATLMS Optimal Weight Vector

As shown in [50], the expected value of the quadratic performance index $(\gamma_k - e_k)^2$ in equation (E.29) is

$$E\Big\{(\gamma_k - e_k)^2\Big\} = E\Big\{\mathbf{w}_k^T \phi_k \phi_k^T \mathbf{w}_k\Big\} - E\Big\{2\phi_k^T \mathbf{w}_k s_k\Big\} + E\{s_k^2\} \tag{E.33}$$

and its partial derivative regarding the weight vector $\mathbf{w}$ is

$$\begin{aligned} \frac{\partial E\big\{(\gamma_k - e_k)^2\big\}}{\partial \mathbf{w}} &= 2E\{\phi_k \mathbf{w}_k \phi_k^T\} - 2\underbrace{E\{\phi_k^T s_k\}}_{\Theta_k} \\ &= 2\big[E\{\phi_k \mathbf{w}_k \phi_k^T\} - \Theta_k\big] \end{aligned} \tag{E.34}$$

.

The result presented in equation (E.34) must be the same as the expected value of gradient estimate $2(\gamma_k - e_k)\phi_k$ in equation (E.31), as follows

$$\begin{aligned} E\{2(\gamma_k - e_k)\phi_k\} &= 2\big[E\{\gamma_k \phi_k\} - E\{e_k \phi_k\}\big] \\ &= 2\big[E\{\mathrm{ATLMS}_k \phi_k - r_{0k}\phi_k\} - E\{(e_0 - a\dot{\hat{L}}_k)\phi_k\}\big] \\ &= 2\big[E\{\phi_k^T \mathbf{w}_k \phi_k - r_{0k}\phi_k\} - E\{(e_0 - a\dot{\hat{L}}_k)\phi_k\}\big] \\ &= 2\big[E\{\phi_k^T \mathbf{w}_k \phi_k\} - E\{(\underbrace{r_{0k} + e_0 - a\dot{\hat{L}}_k}_{s_k})\phi_k\}\big] \\ &= 2\big[E\{\phi_k^T \mathbf{w}_k \phi_k\} - \underbrace{E\{\phi_k s_k\}}_{\Theta_k}\big] \\ &= 2\big[E\{\phi_k^T \mathbf{w}_k \phi_k\} - \Theta_k\big] \end{aligned} \tag{E.35}$$

This proves that

$$\frac{\partial E\{(\gamma_k - e_k)^2\}}{\partial \mathbf{w}} = E\{2(\gamma_k - e_k)\phi_k\} = 2[E\{\phi_k \phi_k^T\}\mathbf{w}_k - \Theta_k] \tag{E.36}$$

and therefore $\mathbf{w}_k$ gets closer to the optimal weight vector $\mathbf{w}^*$.

E.5 ATLMS Tuning Parameters

In this subsection, the ATLMS tuning parameters are further discussed.

- **Safety Offset** e_0: As discussed before, a fault flag is raised if the ATLMS crosses the insensitive residual r_0. Therefore, the dynamics of the insensitive residual r_0 must be taken into account in order to minimize false/missed alarm rates. For this reason, the safety offset $e_0 > 0$ is arbitrarily set to prevent undesired false alarms during the transient response of r_0.

- **Sensitivity Rate** a: It describes the sensitivity of the adaptive threshold due to changes in the trend of the residuals as determined by the logarithmic likelihood ratio (eq. E.20). In case of fault occurrence and for $a < 0$, the adaptive threshold goes in the direction of the insensitive residual r_0. Otherwise, the adaptive threshold increases in the opposite direction of the insensitive residual.

- **ATLMS Convergence Rate** μ: Originally from the LMS algorithm, the parameter μ is responsible for the adaptation stability and convergence speed of the ATLMS. Details on how to select convergance rate μ is presented in [52].

E.6 Numerical Examples

E.6.1 Example 1: Abrupt, Incipient and Intermittent Faults

In the first ATLMS numerical example, abrupt, incipient (also known as drift fault) and intermittent faults are considered. Abrupt fault f_{abrupt} is modelled as a step function defined by fault amplitude $a = 1$ and time of fault occurrence $t_f = 50$ s as follows

$$f_{abrupt} := \begin{cases} 0, & t < t_f \\ a, & t \geq t_f \end{cases} \tag{E.37}$$

Incipient fault $f_{incipient}$ is modelled as a ramp function defined by fault slope $a = 0.01$ and time of fault occurrence $t_f = 50$ s as follows

$$f_{incipient} := \begin{cases} 0, & t < t_f \\ a(t - t_f), & t \geq t_f \end{cases} \tag{E.38}$$

Finally, the intermittent fault $f_{intermittent}$ is modelled as a set of step functions defined by fault amplitude $a = 1$ and duration of fault occurrence from $t_{f1} = 50$ s to $t_{f2} = 100$ s and from $t_{f3} = 250$ s to $t_{f4} = 300$ s as follows

$$f_{intermittent} := \begin{cases} 0, & t < t_{f1},\ t_{f2} \leq t < t_{f3}, \text{ and } t \geq t_{f4} \\ a, & t_{f1} \leq t < t_{f2} \text{ and } t_{f3} \leq t < t_{f4} \end{cases} \tag{E.39}$$

A general scheme of the simulation is presented in figure E.2. As exposed in [50], the effectiveness of the ATLMS technique is constrained to adequate residual generation and does not require any knowledge of the process, except for its control signal.

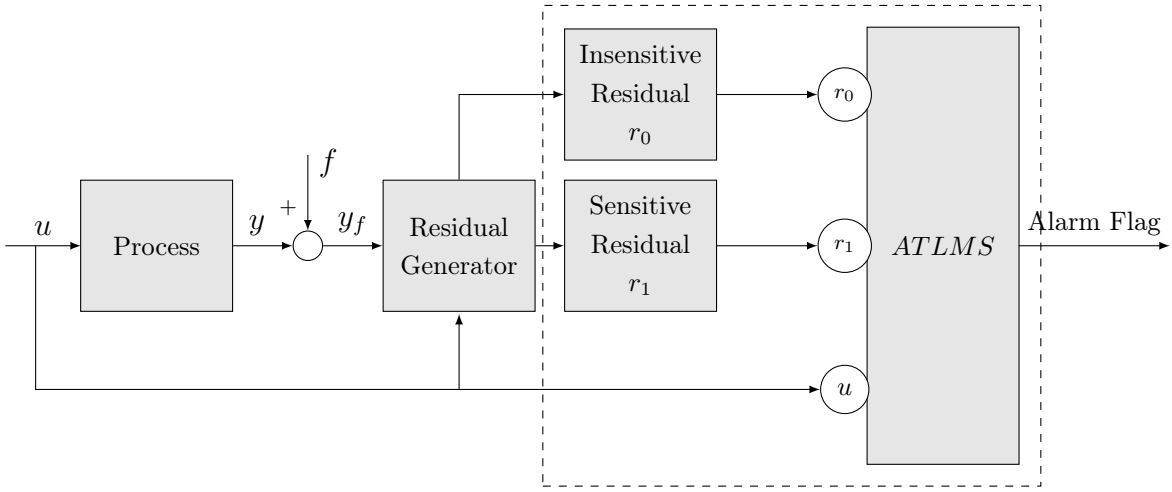

Figure E.2: ATLMS general scheme for numerical simulations.

Therefore, consider the insensitive residual r_0 (definition 4.2) described by a

Gaussian distributed signal with zero mean and variance $\sigma_0^2 = 0.01$ and the sensitive residual r_1 (definition 4.1) also described by a Gaussian distributed signal with zero mean, variance $\sigma_1^2 = 0.01$ and fault behavior (abrupt, incipient and intermittent) as described in equations (E.37), (E.38) and (E.39). Sensitive and insensitive residuals are presented in E.3.

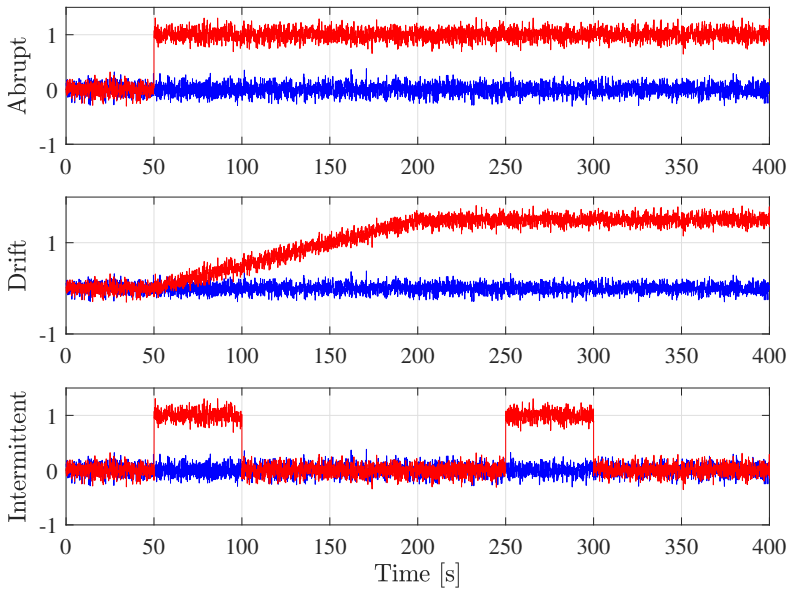

Figure E.3: Fault sensitive residual r_1 (red) and fault insensitive residual r_0 (blue) for abrupt (top), incipient (middle), and intermittent (bottom) fault scenarios.

The ATLMS parameter configuration is given in table E.1

Table E.1: ATLMS parameter configuration for numerical examples

Safety Offset e_0	Sensitivity Factor a	Convergence Rate μ	Control Signal $\mathbf{u}$	Sampling Time T_s	Filter Order ord
50	-0.2	0.005	$\begin{bmatrix} 0.5sin(0.2t) & 5e^{-t} \end{bmatrix}^T$	0.01	4

The ATLMS response for such fault scenarios (fig. E.3) is presented in figure E.4 and the ATLMS weight responses are presented in figure E.5. As expected, the adaptive threshold crosses the insensitive residual r_0 due to fault occurrence. In case of intermittent faults, the ATLMS response recovers from faulty behavior as fault effects vanishes during simulation.

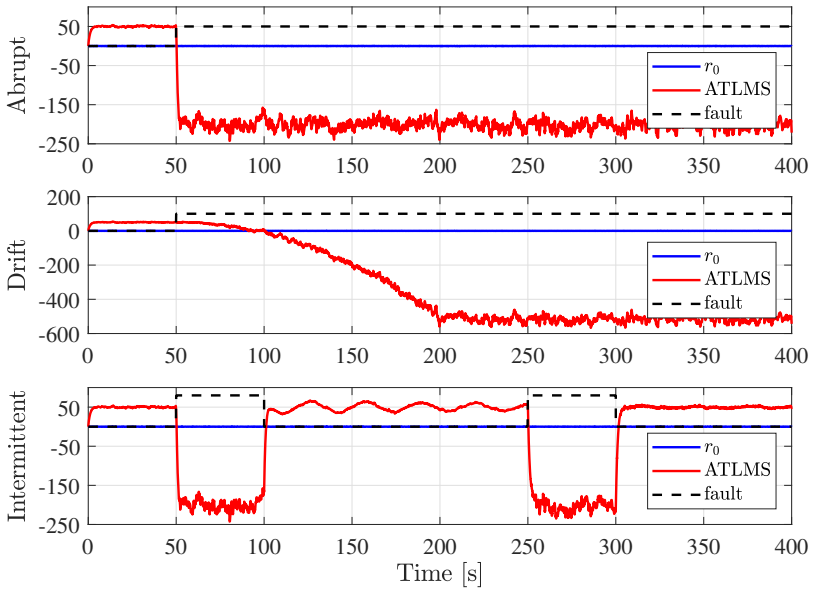

Figure E.4: ATLMS response for abrupt, drift, and intermittent fault scenarios.

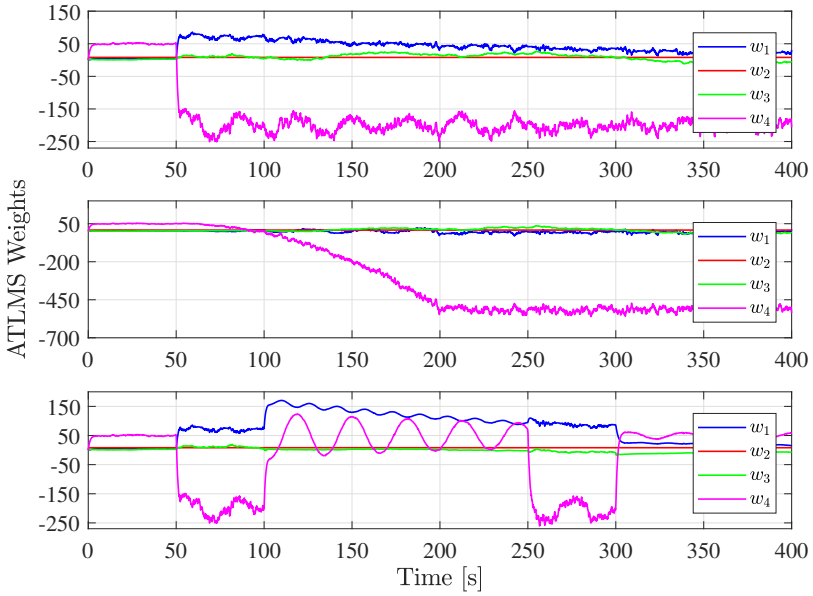

Figure E.5: ATLMS weights for abrupt, drift, and intermittent fault scenarios.

E.6.2 Example 2: ATLMS Parameter Tuning

In the second example, effects of ATLMS parameter tuning are discussed in terms of detection promptness regarding an abrupt fault scenario as described in equation (E.37, with fault amplitude $a = 1$, time of fault occurrence $t_f = 5$ s). As a consequence, a trade-off between detection promptness and false alarms may take

place.

Figures E.6, E.7 and E.8 show the ATLMS responses for an abrupt fault regarding different values of the safety offset e_0, sensitivity factor a and convergence rate μ, respectively. In figure E.6, the higher the value of the safety offset e_0, the longer the ATLMS takes to cross the insensitive residual ($\text{ATLMS}_k < r_{0k}$). Therefore, suitable tuning of the of the safety offset parameter e_0, for example, affects the detection promptness of the adaptive threshold.

In figure E.7, the higher the absolute value of the sensitivity factor a, the faster the ATLMS crosses the insensitive residual ($\text{ATLMS}_k < r_{0k}$). However, an increase of the sensitivity factor may cause undesired false alarms during ATLMS initialization.

Finally, in figure E.8, the higher the value of the convergence rate μ, the faster the ATLMS crosses the insensitive residual ($\text{ATLMS}_k < r_{0k}$). However, an excessive increase of μ could also lead to undesirably large values for LMS the weight vector $\mathbf{w}$.

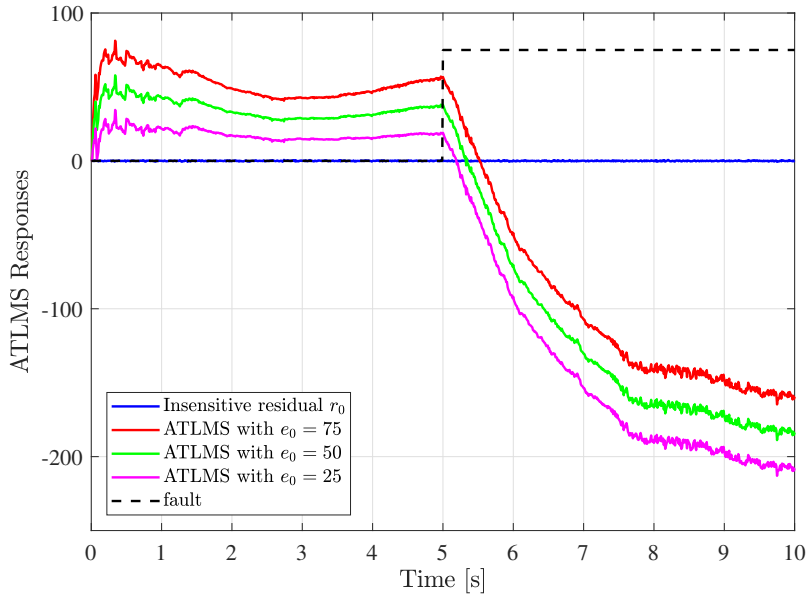

Figure E.6: ATLMS response for an abrupt fault regarding different values of safety offset e_0 parameter.

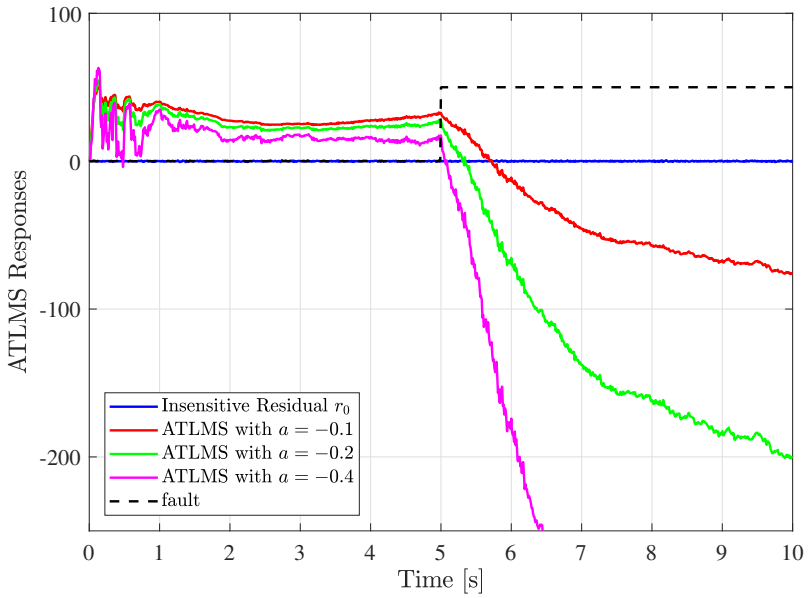

Figure E.7: ATLMS response regarding different values of sensitivity factor a parameter.

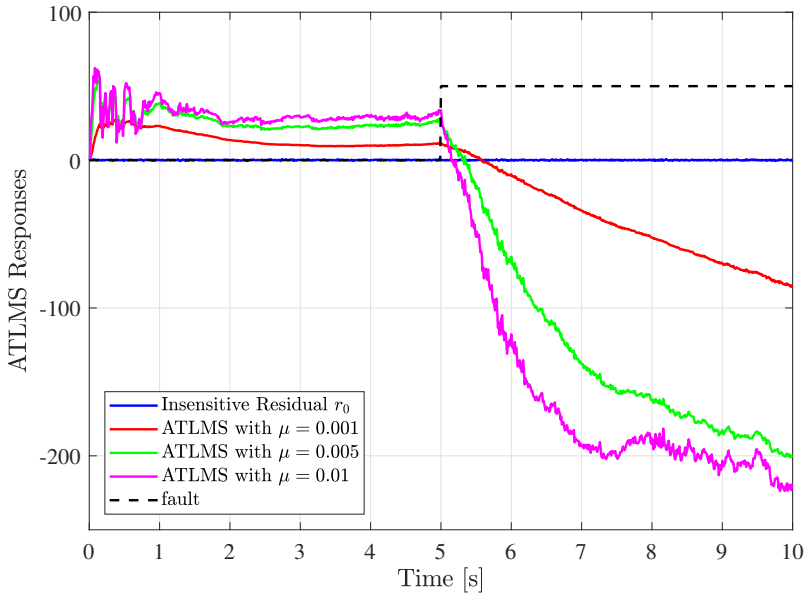

Figure E.8: ATLMS response regarding different values of convergence rate μ parameter.

E.6.3 Example 3: Dynamic Effects of Insensitive Residual on ATLMS Response

In the third example, dynamic effects on the insensitive residual are considered. Such effects may arise due to process perturbations caused by control actions or due to the dynamic nature of the residual generator. As a consequence, non-zero insensitive

residual values are generated. Figure E.9 shows an example of such behavior with an abrupt fault scenario as described in equation (E.37, with fault amplitude $a = 1$, time of fault occurrence $t_f = 5$ s). It is noticed that the adaptive threshold tolerates the deviation of the insensitive residual and do not produce false alarms. On the other hand, the ATLMS crosses the insensitive residual r_0 ($\text{ATLMS}_k < r_{0k}$) as soon as the abrupt fault occurs at 5 s.

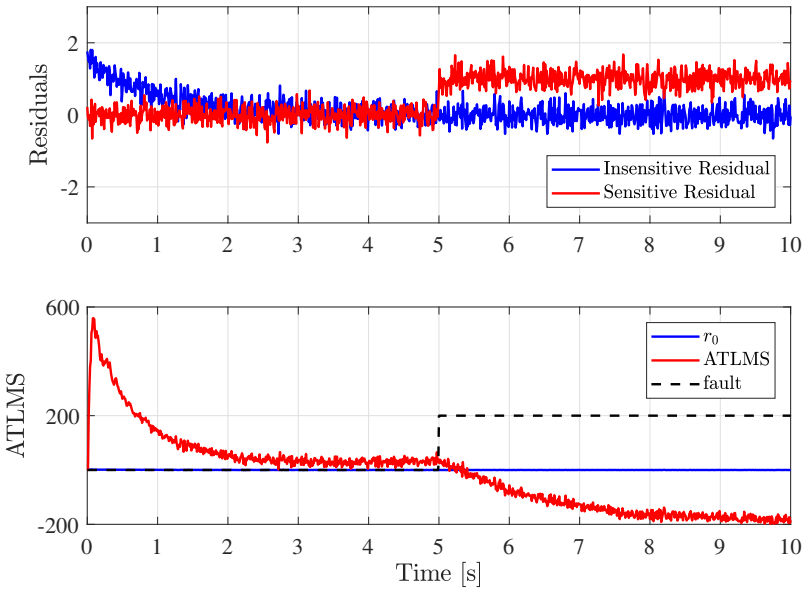

Figure E.9: Effects of insensitive residual dynamics on the ATLMS performance.

Appendix F

Principal Component Algorithm and Mathematical Background

This section is based on the works of [4] and [6] and presents a brief overview of the Principal Component Analysis algorithm and its mathematical background. The basic idea of PCA is to reduce the dimensionality of a data set of interrelated variables, while retaining as much as possible of the information present in such data set [4].

F.1 PCA Mathematical Background

As described in [6], consider the data matrix $\mathbf{X}_{[m\times n]}$ in which each row, $\mathbf{x}_i$ with $i = 1, 2, \ldots, m$, is a measurement sample of n variables taken at a specific time.

The main idea of the PCA algorithm is transforming the data matrix $\mathbf{X}_{[m\times n]}$ into a new data matrix $\mathbf{T}_{[m\times r]}$ with the same m measurements but smaller dimension r (the principal components, $r < n$) through a transformation matrix $\mathbf{P}_{[n\times r]}$ as

$$\mathbf{T}_{[m\times r]} = \mathbf{X}_{[m\times n]}\mathbf{P}_{[n\times r]} \tag{F.1}$$

In order to achieve equation F.1, let the data matrix $\mathbf{X}_{[m\times n]}$ be defined in terms of r pairs of vectors. Each of those pairs of vectors contains a vector in $\mathcal{R}^n$ called

the loadings, $\mathbf{p}_j$ with $j = 1, 2, \ldots, r$, and a vector in $\mathcal{R}^m$, referred to as the scores, $\mathbf{t}_j$ with $j = 1, 2, \ldots, r$.

Therefore, the data matrix $\mathbf{X}_{[m\times n]}$ can be rewritten as

$$\mathbf{X}_{[m\times n]} = \mathbf{T}_{[m\times r]}\mathbf{P}^T_{[r\times n]} = \mathbf{t}_1\mathbf{p}_1^T + \mathbf{t}_2\mathbf{p}_2^T + \ldots + \mathbf{t}_r\mathbf{p}_r^T = \sum_{j=1}^{r} \mathbf{t}_j\mathbf{p}_j^T \tag{F.2}$$

where the orthonormal matrix $\mathbf{P}_{[n\times r]} = [\mathbf{p}_1, \mathbf{p}_2, \ldots, \mathbf{p}_r]$ is referred to as loading matrix (also known as transformation matrix) and $\mathbf{T}_{[m\times r]} = [\mathbf{t}_1, \mathbf{t}_2, \ldots, \mathbf{t}_r]$ is called the score matrix.

If data matrix $\mathbf{X}_{[m\times n]}$ is mean-centered (each variable is scaled to have zero mean, [6]), the covariance matrix $\mathbf{A}_{[n\times n]}$ can be defined as

$$\mathbf{A}_{[n\times n]} = \frac{\mathbf{X}^T\mathbf{X}}{m-1} \tag{F.3}$$

As exposed in [6], the loading vectors $\mathbf{p}_j$ are the eigenvectors of the covariance matrix $\mathbf{A}_{[n\times n]}$ associated with the r largest (most significant) eigenvalues λ_j as described in equation F.4.

$$\mathbf{A}_{[n\times n]}\mathbf{p}_j = \lambda_j\mathbf{p}_j \text{ with } j = 1, 2, \ldots, r, \ldots, n \tag{F.4}$$

At this point, an optimization problem is defined to find the elements $\mathbf{p}_j$ of the transformation matrix $\mathbf{P}_{[n\times r]}$ that leads to maximal data variances [4].

For each step j with

$$\mathbf{t}_j = \mathbf{X}\mathbf{p}_j \tag{F.5}$$

the maximal variance of data $\mathbf{t}_j$ is defined as

$$\begin{aligned} \max\ \mathbf{t}_j^T\mathbf{t}_j &= \max\ (\mathbf{X}\mathbf{p}_j)^T(\mathbf{X}\mathbf{p}_j) \\ &= \max\ \mathbf{p}_j^T\mathbf{X}^T\mathbf{X}\mathbf{p}_j \end{aligned} \tag{F.6}$$

under the constraint $\mathbf{p}_j^T\mathbf{p}_j = 1$ since $\mathbf{p}_j$ are orthonormal components of $\mathbf{P}_{[n\times r]}$.

As exposed in [4], the method of Lagrange multipliers is used to solve this

optimization problem.

If the function $f(\mathbf{p}_j)$ has to be maximized under the constraint $g(\mathbf{p}_j) = \mathbf{p}_j^T\mathbf{p}_j - 1 = 0$, the objective function V is then

$$V = f(\mathbf{p}_j) - \lambda_j g(\mathbf{p}_j) \tag{F.7}$$

where λ_j is the Lagrange multiplier.

Therefore,

$$V = \mathbf{p}_j^T\mathbf{X}^T\mathbf{X}\mathbf{p}_j - \lambda_j(\mathbf{p}_j^T\mathbf{p}_j - 1) \tag{F.8}$$

and

$$\begin{aligned}\frac{dV}{d\mathbf{p}_j} &= 2\mathbf{X}^T\mathbf{X}\mathbf{p}_j - 2\lambda_j\mathbf{p}_j = \mathbf{0} \\ &= \left[\mathbf{X}^T\mathbf{X} - \lambda_j\mathbf{I}\right]\mathbf{p}_j = \mathbf{0}\end{aligned} \tag{F.9}$$

From the definition of covariance matrix $\mathbf{A}_{[n\times n]}$ (eq. (F.3)), equation (F.9) can be rewritten as a standard eigenvalue problem

$$\left[\mathbf{A} - \lambda_j\mathbf{I}\right]\mathbf{p}_j = \mathbf{0} \tag{F.10}$$

Rearranging equation (F.10), it results in

$$\mathbf{p}_j^T\mathbf{A}\mathbf{p}_j = \mathbf{p}_j^T\lambda_j\mathbf{p}_j \tag{F.11}$$

and applying equation (F.11) to equation (F.6), it leads to

$$\max\ \mathbf{t}_j^T\mathbf{t}_j = \max\ \mathbf{p}_j^T\lambda_j\mathbf{p}_j \tag{F.12}$$

In conclusion, the value of each eigenvalue λ_j with $j = 1, 2, \ldots, n$ is equal to the variance in the data set associated with the vector direction $\mathbf{p}_j$ with $j = 1, 2, \ldots, n$. Consequently, maximal eigenvalues λ_j provide maximal variance for coordinates $\mathbf{t}_j$.

The transformation matrix $\mathbf{P}_{[n\times r]}$, the new variable $\mathbf{T}_{m\times r}$, and the back-transformed variable $\mathbf{X}^*_{[n\times m]}$ are determined by the following six steps in table F.1, as presented in [6].

Table F.1: PCA Algorithm

Step 1:	Define data matrix $\mathbf{X}_{[m\times n]}$ in which each row, $\mathbf{x}_i$ with $i = 1, \ldots m$, is a sample of n variables taken at a specific time
Step 2:	Compute mean-centered data matrix $\mathbf{X}_{[m\times n]}$ in which each variable is scaled to have zero mean)
Step 3:	Calculation of covariance matrix $\mathbf{A}_{[n\times n]} = \dfrac{\mathbf{X}^T\mathbf{X}}{m-1}$
Step 4:	Calculation of the eigenvalues λ_j of matrix $\mathbf{A}$ and respective eigenvectors $\mathbf{p}_j$ with $j = 1, \ldots, n$
Step 5:	Selection of the most significant eigenvalues λ_j and corresponding eigenvectors $\mathbf{p}_j$ with $j = 1, \ldots, r$.
Step 6:	Determination of the transformation matrix $\mathbf{P}_{[n\times r]} = [\mathbf{p}_1, \mathbf{p}_2, \ldots, \mathbf{p}_r]$
Step 7:	Calculation of the new data matrix $\mathbf{T}_{[m\times r]} = \mathbf{XP} = [\mathbf{t}_1, \mathbf{t}_2, \ldots, \mathbf{t}_r]$ with $\mathbf{t}_j = \mathbf{X}\mathbf{p}_j$. Matrix $\mathbf{T}$ contains original data with a reduced number $r < n$ of variables, the principal components.
Step 8:	Back-transformation to the original data coordination system with only significant variances leads to $\mathbf{X}^*_{[m\times n]} = \mathbf{T}_{[m\times r]}\mathbf{P}^T_{[r\times n]}$ $= \mathbf{X}_{[m\times n]}\mathbf{P}_{[n\times r]}\mathbf{P}^T_{[r\times n]}$

Appendix G

EKF-ATLMS Fault Detection and Diagnosis Approach: Additional Results

Additional results for the EKF-ATLMS fault detection and diagnosis approach are presented. Such results cover abrupt and incipient faults in the remaining IMU sensor measurements as exposed in table G.1. Figure G.1 presents a general scheme of the EKF-ATLMS for fault detection in all IMU measurements.

Table G.1: Guidelines for simulation campaign.

Number of Simulations	100
Initial desired V_a	random integer between 15 and 21 m/s
Initial desired h	random integer between 500 and 1500 m
Initial desired ψ	random integer between 138° and 160°
Changing Desired Flight Conditions (V_a, h, ψ)	random time instant between 30 and 80 s (cruise flight) with random integer values for V_a, h, and ψ as defined above
Fault occurrence	50 s
Abrupt fault amplitude in r	linearly spaced values between 0.05 and 0.5 rad/s
Drift fault amplitude in r	linearly spaced values between 0.005 and 0.02 rad/s
Abrupt fault amplitude in a_y	linearly spaced values between 0.03 and 3 m/s^2
Drift fault amplitude in a_y	linearly spaced values between 0.02 and 0.2 m/s^2
Abrupt fault amplitude in a_z	linearly spaced values between 0.04 and 4 m/s^2
Drift fault amplitude in a_z	linearly spaced values between and m/s^2

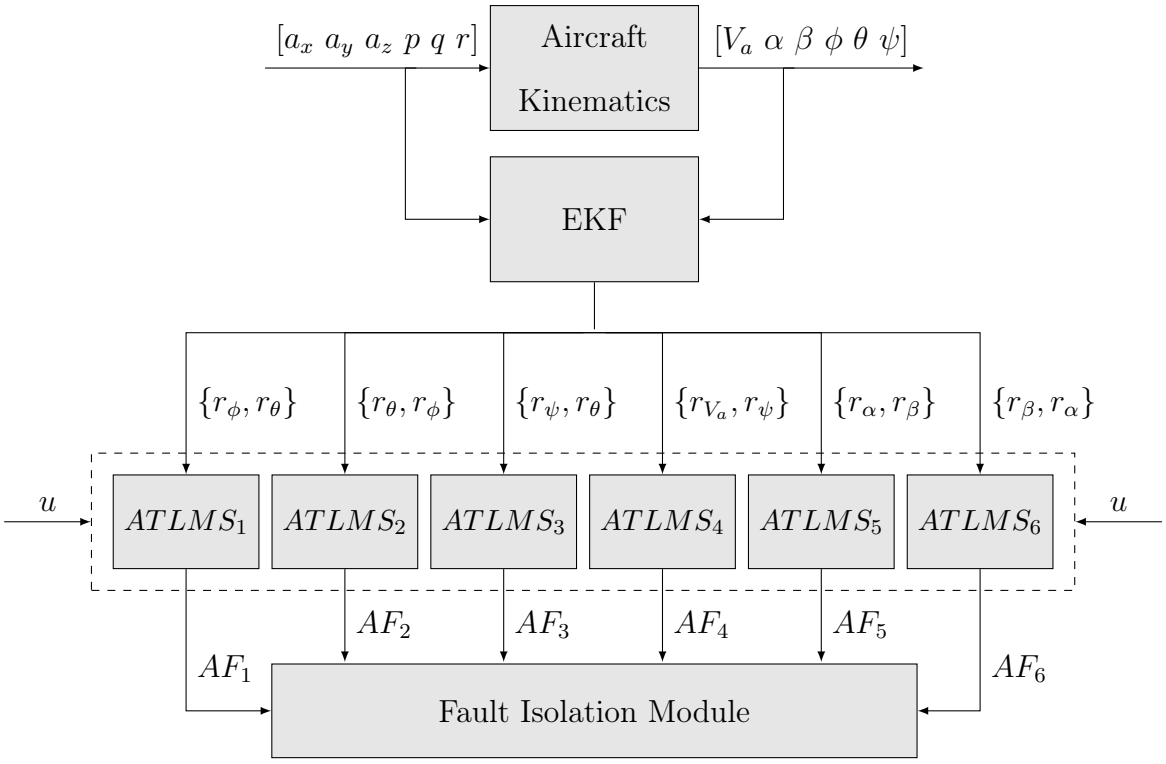

Figure G.1: A general scheme for the EKF-ATLMS fault detection an diagnosis approach. The input vector of the EKF is composed of the aircraft accelerations (a_x, a_y, a_z) and aircraft angular rates (p, q, r); The output vector of the EKF is composed of the attitude angles (ϕ, θ, ψ) and aircraft airspeed V_a, angle of attack α, and sideslip angle β. $\{r_i, r_j\}$ is the pair of evaluated residuals. AF_n, with $n = 1, \ldots, 6$, indicates the alarm flag of each ATLMS module. u is the control vector composed of the control signals for the elevator δ_e, aileron δ_a, rudder δ_r, and thrust δ_t.

Table G.2 shows the ATLMS sign patterns used for fault diagnosis. It is important to highlight that faults in gyroscopes measurements (angular rates p, q, r) are mainly described by ATLMS modules 1, 2 and 3 while faults in accelerometer measurements (a_x, a_y, a_z) are described in terms of the sign patterns of the ATLMS modules 4, 5, 6. Figures G.2 and G.3 show the adaptive threshold response regarding abrupt and incipient faults in yaw rate r during simulation campaign. Also, a fault (abrupt or incipient) in yaw rate produces a sign pattern $(+\ +\ -\ *\ *\ *)$ on the adaptive thresholds, which significantly contributes for fault diagnosis purposes.

The positive sign + indicates that the adaptive threshold keeps a positive value after fault occurrence ($\text{ATLMS}_{1k} \geq r_{\theta k}$ and $\text{ATLMS}_{2k} \geq r_{\phi k}$). On the other hand, the negative sign − indicates that the adaptive threshold assumes negative values

after fault occurrence ($\text{ATLMS}_{3k} < r_{\theta k}$). The $*$ symbol indicates that the adaptive threshold assumes either positive or negative values after fault occurrence. A similar analysis can be done in other fault scenarios.

Finally, figures G.4 - G.7 show the adaptive threshold response regarding abrupt and incipient faults in aircraft acceleration measurements a_y and a_z regarding the simulation campaign presented in table G.1. Finally, table G.3 provides the parameter tuning of each ATLMS module.

Table G.2: Complete isolation patterns for faults in aircraft IMU sensor measurements. The positive sign + indicates that the adaptive threshold keeps a positive value after fault occurrence ($\text{ATLMS}_k \geq r_{0k}$). On the other hand, the negative sign − indicates that the adaptive threshold assumes negative values after fault occurrence ($\text{ATLMS}_k < r_{0k}$). The $*$ symbol indicates that the adaptive threshold assumes either positive or negative values after fault occurrence.

	r_0	r_1	No fault	p	q	r	a_x	a_y	a_z
ATLMS_1	θ	ϕ	+	−	+	+	$*$	$*$	$*$
ATLMS_2	ϕ	θ	+	+	−	+	$*$	$*$	$*$
ATLMS_3	θ	ψ	+	+	−	−	$*$	$*$	$*$
ATLMS_4	ψ	V_a	+	$*$	$*$	$*$	−	−	−
ATLMS_5	β	α	+	$*$	$*$	$*$	+	+	−
ATLMS_6	α	β	+	$*$	$*$	$*$	+	−	+

Table G.3: ATLMS parameter tuning for Kinematic ATLMS approach. r_1 and r_0 = evaluated residuals; e_0 = safety offset; a = sensitivity factor; μ = convergence rate.

	r_0	r_1	e_0	a	μ
ATLMS_1	θ	ϕ	2.5	-0.1	0.005
ATLMS_2	ϕ	θ	2	-0.1	0.005
ATLMS_3	θ	ψ	1	-0.1	0.005
ATLMS_4	ψ	V_a	3	-0.1	0.005
ATLMS_5	β	α	1	-0.1	0.005
ATLMS_6	α	β	1	-0.1	0.005

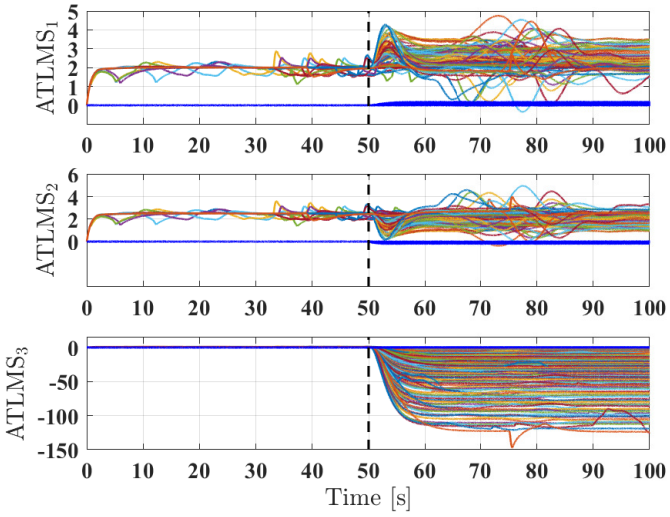

Figure G.2: Adaptive threshold responses for the EKF-ATLMS approach regarding abrupt faults in yaw rate r during simulation campaign as defined in table G.1. After fault occurrence, $\text{ATLMS}_1 > r_\theta$, $\text{ATLMS}_2 > r_\phi$, and $\text{ATLMS}_3 < r_\theta$. ATLMS_4, ATLMS_5, and ATLMS_6 can assume either positive or negative values. This behavior produces the adaptive threshold sign pattern $(+, +, -, *, *, *)$ which can provide useful information for fault diagnosis.

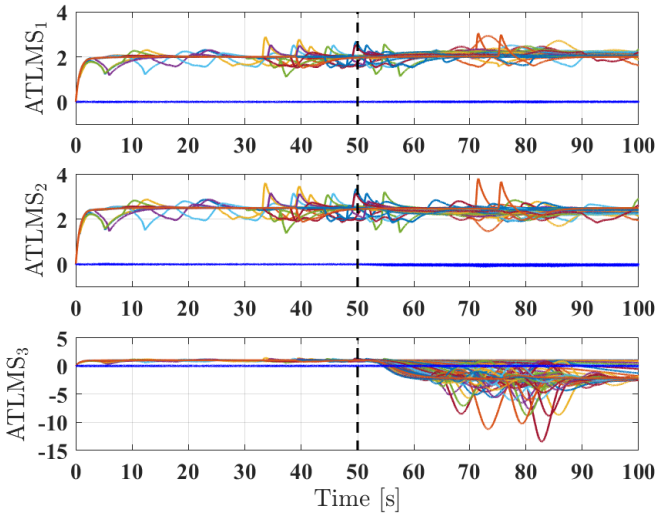

Figure G.3: Adaptive threshold responses for the EKF-ATLMS approach regarding incipient faults in yaw rate r during simulation campaign as defined in table G.1. After fault occurrence, $\text{ATLMS}_1 > r_\theta$, $\text{ATLMS}_2 > r_\phi$, and $\text{ATLMS}_3 < r_\theta$. ATLMS_4, ATLMS_5, and ATLMS_6 can assume either positive or negative values. This behavior produces the adaptive threshold sign pattern $(+, +, -, *, *, *)$ which can provide useful information for fault diagnosis.

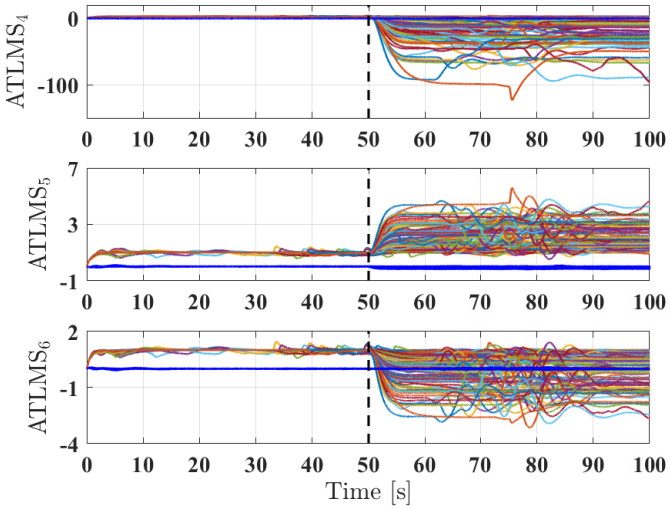

Figure G.4: Adaptive threshold responses for the EKF-ATLMS approach regarding abrupt faults in aircraft acceleration a_y during simulation campaign as defined in table G.1. After fault occurrence, $\text{ATLMS}_4 < r_\psi$, $\text{ATLMS}_5 > r_\beta$, and $\text{ATLMS}_6 < r_\alpha$. ATLMS_1, ATLMS_2, and ATLMS_3 can assume either positive or negative values. This behavior produces the adaptive threshold sign pattern $(*, *, *, -, +, -)$ which can provide useful information for fault diagnosis.

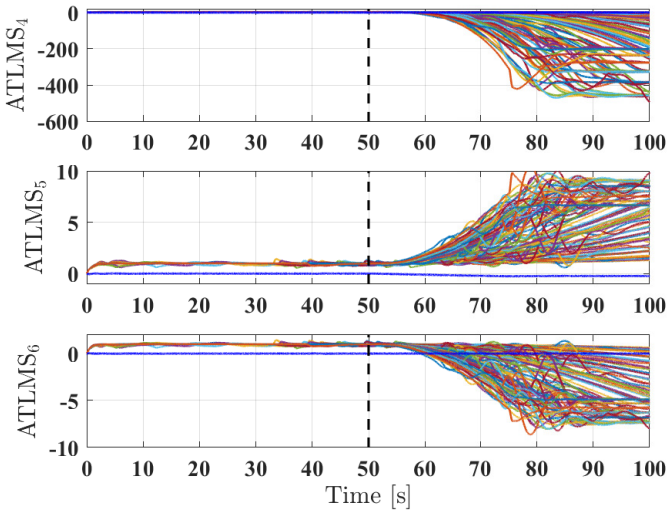

Figure G.5: Adaptive threshold responses for the EKF-ATLMS approach regarding incipient faults in aircraft acceleration a_y during simulation campaign as defined in table G.1. After fault occurrence, $\text{ATLMS}_4 < r_\psi$, $\text{ATLMS}_5 > r_\beta$, and $\text{ATLMS}_6 < r_\alpha$. ATLMS_1, ATLMS_2, and ATLMS_3 can assume either positive or negative values. This behavior produces the adaptive threshold sign pattern $(*, *, *, -, +, -)$ which can provide useful information for fault diagnosis.

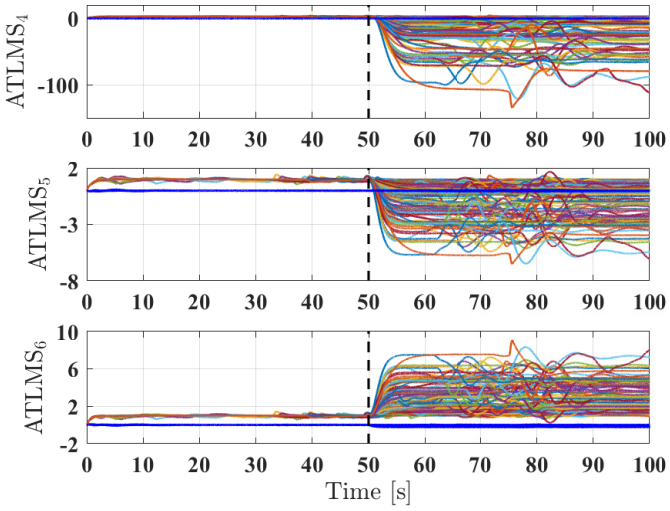

Figure G.6: Adaptive threshold responses for the EKF-ATLMS approach regarding abrupt faults in aircraft acceleration a_z during simulation campaign as defined in table G.1. After fault occurrence, $\text{ATLMS}_4 < r_\psi$, $\text{ATLMS}_5 < r_\beta$, and $\text{ATLMS}_6 > r_\alpha$. ATLMS_1, ATLMS_2, and ATLMS_3 can assume either positive or negative values. This behavior produces the adaptive threshold sign pattern $(*, *, *, -, -, +)$ which can provide useful information for fault diagnosis.

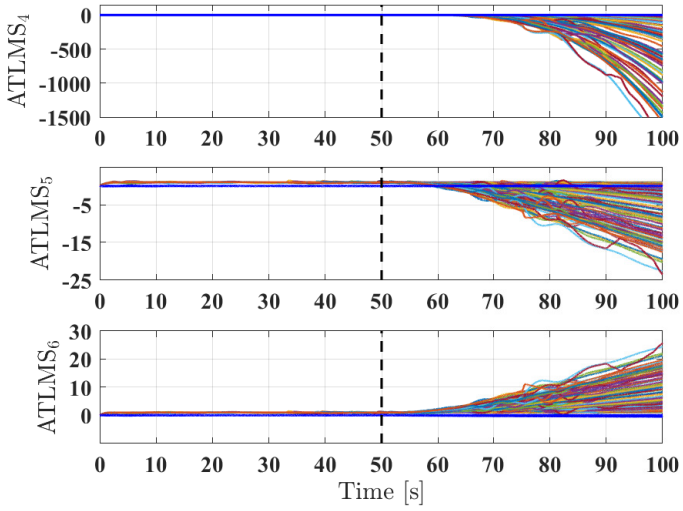

Figure G.7: Adaptive threshold responses for the EKF-ATLMS approach regarding incipient faults in aircraft acceleration a_z during simulation campaign as defined in table G.1. After fault occurrence, $\text{ATLMS}_4 < r_\psi$, $\text{ATLMS}_5 < r_\beta$, and $\text{ATLMS}_6 > r_\alpha$. ATLMS_1, ATLMS_2, and ATLMS_3 can assume either positive or negative values. This behavior produces the adaptive threshold sign pattern $(*, *, *, -, -, +)$ which can provide useful information for fault diagnosis.